This is to certify that the

dissertation entitled

Design and Characterization of a Fiber Optic Based
Intensified Diode Array Fluorometer
for Measuring Absorption-Corrected, Synchronous Fluorescence

presented by

Mark Alan Victor

has been accepted towards fulfillment
of the requirements for

Doctor of Philosophy degree in Chemistry

Stanley R. Crouch
Major professor

Christie G. Enke

Date 2/14/94

Design and Characterization of a Fiber Optic Based Intensified Diode Array Fluorometer for Measuring Absorption-Corrected, Synchronous Fluorescence

By

Mark Alan Victor

A DISSERTATION

Submitted to
Michigan State University
in partial fulfillment of the requirements
for the degree of

DOCTOR OF PHILOSOPHY

Department of Chemistry

1993

ABSTRACT

DESIGN AND CHARACTERIZATION
OF A FIBER OPTIC BASED INSTRUMENT FOR MEASURING
ABSORBANCE CORRECTED SYNCHRONOUS FLUORESCENCE

By

Mark Alan Victor

Inner-filter effects in synchronous fluorescence spectroscopy can lead to large and unexpected quantitative errors. To alleviate this problem, instrumentation and methodologies were developed and characterized to correct for primary and secondary absorption effects in complicated matrices encountered in synchronous fluorescence spectroscopy. The bifurcated fiber optic-base fluorometer simultaneously measures front surface fluorescence and total solution absorbance. This allows calculation of the transfer function that describes the coupling efficiency between the excitation and emission arms of the fiber optic. Once characterized, such a fluorometer is capable of calculating a fluorescence signal corrected for absorption effects. The experimentally determined, wavelength dependent transfer function, along with the measured absorptivity at the excitation and emission wavelengths, permits generation of an array of correction factors for all excitation/emission combinations. Applications to synchronous fluorescence measurements in previously problematic situations are demonstrated and discussed.

To my Parents,

friends and relatives,

brothers and sisters

ACKNOWLEDGMENTS

"If I have seen further (than you and Descartes) it is by standing upon the shoulders of Giants" . [1]

I, as with all preceding graduate students who ponder the final weight and magnitude of their thesis, reflect on the accomplishment it represents, congratulate myself, while the first thought coming to mind is, "look at all I have done". However the "I" must quickly give way to "we". The support I received, both technical and personal, in the form of guidance, support, solace and advice, from my professors (Chris and Stan), is immeasurable and provided the cornerstones on which this work was developed. Although this thesis represents the majority of my graduate work, my most lasting impressions of graduate school are the personal memories of friends, students, professors, beach parties, fireworks, hiking, spelunking, lunch conversations, good jokes, including the usual (and unusual) pranks.

I cannot forget the many people who shared the graduate experience with me, and through their friendship and support made my work creative, and my frustrations bearable. The advantages of having two research groups upon which to draw support becomes a handicap when trying to acknowledge your friends. Special thanks to Norman and Susan Penix, Gene Ratzlaff., Charlie Patton, Pete Wentzell, Bob Harfmann, Dean Peterson, Pete Palmer, and others too numerous to list but impossible to forget.

---

1 . Sir Isaac Newton, Letter to Robert Hooke, February 5, 1675/1676.

TABLE OF CONTENTS

LIST OF TABLES

LIST OF FIGURES

CHAPTER I

CHAPTER II

CHAPTER V

CHAPTER 1

ABSORPTION-CORRECTED SYNCHRONOUS FLUORESCENCE SPECTROMETRY

Review of Synchronous Fluorescence Spectrometry

"I have placed my rainbow in the clouds as a sign of my promise until the end of time, to you and all the earth." [1]

Since its introduction to Noah [1], the wavelength dispersion of light as an analytical tool has grown steadily in popularity and diversity in the past 5,500 years. Fairly recent advances in technology have expanded and refined wavelength dispersive methodologies to include synchronous fluorescence spectrometry. In synchronous fluorescence spectrometry, as opposed to conventional fluorescence spectrometry, the excitation and emission wavelengths are varied simultaneously. With an increased need for rapid and sensitive methods of analysis of complex environmental and clinical samples, conventional fluorescence has a somewhat limited applicability. This is because most spectra of complex mixtures cannot be resolved satisfactorily without prior separation. This inability to do multicomponent analysis without resorting to time consuming or expensive sample preparation limits the applicability of conventional fluorescence techniques. Since first being introduced by Lloyd [2] for the qualitative and quantitative analysis of petroleum residues, synchronous fluorescence spectrometry has been accepted as a standard analytical method.

Basic Performance of Synchronous Fluorescence

The basic performance of the synchronous technique is illustrated in Figure 1-1. The conventional excitation and emission spectra of dansyl chloride in 95% ethanol are shown in Figure 1-1a. The fluorescence spectrum (with λ_{ex} = 323 nm), shows a single featureless band, covering the spectral range from 400 to 600 nm. The excitation spectrum ranges from 250 to 400 nm. Figure 1-1a reveals an absorption maximum off scale at 250 nm and an absorption band at 323 nm. The small wavelength difference of 3 nm between the peaks of the 0-0 band in the emission and excitation spectra is called the "Stokes shift." The synchronous fluorescence spectrum of dansyl chloride, Figure 1-1b, is produced when the wavelength interval ($\Delta\lambda$ = 3 nm) is set to match the Stokes shift. Instead of a spectrum that spans several hundreds of nanometers, the synchronous signal consist of a single peak at 389 nm. This peak is the product of two nearly mirror-symmetrical functions, the excitation and emission spectra.

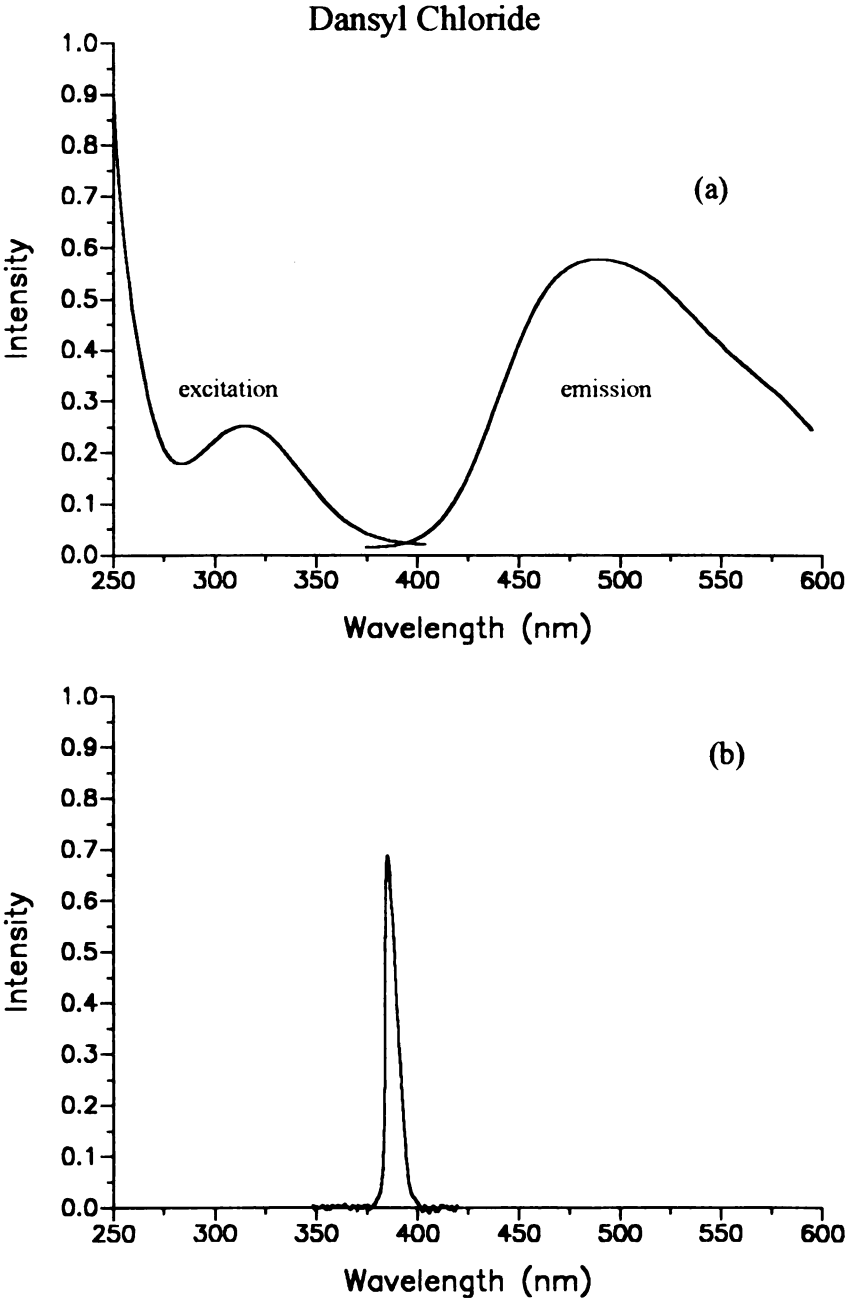

Figure 1-1

Synchronous Fluorescence Spectra of Dansyl Chloride

Show in Figure 1-1a is the excitation emission spectra of dansyl chloride. The synchronous fluorescence spectrum is shown in 1-1b. The synchronous fluorescence spectrum was measured on a Perkin Elmer Lambda III spectrofluorometer with $\Delta\lambda$ = 3 nm. The gain was increased some 20 fold to compensate for the reduced intensity of the synchronous signal. Ten passes of a modified Savitsky-Golay filter was used to smooth both spectra.

Line Narrowing

Another advantage of synchronous fluorescence is an inherent line narrowing effect. In conventional fluorescence spectroscopy, the spectrum is observed as a resolved structure only when the observed fluorescence function consist of narrow bands. However, with the synchronous technique, a resolved spectrum can be obtained if either the excitation or the emission spectrum consist of narrow peaks. This increases the likelihood of obtaining spectra with resolved structure. This band narrowing effect is a consequence of multiplying two functions that increase and decrease simultaneously (Figure 1-2).

Spectral Simplification

In many instances the synchronous technique can greatly simplify complex spectra consisting of single or multiple components. This is best illustrated visually. As shown in Figure 1-3a, a single peak signal is observed only when the wavelength interval $\Delta\lambda$ matches one unique pair of absorption and emission bands. Spectral simplification for two components of a mixture is shown graphically in Figure 1-3b. Here, a single component of a mixture can be resolved by selecting an appropriate $\Delta\lambda$ which is unique to a particular fluorophore.

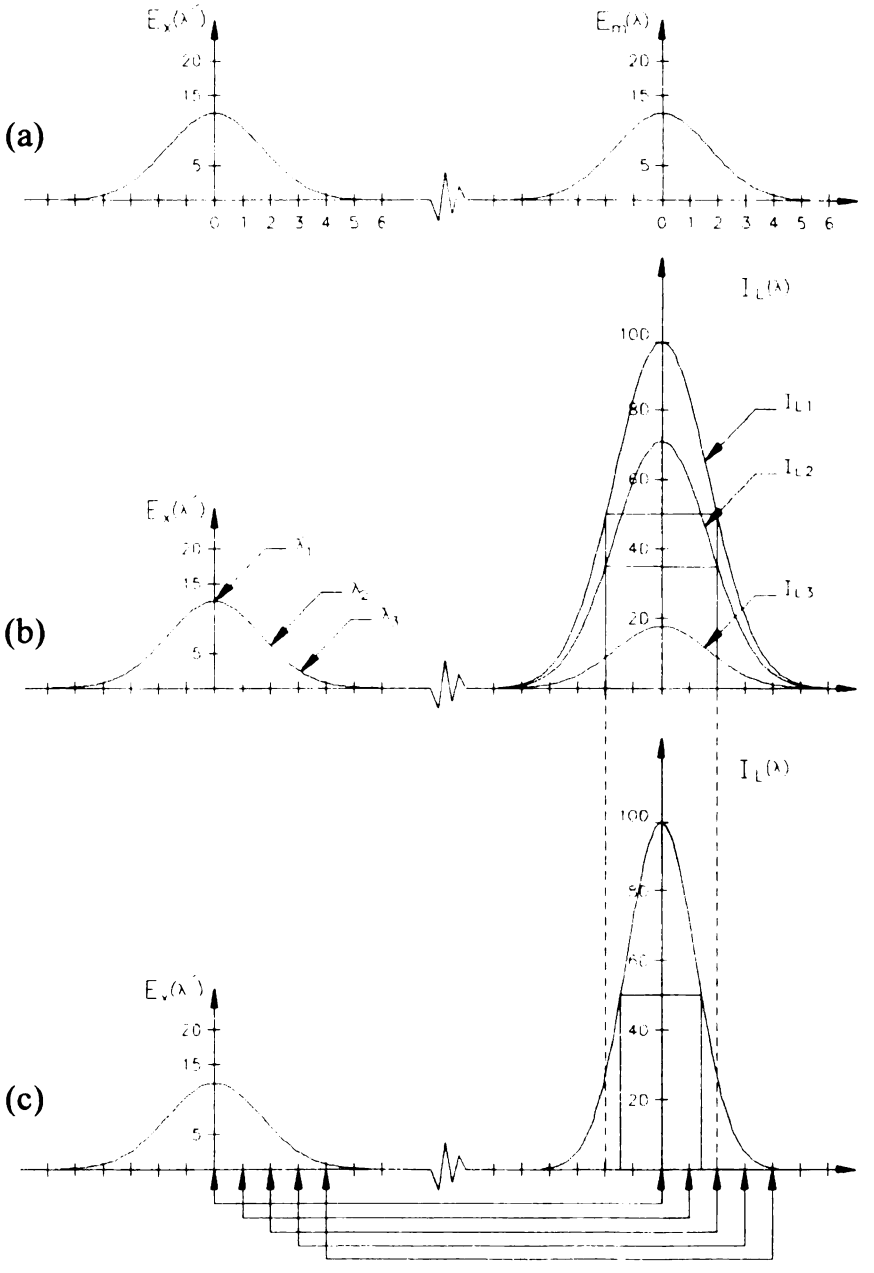

Figure 1-2

Band Narrowing Effect of Synchronous Fluorescence

Figure 1-2a shows the relationship between excitation (E_x) and emission (E_m) band in a conventional fluorescence measurement. The emission bandwidth is relatively independent of the experimental conditions. In synchronous fluorescence (Figure 1-2b), the emission intensity (I_I) increases proportionally with the efficiency of sample excitation (λ'), while the emission bandwidth remains constant. The band narrowing effect of synchronous fluorescence is illustrated in Figure 1-2c. The resultant synchronous fluorescence signal is the multiplicative product of the two functions $E_x(\lambda')$ and $E_m(\lambda)$ which increase and decrease synchronously. The emission band width thus remains constant, while its height increases, increasing its height to width ratio.

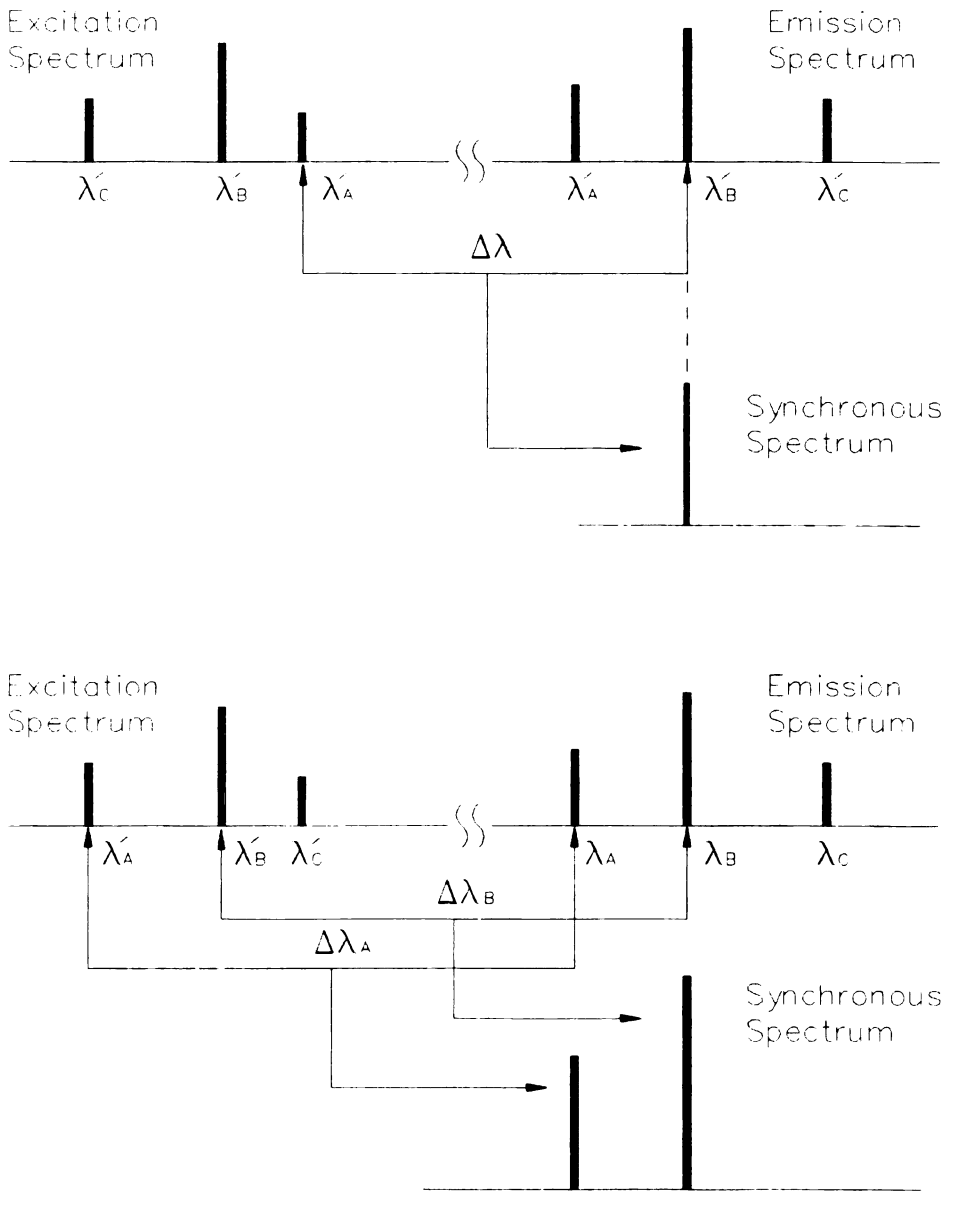

Figure 1-3

Spectral Simplification Effect of Synchronous Fluorescence

Figure 1-3a represents spectrum simplification by a judicious choice of Δλ. A hypothetical fluorophore which contains multi-banded excitation and emission spectra generates a single signal when synchronously scanned at Δλ. Similarly 1-3b illustrates how multiple components can be resolved by choosing ΔλA or ΔλB. Multiple components can be resolved by the position of their Stokes shift at a constant Δλ.

Applications of Synchronous Fluorescence

Fingerprinting Polynuclear Aromatic Hydrocarbons (PAH's) in Mixtures

Synchronous fluorescence has proven useful in the qualitative and quantitative spectral characterization of complex mixtures of polyaromatic hydrocarbons (PAH's) without prior physical separation [3 -17], or where separation methods are incomplete [18 -20]. The technique is successful in fingerprint identification of PAH samples in micellular medium [21 , 22]. Environmental uses include quantitative and qualitative identification of PAH's in muds and sediments [23 -27], fly ash and air [28 -40], fresh and seawater [41 -46], industrial effluents [47 -50], and biological fluids [51 -55].

Metal Cation Determination via Constant Energy Synchronous Fluorescence

Synchronous fluorescence facilitates the simultaneous analysis of multiple metal cations via their fluorescent complexes [57, 56 -72]. Selectivity can been further enhanced by computing high-order derivatives of synchronous spectrum [65, 66, 74-80]. Constant energy synchronous fluorescence (CESL) has shown advantages over constant wavelength measurements in quantitative and fingerprinting applications [81 -90]. Scanning at a fixed $\Delta\nu$ instead of $\Delta\lambda$ is preferred because the electronic transitions that give rise to absorbance and emission bands are quantized at discrete energy levels. Constant energy synchronous fluorometry has been described as a means of reducing solvent Raman scatter interference on the fluorescence spectrum of trace concentrations of organic molecules [91].

Limitations of Synchronous Fluorescence

With increasing complexity of the sample matrix, the advantages of synchronous fluorescence are quickly overcome by those effects which limit classical fluorescence measurements, most commonly quenching and inner filter effects. The assumption that the observed fluorescence is proportional to fluorophore concentration is valid for a single fluorophore at low concentration. However, when the fluorophore absorbs a significant proportion of the incident radiation, the result is uneven sample illumination throughout the sample cell. This is what limits the upper end of the linear dynamic range of a fluorescence calibration curve. In the complicated matrices encountered in synchronous fluorescence measurements, absorbance may be high at the excitation wavelength (primary absorbance), or at the emission wavelength (secondary absorbance), due to various components in the sample matrix.

Without methodology to correct for non-quenching effects, the source of signal reductions from their expected values can be ambiguous [92]. Other investigators [109] have noted that the wide differences in the linearity ranges of various synchronous fluorescence bands in a mixture is dependent largely on the bands energy. Linearity ranges for the high energy synchronous fluorescence bands of fluorene (304 nm), acetanapthene (323 nm), and 2,3-benzofluorene (342 nm) extended over less than 3 orders of magnitude, whereas the linearity ranges of the lower energy synchronous bands of anthracene (378 nm), benzo-[a]-pyrene (405 nm), and perylene (438 nm), extended over 3-4 orders of magnitude. An empirical description of the magnitude of inner filter effects vs wavelength (Figure 1-4) describes how secondary inner filter effects are more severe at shorter wavelengths.

Inner filter effects can be compensated by sample dilution or the standard addition method [93]; however, signal enhancement may be at the expense of weak fluorophores whose

concentration is lowered below the instrument's detection limits. In the case of strong absorbance by the analyte itself, the standard addition method will not produce a linear calibration curve. A technique that can deal with absorbances as high as 3.0 is as analytically useful as a 1000 fold dilution. Real time correction methodology is preferable for monitoring dynamic systems or flowing streams where removing aliquots for dilution is not always feasible.

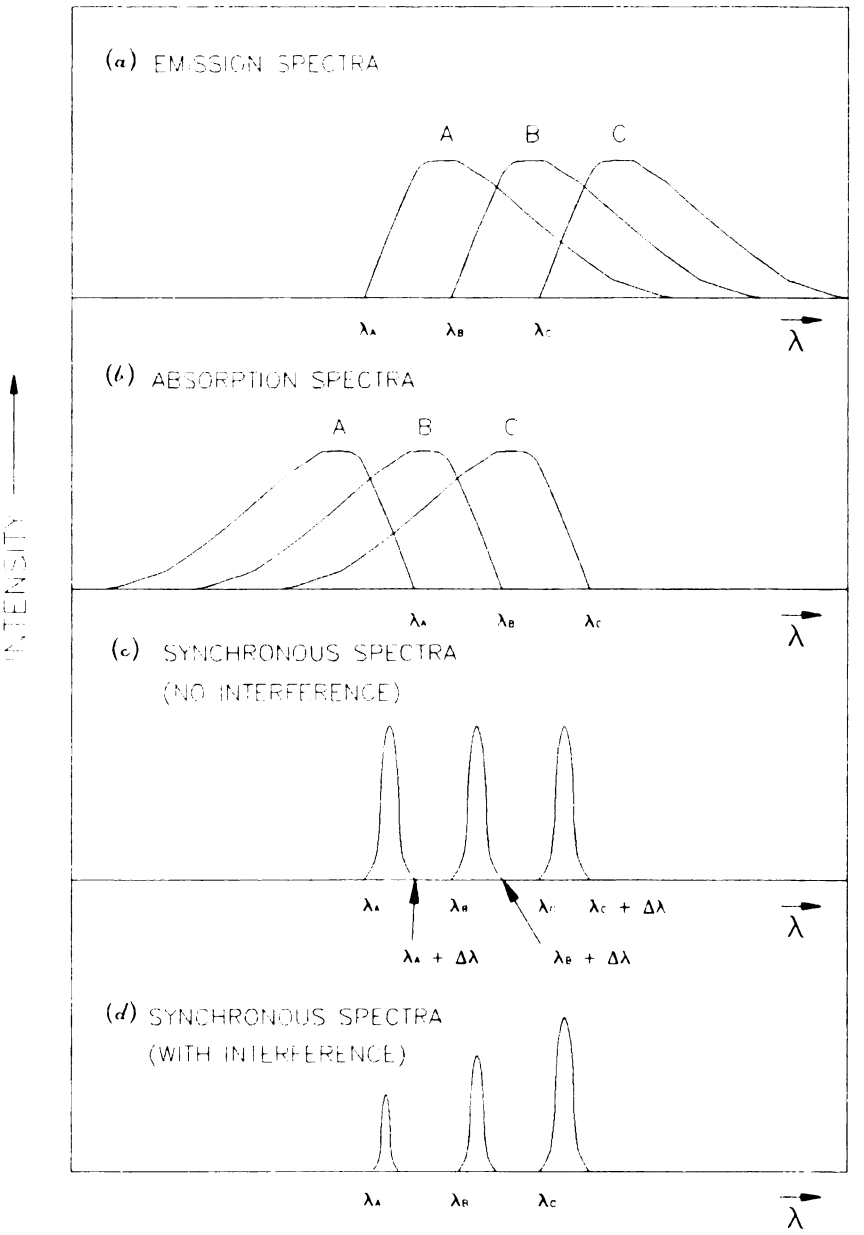

Figure 1-4

Matrix Effects in Synchronous Fluorescence

Figure 1-4 graphically shows post filter matrix effects encountered in synchronous fluorescence. Analytes emitting at shorter wavelengths lie under one or more absorbance bands of other analytes present in the mixture. Matrix effects are most severe at shorter wavelengths and less troublesome for fluorophores emitting at longer wavelengths.

HISTORY OF INNER FILTER EFFECTS INVESTIGATIONS

Previous investigators have described mathematical corrections to explain and/or instrumentation to compensate for absorption effects in fluorometry [94 -107]. However, most of this work deals with conventional instrumentation based on standard one centimeter square cuvettes which are not readily adapted for use with flowing streams or small sample volumes. Most of the instrumental techniques require spatial displacement of either the cell or the optical path in time. This precludes any correction based on such a method from being used for rapid kinetic or transient effects.

Because synchronous fluorescence spectroscopy is used primarily to resolve distinct spectral features of single fluorophores within mixtures, classical synchronous fluorescence techniques are uniquely susceptible to inner filter effects. As most commercially available fluorometers are unable to diagnose or differentiate whether signal attenuation is due to inner filter effects or quenching, synchronous fluorescence methodology should routinely make provisions for dealing with suspect samples. Other investigators have observed dramatic signal reductions for individual components of mixtures of PAH's [92, 108]. Although ambiguities between quenching and inner filter effects have been discussed in the literature [92, 108, 109], dilution studies offered evidence that signal attenuation was attributable to inner filter effects [108]. It has also been empirically explained how fluorophores whose synchronous fluorescence signal were observed at shorter wavelengths were more likely to be suppressed [6].

The fingerprinting capability of synchronous fluorescence would be markedly enhanced if matrix-dependent inner filter anomalies could be corrected by a mathematical model which accurately predicts the synchronous fluorometer's behavior. Such a model has been developed by Ratzlaff, Harfmann and Crouch [110]. It provides a method of correction based on the aggregate absorbances at the excitation and emission wavelength. The

mathematical model described by Ratzlaff, et al., has shown the ability to describe the coupling efficiency between the excitation and emission arms of a front-surface, bifurcated fiber-optic based, fluorometer. Ratzlaff et al., call the term describing the coupling efficiency as a function of distance the transfer function. When adequately characterized, this transfer function completes a mathematical description of a front surface fluorometer which is capable of deconvolving the effect of primary and secondary inner filter effects to produce absorption corrected spectra in real time. The type of instrument described by Ratzlaff et al. is preferable to earlier instruments for absorbance-corrected synchronous fluorescence because no spatial displacement of the cell is required, the correction is performed in real time, and the measurement can be made on flowing streams.

Because no requirements are made on beam collimation, the technique produces higher signal-to-noise ratios than conventional cell shift methods which require collimated beams [102]. The lack of moving parts and the employment of fiber optics also make the method more desirable in vibration-prone or otherwise inhospitable environments. Additionally, the technique requires very little modification over the basic fiber optic fluorometer described by Aldous [111].

Lack of complete characterization of the fluorometer developed by Ratzlaff [110], had placed doubts on the stability of the transfer function across the broad wavelength range encountered in synchronous fluorescence spectroscopy [110]. As currently described, the transfer function is solely dependent on the fibers effective numerical aperture (*na*). As the fibers *na* is also wavelength dependent, the simultaneous scanning of the excitation and emission monochromators in synchronous fluorescence is expected to require a different correction factor for every possible excitation/emission wavelength combination. Because the fluorometers' transfer function had only been determined at a single wavelength pair [110], a means of rapidly determining the transfer function at all excitation/emission wavelengths was desired. This chapter deals with a such a method for complete

characterization of the transfer function as a function of excitation/emission wavelength. The instrument, once accurately calibrated at all excitation/emission wavelengths, can then be used for absorbance corrected synchronous fluorescence measurements.

A FLUORESCENCE INTENSITY EXPRESSION

A Mathematical Model for a Bifurcated Fiber Optic Fluorometer

The mathematical model for a fiber optic based fluorometer is based on the work of Ratzlaff et al. [110], which has roots in a general mathematical model for the collimated, front-surface fluorometer developed by van Slagern, den Boef, and van der Linden [112]. The complete derivation is presented here for the sake of better understanding the differences between the procedures used to characterize the instrumental parameters.

The theoretical basis of the signal vs. concentration or the signal vs. absorbance functions has been described earlier by Ratzlaff for a front surface fluorometer as shown in Figure 1-5. The model makes the following assumptions.

1.) A cylinder of known dimensions defines the volume of the cell.

2.) The front surface emission is collected from the front of the cell comprised of the end of a bifurcated fiber optic whose fibers are randomized.

3.) Transmittance is measured from a transparent window on the far end of the cell.

4.) The cell window and walls are non reflective.

5.) The excitation and emission beams are assumed to be monochromatic and homogeneous.

6.) Scattered light, refractive index effects and reflections within the cell are negligible.

7.) Reemission of absorbed fluorescence is negligible.

The radiant power P_X, at any point in the cell a distance x from the excitation window is given by Beer's law as,

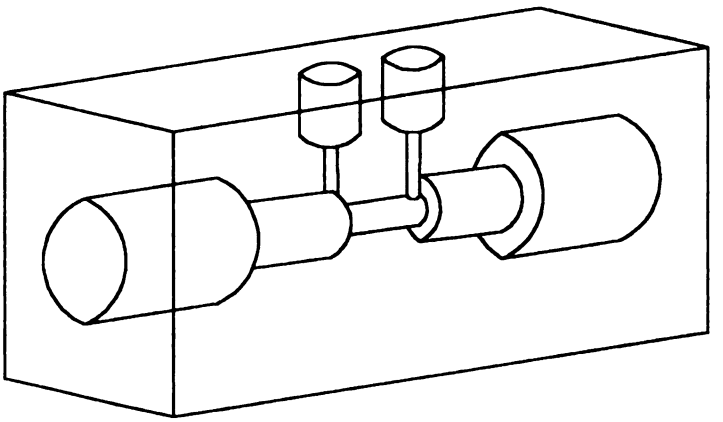

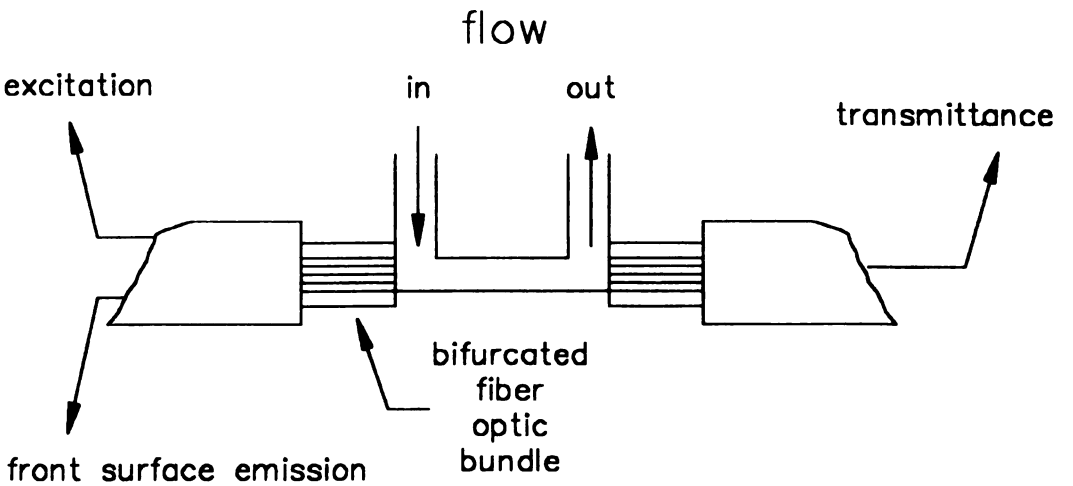

Figure 1-5

Flow Cell for Front Surface Fluorescence Measurements

Flow cell designed for simultaneous emission/transmittance measurements to permit absorbance corrected fluorescence measurements. Front surface fiber optic excitation/emission facilitates measurements on flowing streams and small volumes.

$$P_x = P_0\left[\log(\varepsilon c)_{ex} x\right] = P_0\left[\exp\left(-2.303\left\{(\varepsilon c)_{ex} x\right\}\right)\right] \qquad (1)$$

where $(\varepsilon c)_{ex}$ is the summation of absorptivities per unit pathlength at the excitation wavelength and P_O is the initial power of the excitation beam at front surface of the cell. The fluorescent power generated at a differential slice dF_{dx} is given by,

$$dF_{dx} = QP_x(\varepsilon c)_f dx = Q P_0\left[\exp\left(-2.303\left\{(\varepsilon c)_{ex} x\right\}\right)\right](\varepsilon c)_f dx \qquad (2)$$

where Q is the quantum efficiency of the fluorophore and $(\varepsilon c)_f$ represents the cumulative absorptivity of the fluorophore at the excitation wavelength over the pathlength of the cell. The excitation actually returned and observed from this infinitely thin plane dF_x (Figure 1-6) is a function of the absorptivity over the pathlength of the cell at the emission wavelength, given by

$$dF_x = T(x)\, dF_{dx}\left[\exp\left(-2.303\left\{(\varepsilon c)_{ex} x\right\}\right]\right.$$

$$dF_x = G\, T(x)\left[\exp\left(-2.303\left\{(\varepsilon c)_{ex} + (\varepsilon c)_{em} x\right\}\right]\right. \varepsilon c_f dx \qquad (3)$$

where $(\varepsilon c)_{ex}$ represents the aggregate absorptivity over the pathlength of the cell at the excitation wavelength, and $(\varepsilon c)_{em}$ is the summation of absorptivities over the pathlength of the cell at the emission wavelength. Parameter G incorporates the quantum efficiency, wavelength dependence, and the efficiency of the sources, optics and detectors. T(x) is the transfer function which describes excitation efficiency and emission collection as a function of distance into the cell. The total fluorescence observed is found by integrating equation 3 over the cell pathlength, b

$$F_b = P_o\,(\varepsilon c_f)\, G\, T(x) \int_0^b \left[\exp\left(-2.303\left\{(\varepsilon c)_{ex} + (\varepsilon c)_{em} x\right\}\right]\right. dx \qquad (4)$$

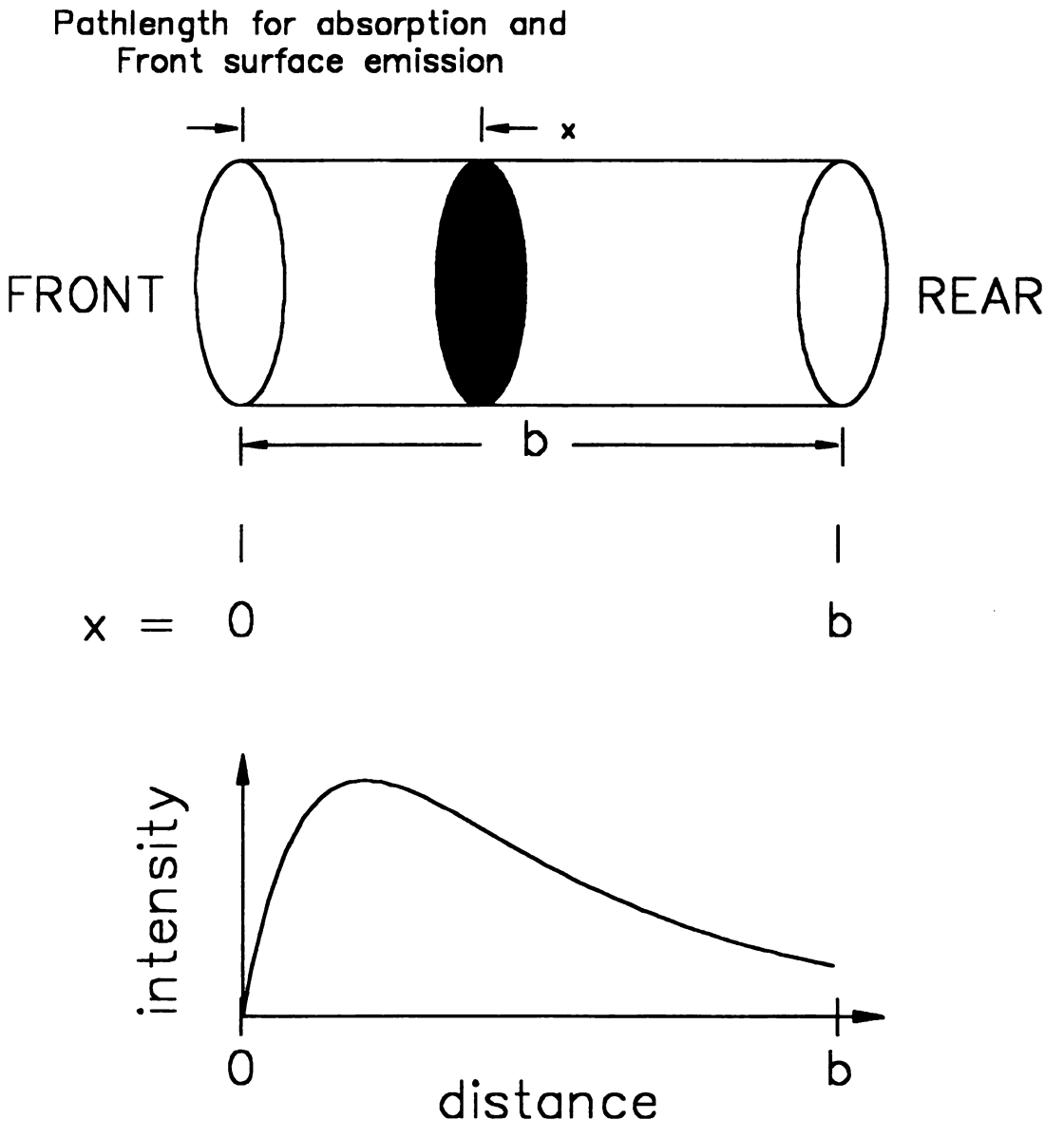

Figure 1-6

Dual Exponential Behavior of the Transfer Function

With increasing distance into the cell improved coupling between the excitation and emission fibers causes an exponential rise near the front surface. With increasing distance into the cell, intensity drop is inversely proportional to the distance into the cell. This transfer function $T_{(b)}$ can be modeled as a dual exponential of form $T_{(b)} = G(e^{-Hx} - e^{-Kx})$, where H and K describe the exponential rise and decay respectively.

An Empirical Description of the Fiber Optic's Transfer Function

For a simple right angle geometry or collimated excitation and emission beams, T(x) remains constant at a given wavelength. The exit and acceptance angle for an individual fiber is governed by its numerical aperture (*na*). This in turn is governed by the composition of the fiber and the refractive index of the media in which the fiber is immersed.

$$na = \eta_0 \sin\theta_0 = \sqrt{\left(\eta_1^1 - \eta_2^2\right)} \qquad (5)$$

The numerical aperture (*na*), is defined in equation 5 [113], where η_1 and η_2 are the refractive indices of the core and cladding (Figure 1-7a). The light emanating from a fiber thus resembles the inverted frustum of a cone with the exit angle from perpendicular being given by $\theta = \sin(na)$. Likewise rays intended for collection cannot enter at angles steeper than $\theta = \sin(na)$ in order to successfully traverse the fiber. This gives the appearance of clearly defined cones of admittance and acceptance for emission and excitation respectively (Figure 1-7b). At zero distance into the cell, the radiant power of the excitation beam is greatest. However, the finite thickness of the fibers cladding places the fluorescing portion of the solution out of view of the excitation fibers. No emission is expected to be observed from the front surface of the cell. Further into the cell the more effective overlap of the excitation and emission beams increases the efficiency of which fluorescence is generated and observed (Figure 1-8). The exponential rise in beam overlap is tempered by the exponential decrease in intensity of the diverging excitation beam.

An empirical mathematical description of the previously described effects predicts an exponential rise attributable to increased coupling efficiency, offset by the exponential decay with distance into the cell of the excitation beam intensity [110, 114]. A suitable

mathematical description of the above process which is can be directly integrated within equation 4 is,

$$T(x) = G\left(e^{-Hx} - e^{-Kx}\right) \tag{6}$$

where G is a normalization constant taking into effect source and detector wavelength dependence and fluorescent quantum efficiency, H describes the exponential rise, and K describes the exponential decay. Although this model is still intuitive, experimental evidence by Smith, Jackson, and Aldous [114] support this description of the transfer function. The evidence was obtained by measuring the scattered intensity from a specular reflector at varying distances through the cell. The researchers noted an exponential rise close near the front surface with an exponential drop noted further into the cell. The maximum scattering intensity was observed at a depth of 3 mm.

Substituting Equation 6 into Equation 4 and integrating yields,

$$F_b = P_0(\varepsilon c)_f G\left[\frac{1}{M}\left(1 - e^{-Mb}\right) - \frac{1}{N}\left(1 - e^{-Nb}\right)\right] \tag{7}$$

which describes the observed fluorescence in terms of the analyte absorbances at the excitation and emission wavelengths where:

$$\left.\begin{aligned} M &= H + 2.303\left((\varepsilon c)_{ex} + (\varepsilon c)_{em}\right) \\ N &= K + 2.303\left((\varepsilon c)_{ex} + (\varepsilon c)_{em}\right) \end{aligned}\right\} \tag{8}$$

The limiting form for Equation 7 for low absorbances occurs when $\left((\varepsilon c)_{ex} = (\varepsilon c)_{em} = 0\right)$ and equation 7 becomes:

$$F_0 = P_0(\varepsilon c)_f G\left[\frac{1}{H}\left(1 - e^{-Hb}\right) - \frac{1}{K}\left(1 - e^{-Kb}\right)\right] \tag{9}$$

where F_O is the unattenuated fluorescence observed. We can solve for a correction factor (CF), which when multiplied by the observed fluorescence, will produce the fluorescence signal (F_O) corrected for primary and secondary absorbance. This can be done by substituting Equation 8 into Equation 9 and rearranging. The correction factor can be expressed as shown in equation 10.

$$CF = \frac{\frac{1}{H}\left(1-e^{-Hb}\right)-\frac{1}{K}\left(1-e^{-Kb}\right)}{\frac{1}{M}\left(1-e^{-Mb}\right)-\frac{1}{N}\left(1-e^{-Nb}\right)} \qquad (10)$$

Therefore, measurement of the absorptivities at the excitation and emission wavelengths should allow for compensation for both primary and secondary inner filter effects in front surface fluorometry. Determination of values for M and N, and thus H and K, can be done by nonlinear regression of fluorescence vs. absorbance $(\varepsilon c)_{ex}$ data on Equation 7 for a known fluorophore where $(\varepsilon c)_{em} = 0$. Values for H and K can also be obtained by regression on Equation 6 from the fluorescence observed from simulated infinitely thin slices at varying depths into the solution.

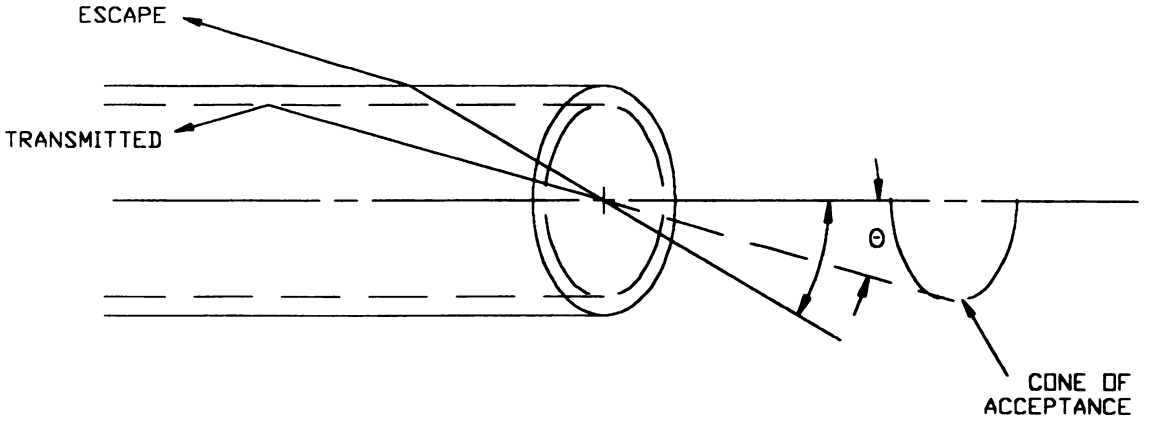

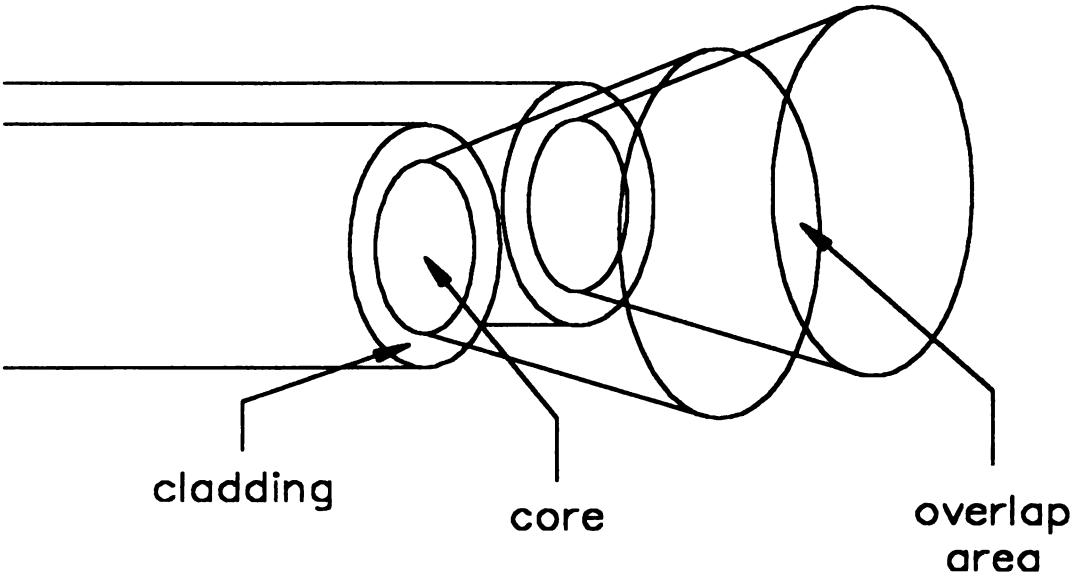

Figure 1-7

Numerical Aperture Limited Cones of Excitation and Emission

Figure 1-7a shows how the acceptance angle, or the numerical aperture, defines the limits of the cone of acceptance for a single fiber. Figure 1-7b shows that as the sampling depth into the cell increases, so does the overlap efficiency of the excitation and emission fibers. Sample excitation decreases exponentially, receding into the cell due to the divergence of the rays from the excitation fibers.

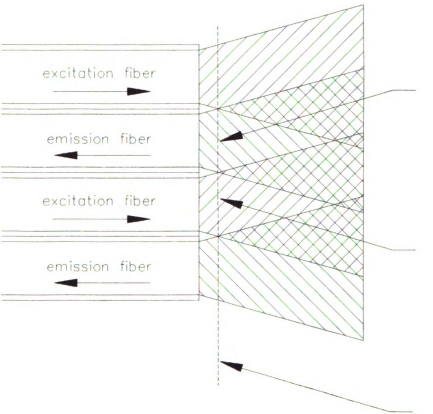

Figure 1-8

Excitation Emission Fiber Overlap

Near the front surface of the excitation fibers the emission capture is negligible. Likewise directly in front of the emission fibers, illumination is zero. This accounts for the lack of any observable fluorescence until appreciable excitation/emission overlap occurs. Fluorescence occurs but is not observed until the excitation and emission cones overlap at the minimum penetration depth.

EXPERIMENTS IN ABSORPTION-CORRECTED SYNCHRONOUS FLUORESCENCE

Soluble Fluorophores for Synchronous Fluorescence Studies

Dimethylaminonapthalenesulphonylchloride (Dansyl Chloride) 98%, perylene 99+%, 1,1,4,4-tetraphenylbutadiene 99%, (Aldrich Chemicals of Milwaukee Wisconsin) and pyrene 99+%, fluorene 98%, phenanthrene 98% (Sigma Chemical Supply), anthracene 99.9+% (Eastman Kodak Co., Rochester, NY.), and spectrophotometric grade cyclohexane (Mallincrodt, Paris, KY.) were used without further purification. Stock solutions of 500 μg/mL in cyclohexane were prepared for phenanthrene, fluorene, pyrene, perylene, 1,1,4,4-tetraphenylbutadiene, and dansyl chloride, while stock solutions of 100 μg/mL were prepared of anthracene and perylene. All solutions were stored in the dark to prevent photodecomposition and extend shelf life. Table 1-1 shows the working

Table 1-1

Reagents for Instrument Characterization	
Reagent	Concentrations
Dansyl Chloride (in ethanol) (λ_{ex} = 322, λ_{em} = 459, 552, 600 nm)	0.0, 5.0, 10.0, 20.0, 30.0 40.0, 50.0, 70.0, 80.0, 100.0 (2.45 AU @ 70.0 μg/mL)
1,1,4,4-Tetraphenylbutadiene (in cyclohexane) (λ_{ex} = 348, λ_{em} = 450 nm)	0.0, 3.0, 6.0, 9.0, 12.0, 15.0 18.0, 21.0, 24.0, 27.0, 30.0 (2.88 AU @ 30.0 μg/mL)
Quinine Sulfate (in 0.09 M $HClO_4$ (λex = 318, λ_{em}= 460 nm)	0.0, 4.0, 12.0, 16.0, 20.0 24.0, 28.0, 32.0, 36.0, 40.0 (2.79 AU @ 40.0 μg/mL)
Perylene (in cyclohexane) (λ_{ex} = 322, λ_{em} = 434, 458, 504 nm)	0.0, 0.9, 1.8, 2.7, 3.6 4.5, 5.4, 6.3, 7.2, 8.1, 9.0 (2.67 AU @ 8.1 μg/mL)

reagents prepared, along with the maximum absorbance measured for which Beers' law adherence was observed. A solution of 0.065 g/L $K_2Cr_2O_7$ in 0.01 N H_2SO_4 was prepared as a known absorbance standard for determination of the cell pathlength. A mixture of five PAH's, similar to that of Latz and Winefordner [92], was prepared for the stock reagents. Four of the PAH's were present at constant concentrations, fluorene (24.0 μg/ml), phenanthrene (40 μg/ml), anthracene (1.0 μg/ml), and perylene (0.06 μg/ml). The concentration of pyrene was varied, as shown in Table 1-2.

Table 1-2

Reagents for Inner-Filter Effects Study	
Mixture number	Pyrene concentration (μg/mL)
1	0.0
2	0.02
3	1.0
4	2.0
5	10.0
6	20.0
7	40.0

Immobilized Phosphor for Characterization of the Instrument

To simulate the measurement of the fluorescence from successive infinitely thin layers, a thin surface phosphor was fabricated by grinding together blue, yellow, orange, and red fluorescent chalks (Weber Costello Inc., Troy, MO). The pigments were mixed in experimentally determined proportions to give a phosphor with the broadband output shown in Figure 1-9. The phosphor mixture was then finely ground with decolorizing charcoal and mixed with an epoxy resin. A brass rod of the same i.d. as the flow cell was dipped in the resultant mixture and allowed to set. The hardened resin/phosphor mixture was machined and sanded to give a flat plug of broad band phosphor on the end of the brass rod. The presence of large amounts of charcoal in the mixture was necessary to assure sampling was to be only from the front surface of the phosphor mixture, prevent depth profiling, light piping, and scattering by rendering the transparent epoxy resin matrix opaque. The front surface, broad band phosphor, was advanced with a micrometer drive through the length of the cell (see later Figure 1-11).

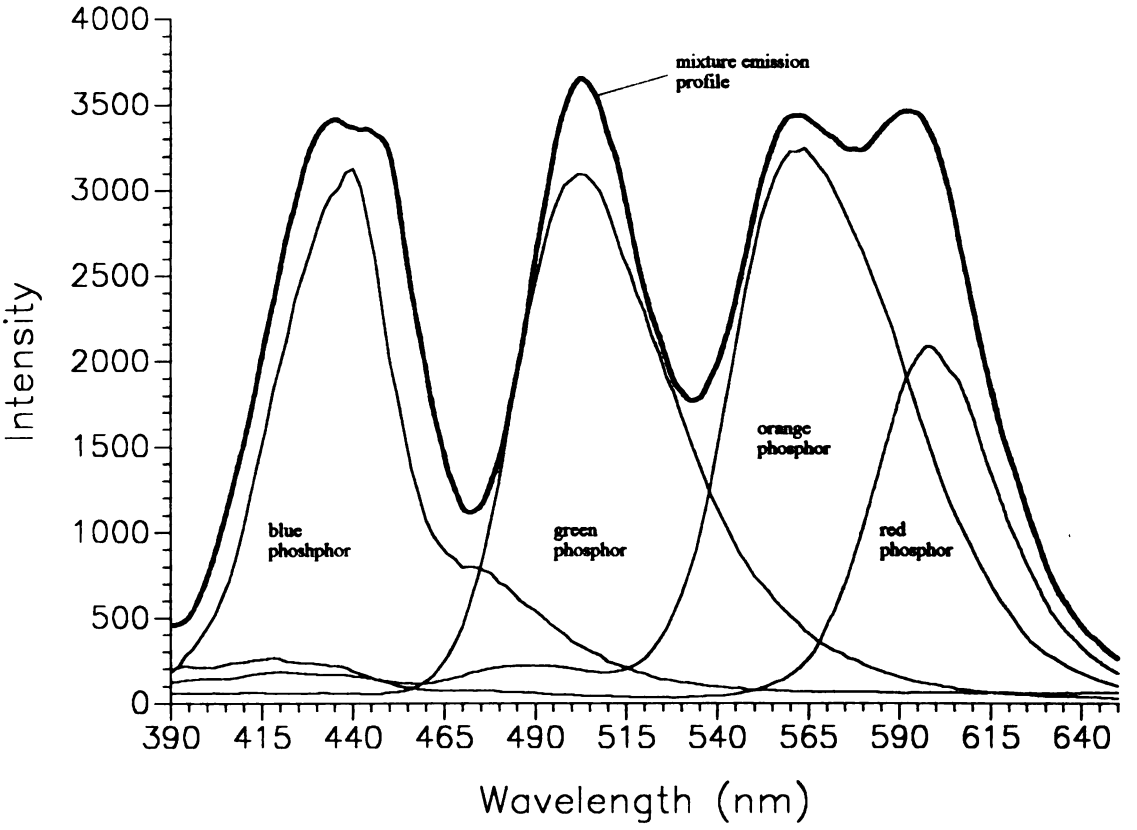

Figure 1-9

Solid State Phosphor Emission Profile

$\lambda ex = 375$ nm

Emission profile for a solid state phosphor embedded in an opaque epoxy matrix. The mixture consisted of yellow, blue, orange, and red fluorescent chalks mixed in experimentally determined proportions to give the resultant broad band output shown. The mixture has good response for λ_{ex} from 260 through 400 nm. The envelope is the emission profile of the mixture excited at 375 nm, while the enclosed peaks are the emission profiles of the pure phosphors, blue, yellow, orange, and red (from left to right).

INSTRUMENTATION FOR ABSORBANCE-CORRECTED SYNCHRONOUS FLUORESCENCE

The instrument pictured in Figure 1-10 was constructed as follows. The sample cell was machined from a black Delrin rod (Cadillac Plastics and Chemical Co., Flint, MI) with an inside diameter of 3.175 mm (1/8 inch). The ends of the cell were tapped to accept the threaded split ring ferrule attached to the common end of the bifurcated fiber optic (Maxlight Optical Waveguides, Inc., Phoenix, Arizona). The opposing ends of the cell were machined to accept either another fiber optic to conduct transmission measurements, or a guide to permit a steady introduction of a brass rod the length of the cell (Figure 1-11). Inlet and outlet ports were tapped to allow sample streams to flow through the cell. The entrance slit of an f3.5 UV/VIS holographic grating monochromator (Model number MC1-02, PTR Optical Co., Waltham, MA) with slits to permit a 4.5 nm bandpass was positioned adjacent to the emission waveguide. A black Delrin housing contained a ultra low dark current photomultiplier tube (PMT Model number S780-5BQ, Hammamatsu Corp, Middlesex, NJ). The transmission was measured from the far end of the cell via a waveguide connected to an identical f3.5 monochromator/PMT housing. The spectral bandpass of the emission monochromator was fixed at 4.5 nm to match the bandpass of the excitation monochromator and reject the high fluorescence background. A UV transmitting filter (Model number 51122, Oriel Corp., Stratford, Connecticut) was placed between the lamp and the excitation monochromator, while either a visible transmitting filter (Model 2A, Eastman Kodak, Rochester, New York), or a visible blocking filter (Model number 51124, Oriel Corp., Stratford, Connecticut), was placed at the entrance slits of both the emission and transmission monochromators to reject stray light.

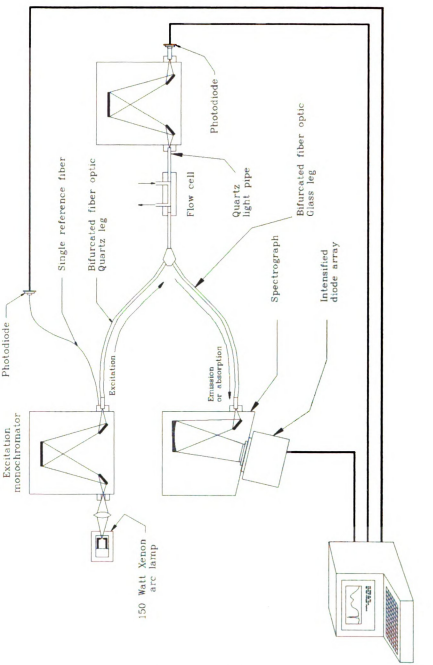

Figure 1-10

Instrumentation for Simultaneous Emission Transmittance Measurements

Instrumentation for the simultaneous measurement of fluorescence and transmittance for determination of the cells transfer function. Shown with the intensified diode array detector as the emission detector.

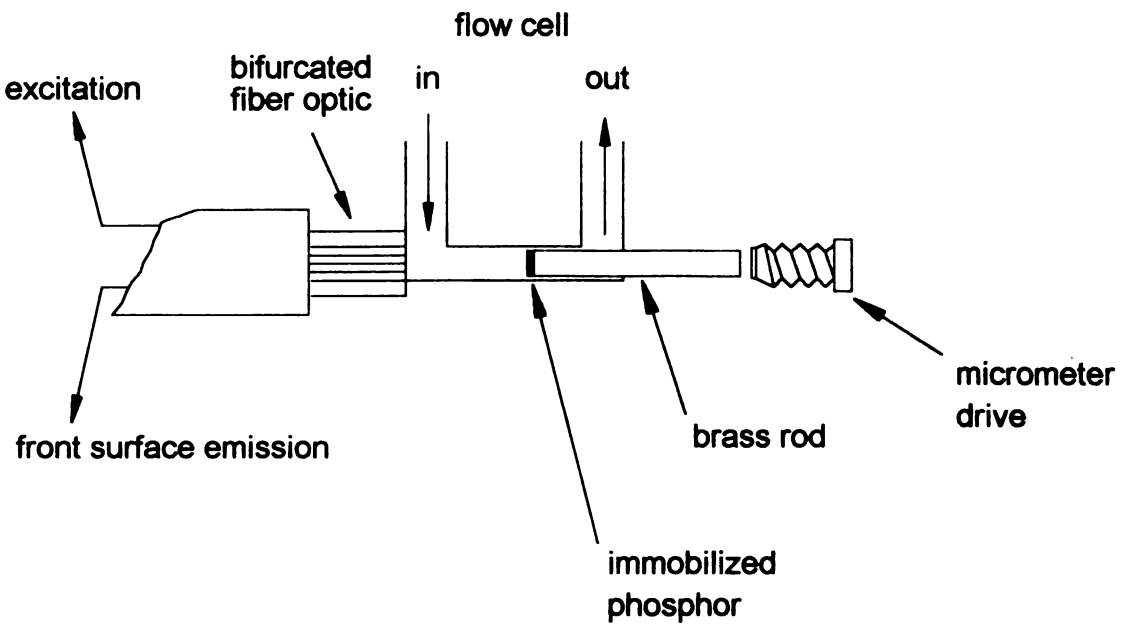

Figure 1-11

Instrumentation Flow Cell for Immobilized Phosphor Study

Shown above is the flow cell configured for measurement of the phosphorescence from the immobilized phosphor. The brass rod was slightly smaller than the cell diameter to permit a trickle flow. This was necessary to prevent the formation of air bubbles in the flow cell.

The excitation source was a high pressure continuous xenon arc lamp (150 W) powered with a constant current power supply (PRA Inc., London, Ontario, Canada). The excitation beam was focused with an *f* 2.8 quartz lens onto the entrance slit of the excitation monochromator. The slit shaped brass ferrule which form the ends of the excitation and emission arms of the bifurcated fiber optic were mated with light tight rubber grommets to the entrance slits of the excitation and emission monochromators. A single fiber split a reference signal from the exit slit of the excitation monochromator to a silicon photocell detector to compensate for source fluctuations. The PMT at the transmission monochromator was set to -250 V, the emission monochromator PMT voltage varied from -400 to -900 V. The entire assembly, exclusive of the arc lamp was placed in a light tight box painted ultra-flat black on the inside. The PMT current output was amplified and converted to a voltage (Model 427, Keithley Instruments, Cleveland, Ohio) with a 10^7 - 10^{10} V/A conversion factor. The output voltages were sampled in rapid sequence by an IBM data acquisition board (Mendelson Electronics Co., Cleveland, OH). The transmission and emission measurements were both bracketed by reference channel measurements of the output of the excitation monochromator. An IBM compatible computer programmed in FORTH (Harvard Softworks, Springboro, Ohio) monitored and controlled experimental conditions while collecting data and providing drive signals for the three stepper motor driven monochromators. Perylene was studied both with the PMT-based system and also using an intensified diode array (Model 6123, Tracor Northern Inc., Middelton, Wisconsin) which was used to simultaneously acquiring the entire emission spectra.

EXPERIMENTAL PROCEDURE

A Soluble fluorophore for Instrument Characterization

To determine the cell parameters it was necessary to know the cell pathlength. This was determined experimentally by measuring the absorbance for 0.0650 g/L $K_2Cr_2O_7$ at 350 nm. The pathlength was thus determined to be 0.974 cm for an absorptivity of 10.71 L/cm-g [93]. In addition to the cell pathlength, determination of H and K via equation 8 requires that transmission measurements be free of stray light and exhibit Beers' law linearity. By regression of absorbance vs fluorescence data for 1,1,4,4-tetraphenylbutadiene, linear response can be verified while simultaneously providing data for our curve fitting programs, Plotit (Scientific Programming Enterprises, Okemos, MI) and Kinfit [115]. Regression of the data about equation 8 provided fitted values for H and K. An absorption maximum at 348 nm was chosen for excitation, while fluorescence was measured at the emission maximum of 450 nm. By setting the excitation monochromator at 348 nm equation 8 can be used, which is the limiting form of equation 7 for low absorbances ($(\varepsilon c)_{ex} = (\varepsilon c)_{em} = 0$).

Results

For solutions of 1,1,4,4-tetraphenylbutadiene, ranging in concentration from 0.0 μg/ml to 30.0μg/ml, linearity to 2.89 absorbance units was observed. A nonlinear least squares fit of the absorbance ($(\varepsilon c)_{ex}$) vs fluorescence data gave the following values for the parameters H and K.

$H = 1.21 \pm 0.11$

$K = 9.42 \pm 0.39$

These values were consistent within experimental error with the earlier work performed by Ratzlaff [110] in our laboratory. Table 1-3 gives determined values of H and K for dansyl

Table 1-3

Regression Fit parameters for Various Soluble Fluorophores		
Fluorescent Probe excitation/emission wavelengths	Regression Fit Parameters $T(x) = G\left(e^{-Hx} - e^{-Kx}\right)$	Comments
1,1,4,4-Tetraphenylbutadiene (in cyclohexane $\lambda_{ex} = 348, \lambda_{em} = 450nm$	H = 1.28 ± 0.16 K = 9.72 ± 0.74	This investigation
Dansyl Chloride (in ethanol) $\lambda_{ex} = 322, \lambda_{em} = 460nm$	H = 1.33 ± 0.14 K = 9.92 ± 0.69	This investigation
Dansyl Chloride (in ethanol) $\lambda_{ex} = 322, \lambda_{em} = 522nm$	H = 1.24 ± 0.20 K = 9.86 ± 0.62	This investigation
Dansyl Chloride (in ethanol) $\lambda_{ex} = 322, \lambda_{em} = 600nm$	H = 1.23 ± 0.17 K = 9.69 ± 0.83	This investigation
Quinine Sulfate (in 0.09 M $HClO_4$) $\lambda_{ex} = 365, \lambda_{em} = 450nm$	H = 1.14 ± 0.18 K = 9.82 ± 0.57	This investigation
Quinine Sulfate (in 0.1 N H_2SO_4) $\lambda_{ex} = 365, \lambda_{em} = 450nm$	H = 1.11 ± 0.05 K = 9.60 ± 0.33	Earlier work [110]
Perylene (in cyclohexane) $\lambda_{ex} = 388, \lambda_{em} = 434nm$	H = 1.07 ± 0.32 K = 8.02 ± 1.69	This investigation (diode array detection)
Perylene (in cyclohexane) $\lambda_{ex} = 388, \lambda_{em} = 468nm$	H = 1.12 ± 0.25 K = 9.24 ± 1.19	This investigation (diode array detection)
Perylene (in cyclohexane) $\lambda_{ex} = 388, \lambda_{em} = 502nm$	H = 1.05 ± 0.26 K = 9.36 ± 0.39	This investigation (diode array detection)

chloride, quinine sulfate, and perylene along with the wavelength settings, solvents, detectors, and the maximum concentration observed for Beers' Law adherence. Figure 1-12 shows the absorbance corrected vs the uncorrected fluorescence intensity curves for 1,1,4,4-tetraphenylbutadiene.

By using several fluorescent probes to implicitly determine the instruments transfer function, we have found good agreement between the predicted and the observed experimental behavior for several probe fluorophores in a variety of solvents and under varying experimental conditions (Table 1-3). Consistent values of the transfer function were observed which are independent of the solvent system, wavelength settings, flow cell, or probe fluorophore.

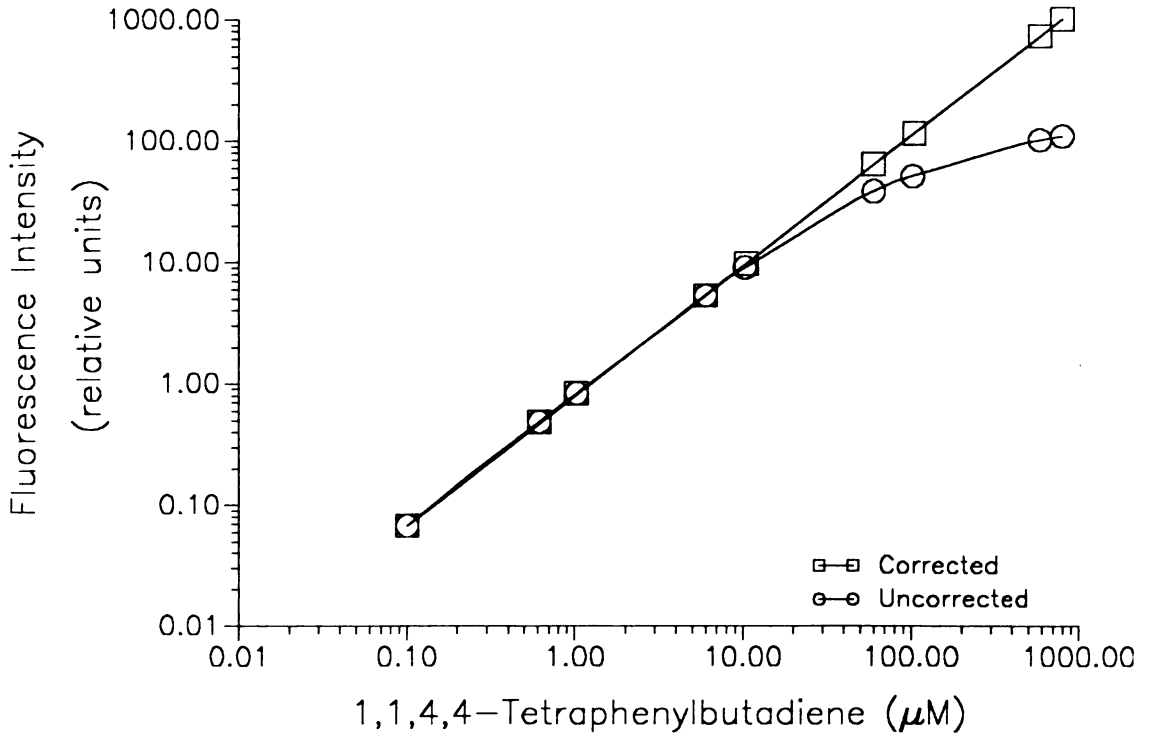

Figure 1-12

1,1,4,4-Tetraphenylbutadiene

λ_{ex} = 348 nm, λ_{em} = 450 nm

Signal vs concentration plots of 1,1,4,4-tetraphenylbutadiene. The correction technique compensates adequately to extend the linearity range 2 decades over the uncorrected data.

An Immobilized Phosphor for Instrument Characterization

We were also able to obtain values for H and K by direct simulating the signal from an infinitely thin slice of a broad band phosphor at varying distances from the front of the cell. This was accomplished by immobilizing an insoluble, solid state, broad band phosphor mixture in an epoxy matrix on a brass rod the same i.d. of the flow cell. A micrometer drive advanced the brass rod from the rear of the cell toward the bifurcated fiber optic (Figure 1-11). By scanning the emission monochromator after each incremental step, a direct determination of the wavelength dependence of the transfer function is obtained. The phosphor mixture had sufficient phosphorescent output to allow determinations to be made for excitation wavelengths from 280 to 400 nm and emission wavelengths from 400 to 600 nm. The composition of our glass fiber optic determined the lower excitation wavelength limited. A brass rod identical to the previous containing only epoxy and decolorizing carbon was used to correct for the background.

Results

Figure 1-13 likewise contains calculated correction factors from equation 10 based on nonlinear regression of distance vs intensity data with equation 6. We have arrived at identical values for the correction factors, but not for the coefficients that determine the transfer function. The direct method determines the transfer function by measuring the phosphorescent scattering intensity versus distance (equation 6), as opposed to the indirect method using soluble fluorophores (equation 7). The coefficient of determination for the curve in Figure 1-14 was $(r^2) = 0.995$, and the standard error of estimate $(SSR)^{1/2} = 0.051$. The magnitude of the determined coefficients are $H = 3.154 \pm 0.17$ and $K = 5.48 \pm 0.22$.

One of the intensity vs distance curves for the phosphor emission is shown in Figure 1-14 along with the regression-determined fit of the data to equation 6. The individual points shown are the sum of 50,000 averages. A large number of data points had to be averaged to keep the standard deviation of any single point below 1%. This is due to the necessary presence of large amounts of decolorizing carbon added to the epoxy resin in which the solid phosphor was immobilized.

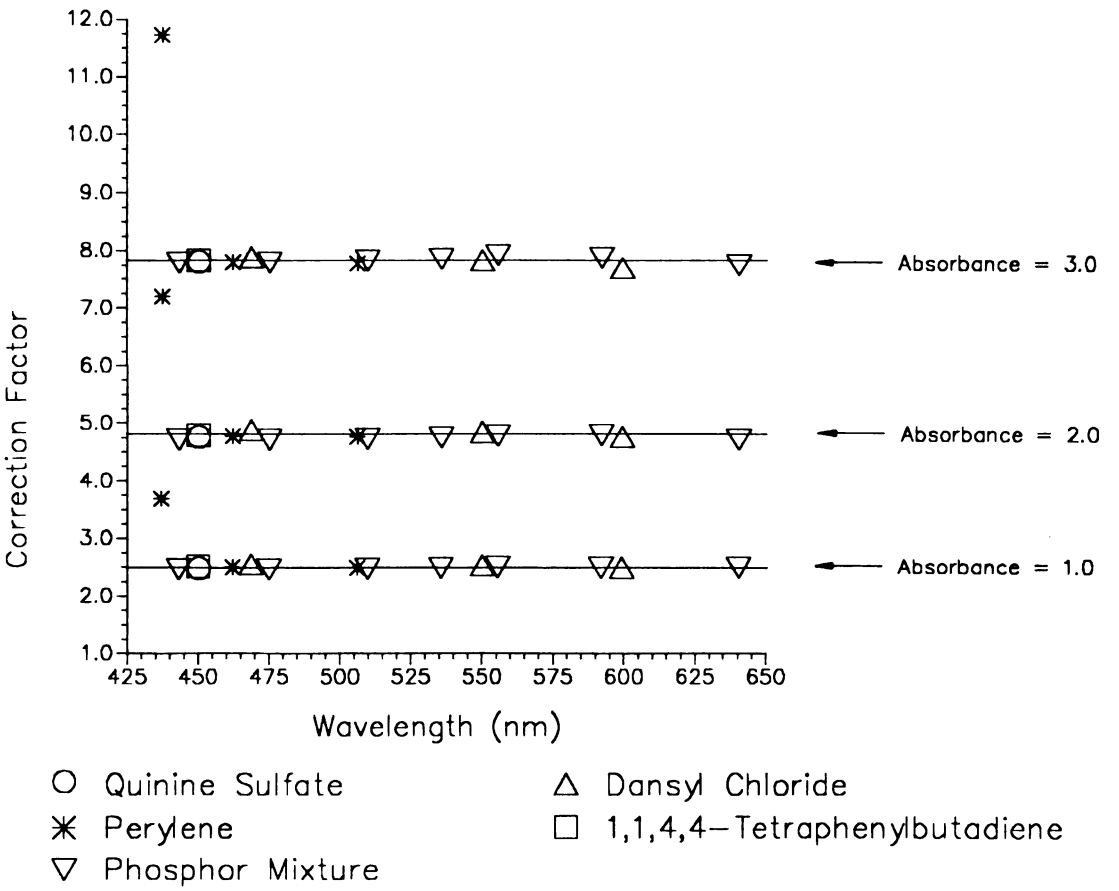

Figure 1-13

Comparison of Calculated Correction Factors

(for several simulated absorbance values)

Comparison of correction factors calculated from the regressed cell parameters H and K. The solid state phosphor measures the fluorescence scattering directly, while the soluble fluorophores implicitly determine a mathematical description of the effective transfer function.

Absorbance Corrected Synchronous Fluorescence

The performance of the instrument in providing absorption corrected synchronous fluorescence data was determined using a mixture of five PAH's identical to the mixture of Latz [92]. The synchronous fluorene emission at 306 nm was determined simultaneously with the solutions' absorbtivity at the excitation and emission wavelengths This was determined in the presence of varying amounts of pyrene. Correction factors determined from the immobilized phosphor study were used to correct the fluorene emission for primary and secondary inner filter effects (Table 1-2, Figure 1-15).

Results

Although mixture 7 had a primary absorbance of 2.49 AU at 301 nm, and secondary absorbance of 2.53 AU at 306 nm (fluorene emission maxima), signal recovery ranged from 109% for mixture 7 to 99% for mixture 2. The percentage relative standard deviations for the corrected synchronous fluorescence fluorene emission in the PAH mixtures are shown in Table 1-4.

Table 1-4

Precision of the Corrected Fluorene Fluorescence Signal vs Pyrene Concentration		
Mixture number	Pyrene conc. (μM)	Percent RSD
1	0.0	1.16
2	9.89×10^{-2}	0.75
3	4.94	0.83
4	9.89	1.05
5	49.44	3.72
6	98.88	4.91
7	197.7	17.54

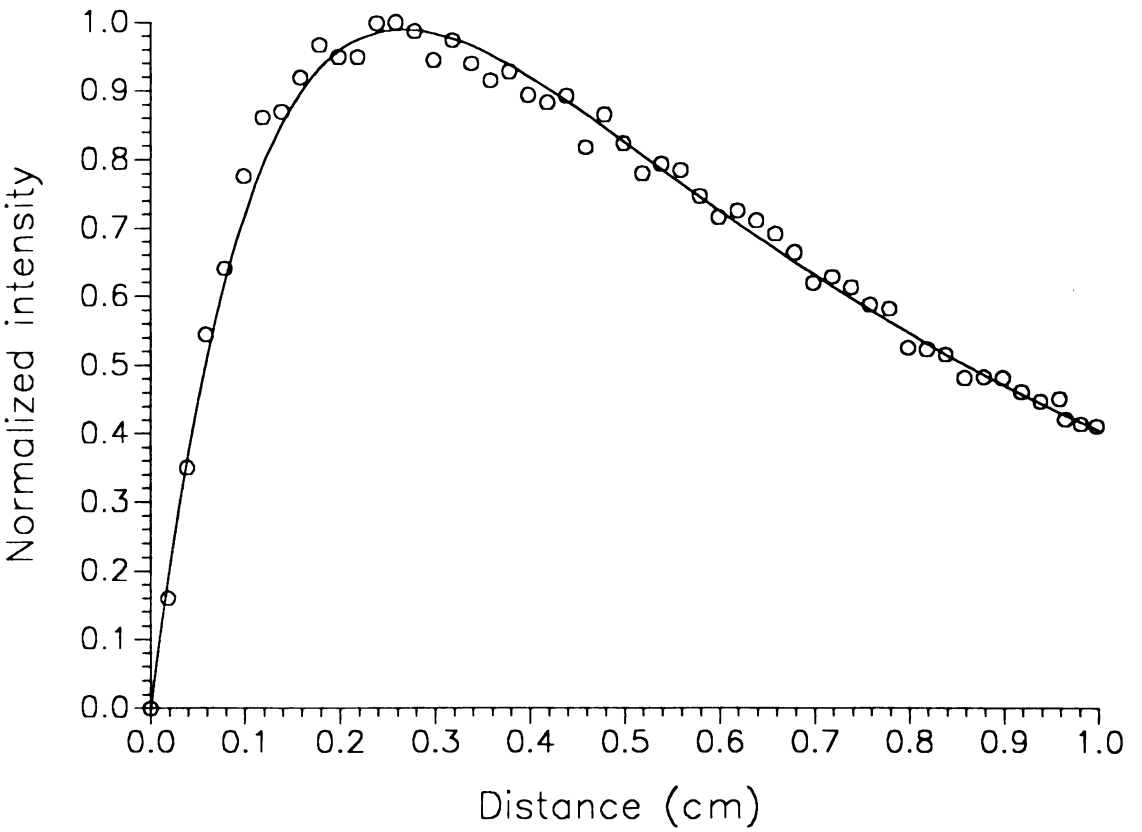

Figure 1-14

Solid State Phosphor Emission Spectra

intensity vs distance λ_{ex} = 290 nm, λ_{em} = 500 nm

Plot of scattering intensity vs distance for a thin layer phosphor. The presence of lampblack in the phosphor mixture helps insure sampling occurs only from the front surface of the solid phosphor probe. The circles are actual data points while the solid line is the calculated best fit to the values of H and K which mathematically define the transfer function $T(x)=G(e^{-Hx} - e^{-Kx})$. The fit is excellent, with a coefficient of determination of 0.994. Maximum scattering was observed 2.8 mm from the front surface of the cell.

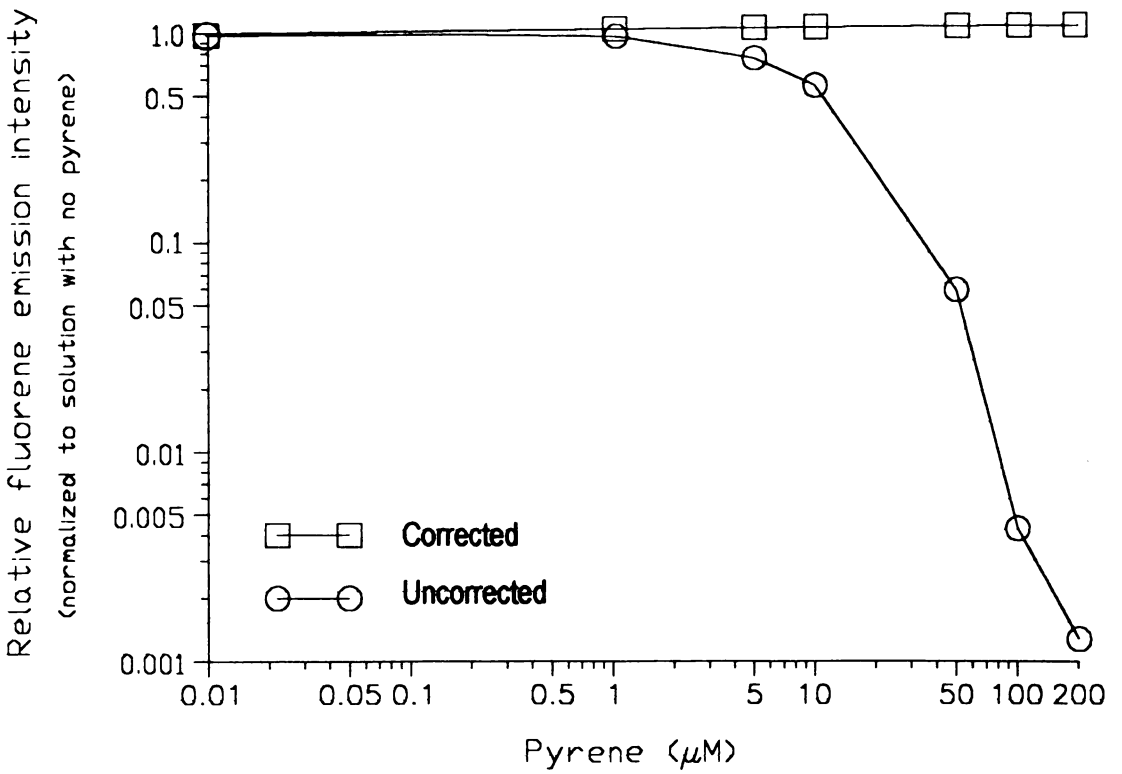

Figure 1-15

Fluorene Intensity vs. Pyrene Concentration

Synchronous scan, λ_{ex} = 301 nm, λ_{em} = 306 nm

Synchronous scan of PAH mixture consisting of fluorene (24.0 μg/mL), phenanthrene (40.0 μg/mL), anthracene (1.0 μg/mL), and perylene (0.06 μg/mL). The fluorene signal is plotted against the concentration of pyrene. The measured absorbance of the mixture containing 40 μg/mL pyrene at λ_{ex} = 301 nm was 2.49 AU and 2.53 AU at λ_{em} = 306 nm. Signal recovery is 109% of theoretical for the 200 μM solution (40.0 μg/mL).

DISCUSSION

Refractive Index Effects

The only physical property of a non-absorbing, non-quenching solvent, which could affect the shape of the transfer curve is its refractive index. Refractive index variations such as those encountered in solvent gradient elution affect how rapidly the beam diverges from the face of the fiber optic. The refractive index also governs the maximum acceptance angle of the isotropic emission signal which will successfully traverse the emission leg of the fiber. Of the solutions analyzed, quinine sulfate was measured in aqueous media (refractive index ca. = 1.333), perylene and 1,1,4,4-tetraphenylbutadiene were measured in cyclohexane (refractive index = 1.420), while dansyl chloride was measured in ethanol (refractive index = 1.359). The refractive indices given are those of the pure solvent. The low concentration of the fluorophores (10^{-4} to 10^{-6} M) should not have an appreciable effect on the solution's refractive index.

As the refractive index increases we should expect a corresponding decrease in the *n.a.* This will reduce the exit angle of the excitation radiation, thus forming a smaller cone which will hold its intensity better further into the cell. Similarly, the reduced acceptance angle of the emission fibers will also form a smaller cone. The effect of a smaller acceptance cone should be offset partially or completely by the more intense excitation cone. If not for the fact that the fiber optic-based fluorometer is limited by the *na.* of the monochromator, system behavior would be solvent and wavelength dependent. A simple filter fluorometer, which is limited by the numerical aperture of the fibers, would require a different model.

The wavelength dependency of the refractive index should have no effect on the experimental results. No likely combination of solvent refractive index and wavelength

settings would provide an effective system n.a. which is fiber limited. Therefore under normal conditions the effective system numerical aperture is that of the monochromators, whose n.a.'s are largely wavelength independent.

Comparison of Immobilized Phosphor vs. Soluble Fluorophore Instrument Characterization Methods

Although our mathematical description of the transfer curve appears valid, the two methods arrived at identical values for the correction factors, but not for the coefficients, H and K, which determine the transfer function. The direct method determines the transfer function by measuring the phosphorescent scattering intensity versus distance (equation 6), as opposed to the indirect method using soluble fluorescent probes (equation 8). The fit parameters for the curve in Figure 1-14 are quite good, $(r^2) = 0.995$, and $(SSR)^{1/2} = 0.051$, however, the coefficients determined by curve fitting the solid phosphor data gave values of $H = 3.154 \pm 0.17$ and $K = 5.48 \pm 0.22$. This range is well beyond the experimental limits of $H = 1.24 \pm 0.20$ and $K = 9.86 \pm 0.62$ obtained via the soluble fluorophore method of determining cell coefficients. Nevertheless, these values provide a series of correction factors (equation 10) which are found to be in good agreement with the values predicted by indirect measurements with the fluorescent probes (Table 1-3). As is shown by equation 9, the correction factor depends not so much on the absolute values of H or K, but on their relative magnitudes. It is reassuring that both methods arrive at virtually identical values for the correction factor (CF) through two different methods of determination; one method being a direct scattering measurement, and another using fluorescence-absorbance-concentration data to implicitly determine cell parameters (Figure 1-13).

Figure 1-12 shows the absorbance corrected vs the uncorrected fluorescence curves for 1,1,4,4-tetraphenylbutadiene. It is significant to note that the only piece of equipment

common to both investigations was the bifurcated fiber optic. The instrumental and procedural dissimilarities between this investigation and an earlier one [110], include solvents (aqueous H_2S0_4 vs. cyclohexane), monochromators, PMTs, flow cells, lamps, data acquisition systems, curve fitting software, sources, amplifiers, and fluorophores. The independence of the transfer curve descriptors H and K from any other experimental variable except the bifurcated fiber optic gives the technique a measure of independence from the experimental variations normally encountered in fluorometry. The empirical mathematical function describing the interaction of the excitation/emission arms of the bifurcated fiber optic is shown to be constant for a particular fiber optic.

Perylene seemed unsuitable for determining cell parameters and correction factors at shorter wavelengths (Figure 1-13). The correction factors determined at 446 nm using 1,1,4,4-tetraphenylbutadiene are valid for simulated absorbances to 3.0 AU (Figure 1-13). The reason is obvious when comparing the perylene emission band at 435 nm (Figure 1-16) to the 1,1,4,4-tetraphenylbutadiene emission band at 446 nm. Perylene exhibits significant self-adsorption at the shorter wavelengths (Figure 1-16), while perylene [116], and dansyl chloride (Figure 1-17) do not. This caveat must be taken into account when choosing a soluble fluorophore for cell characterization. Although perylene proved unsuitable for determination of cell parameters at shorter wavelengths, it could be corrected for primary and secondary inner filter effects using the above methods (Table 1-3). Good linearity was obtained for the perylene signal at 434 nm for absorbances up to 2.5 AU.

The solid phosphor method of cell characterization is immune from self-absorption because the measurement is made from the surface. The phosphor/carbon matrix renders the mixture opaque and precludes the possibility of depth profiling.

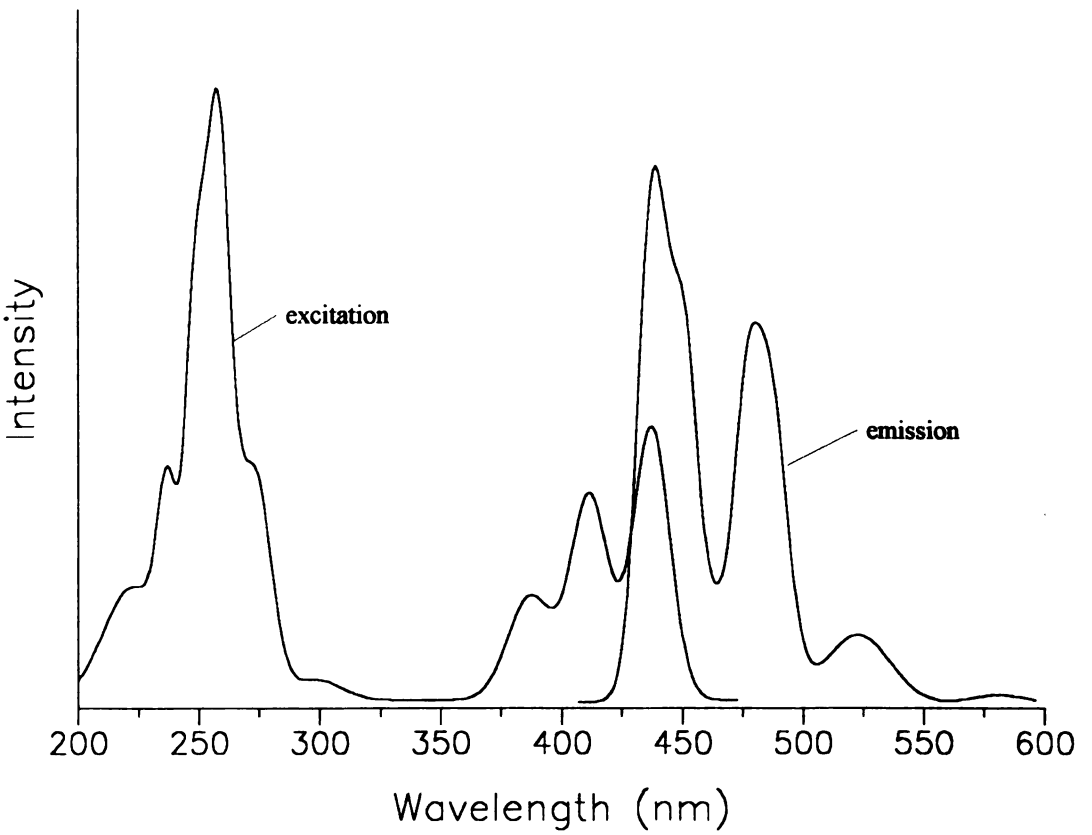

Figure 1-16

Absorbance and Emission Spectrum of Perylene

Strong self absorption at 435 nm is the primary reason perylene derived correction factors fail to agree with correction factors determined by measurements made at alternate wavelengths.

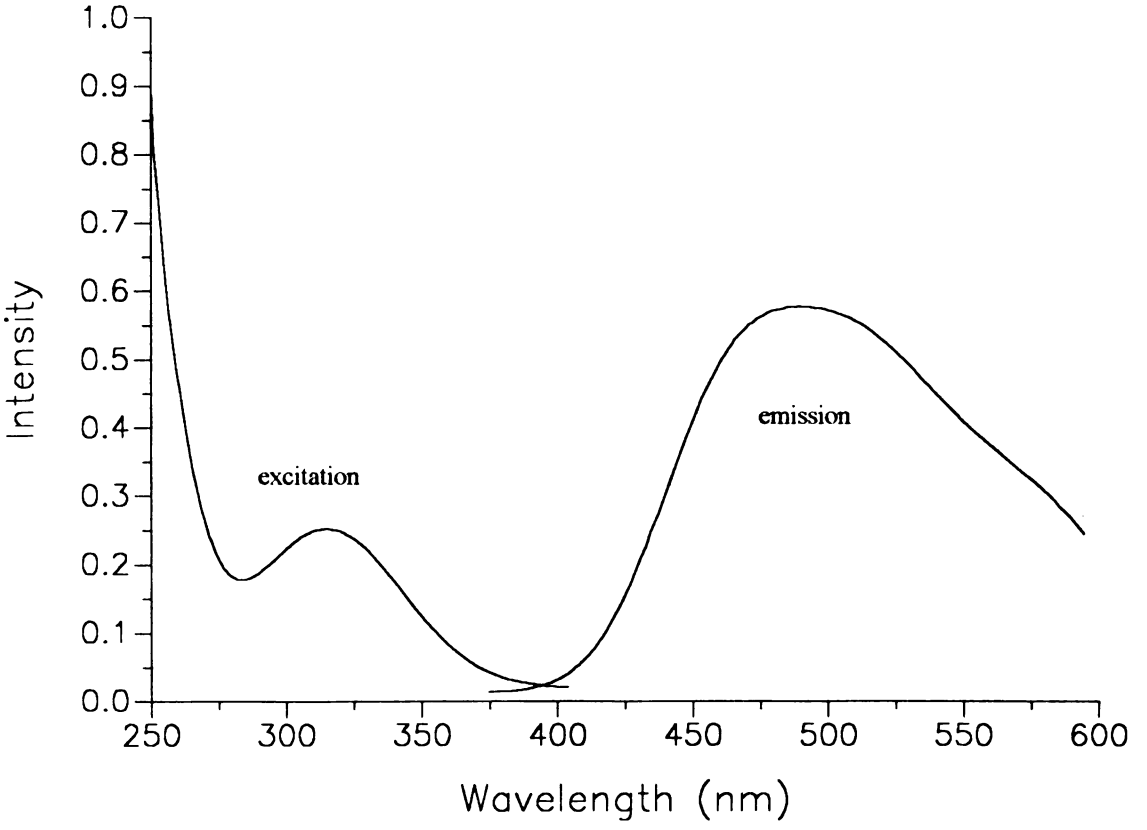

Figure 1-17

Spectra of N-N, Dimethylaminonapthalenesulphonyl Chloride

"Dansyl Chloride"

Unlike perylene, dansyl chloride has minimal overlap of the excitation/emission bands. The lack of any significant self absorption, a high quantum efficiency (0.95), and a broad emission spectra made dansyl chloride a suitable fluorophore for determining cell parameters for the front surface bifurcated fiber optic fluorometer.

Advantages of the Correction Technique in Synchronous Fluorescence Spectrometry

For the correction technique to prove useful in synchronous fluorescence, we must be able to correct for both primary and secondary inner filter effects based on the aggregate absorbances at a single measurements. The design of our instrument allows the simultaneous measurement of absorbances at the excitation and emission wavelengths along with the fluorescence.

Another requisite is that the fluorescence from only one analyte be observed at a time. Earlier investigations by Ratzlaff [110], which corrected for primary inner filter effects in quinine sulfate (QS) due to the presence of varying amounts 1,5-dihydroxybenzoic acid (DHBA), required multiple corrections. The corrected fluorescence of QS with DHBA present was obtained by subtracting the corrected fluorescence of DHBA from that of the QS/DHBA mixture. For fingerprinting unknown mixtures this method is impractical because it requires the preparation of solutions containing the correct concentrations of the interfering chromophore to subtract from the unknown. To perform this correction would require total knowledge of the composition of the "unknown". Synchronous fluorescence has its own built in safeguards against interference by spurious fluorophores. Judicious selection of the scanning difference for either constant wavelength or constant energy synchronous fluorescence renders spurious fluorophores "off scale" when observing the spectral feature of interest. The narrow scanning interval $\Delta\lambda$ in the tail of an absorbance band, and observation in the tip of the emission band, greatly reduces the likelihood of more than one fluorophore contributing to the fluorescence signal.

Disadvantage of the Correction Technique in Synchronous Fluorescence Spectrometry

Synchronous fluorescence based on the Stokes shift is performed in the wings of the excitation and emission bands. Consequently, the fluorophore's absorption cross section is low. Similarly the emission is observed where the quantum efficiency is usually poor. This greatly complicated our obtaining acceptable S/N with a front surface fiber optic based fluorometer. Our detection limit for perylene is over 400 times greater than that of a commercial right angle geometry fluorometer. This poor detection limit is in spite of the fact that the reported quantum efficiency of perylene is between 0.96 - 1.0 [116].

At high pyrene concentrations additional signal averaging became necessary to recover the fluorene signal with a satisfactory signal-to-noise (S/N) ratio. At 200 μM (40.4 mg/ml), the measured absorbance at the excitation wavelength of fluorene was ($(\varepsilon c)_{ex}^{301}$ = 2.49 AU), while the absorptivity at the emission wavelength was ($(\varepsilon c)_{em}^{306}$ = 2.53 AU). The net total solution absorbtivity from primary and secondary inner-filter effects relative to an optically clear solution is ($10^{-(2.49 + 2.53)} = 10^{-5.02}$ = 9.56×10^{-6}) for a 1 cm pathlength. A numerical integration of the curve in Figure 1-14 shows 90% of the observed fluorescence occurs within the first 7 mm.

Wavelength Dependency of the Transfer Function

Our concern for the applicability of the technique to synchronous fluorescence required that we characterize the transfer function over the entire wavelength range a synchronous fluorometer might encounter. To characterize the transfer functions at all possible excitation/emission combinations would require finding a series of fluorophores with which to calibrate the instrument. These fluorophores would have to cover all possible combinations of excitation and emission wavelengths. Other investigators have reported

significant errors for fiber optic based fluorometers when the correction technique doesn't take into account refractive index effects of polychromatic signals due to the emission and absorbance monochromators wide spectral bandpasses [117].

Fortunately the wavelength dependence of the transfer function is that of the smallest numerical aperture of the system. The limiting numerical aperture initially appears to be that of the monochromators, which are f/3.5. The *f/#* of the fiber is related to the numerical aperture by $f/\# = n.a. / 2 * \tan(\theta_0)$ [113]. Because the fibers are immersed in cyclohexane with a refractive index of 1.420, the effective numerical aperture is thus $0.2 / 1.42 = 0.14$. This makes the wavelength dependent range of the fibers effective *f/#* between 1.7 - 3.8 over the wavelength region from 350 - 650 nm [118]. When compared to the monochromators wavelength independent [113] $f/\#$ of 3.5 over the same wavelength region, the limiting aperture of the instrument over most of the wavelength region is due to the monochromator's *n.a.* Since the effective *n.a.* of the monochromators is wavelength independent, we would expect the synchronous scanning of the excitation and emission wavelengths may show some wavelength dependencies in our determination of the transfer function.

Other investigators have described an effective *n.a.* [96, 114, 119 -122]; a measured quantity that is noticeably smaller than the calculated *n.a.* based on the manufacturer's literature. This is due to the fiber's measured emission efficiency decreases from a maximum value to near the center of the fiber to near zero [96, 119-120]. The gaussian beam profile concentrates over 96% of the emitted radiation in roughly the center 1/2. This has the effect of reducing the fibers effective numerical aperture to roughly 1.18 (or $f/\# \approx 4.0$).

Other Instrumentation Factors Affecting the Efficiency of Absorption Corrections

The poor response at higher concentrations is symptomatic of several conditions inherent in this study. The fiber optic being faster than the monochromators tends to overfill the entrance slits, thereby increasing stray light. The monochromators are physically small and optically fast. Their small size pre-empts the presence of any internal baffling. The stray light levels probably lowered our the detection limits considerably.

Crosstalk within our laboratory's bifurcated fiber optic bundle severely limits the minimum detectable signal. This was quantitated by immersing the common end of the fiber in a non-fluorescing, highly absorbing solution of 0.35 M $KMnO_4$. The signal at 535 nm was compared to the signal obtained from a polished reflector at a distance of 3 mm. This experiment was conducted in a modified cell with a 1 cm. diameter bore (to eliminated scattering contributions from the cell wall). The difference in signal intensity between the two experiments is roughly proportional to the noise due to crosstalk between the excitation/emission fibers within the cladding. Crosstalk was observed to be 2.5% of the full scale signal (the signal measured with the reflector in place). Through its long tenure in our laboratory, 8 of the 40 fibers became broken due to normal wear and tear. This probably contributes significantly to the level of noise due to crosstalk among the excitation/emission fibers in the common arm of the bifurcated fiber.

The noise attributable to crosstalk is rather large relative to the scale of the fluorene-pyrene experiment. Although only 2.5% of transmitted radiation appears as stray light, we must keep in mind that this is 2.5% of the excitation beam from the Xe arc lamp through the excitation monochromator. When compared to the intensity of the fluorescence from fluorene, this represents a stray light level that is over 5000 times as great as the signal obtained from the most concentrated (200 μM) fluorene solution. This large stray light

signal due to crosstalk alone is separated from the fluorene fluorescence signal by 5 nm. A single data point of the fluorene fluorescence signal was typically only 8-12 A-to-D counts measured against a background of 2800 to 3300 counts.

CONCLUSIONS

In conclusion we have been able to correct for primary and secondary inner filter effects when conditions permit gathering a fluorescence measurement with an adequate signal-to-noise ratio. The addition of the transmittance monochromator to reject stray fluorescence makes our instrument an excellent spectrometer for strong fluorophores. We can measure absorbances linear to 3 AU reliably despite a high fluorescence background. The source of most of the error in correcting a fluorescence measurement for absorbance arises from our large RSD in the fluorescence measurement. The major source of this is low throughput due to combined primary and secondary absorbances of over 5 AU. We can however recognize a problematic sample by noting the primary and secondary absorbances.

Clearly our instrument is somewhat over-extended for the more concentrated solutions. However, even for mixture 6, where pyrene is present at 100 μM, the RSD of our measurement falls to a respectable 4.91% (Table 1-4). Without the benefit of any correction, the original investigators could recover ≈2% of the expected fluorene fluorescence [92, 114].

REFERENCES:

1 . Genesis 9:13

2. J.B.F. Lloyd, *Nature* (London), **231**, 64 (1971).

3 . T. Masaki, F. Motohisa, *Analyst* (London), **117(9)**, 1485 (1993).

4 . G.I. Romanovskaya, V.M. Pivovarov, A.K. Chibisov, *Zh. Anal. Khim.*, **42(8)**, 1401 (1987).

5 . L.A. Spino, D.W. Armstrong, T. Vo-Dinh, *J. Chromatography.*, 409, 147 (1987).

6 . D.W. Abbot, R.L. Moody, R.M. Mann, T. Vo-Dinh, *J. Am. Ind. Hyg. Assoc.*, **47(7)**, 379 (1986).

7 . K. Nithipatikom, L.B. McGown, *Applied Spectroscopy*, **41(3)**, 395 (1987).

8 . L.A. Files, M.A. Mignardi, J.D. Winefordner, *J. Microchem.*, **36(1)**, 122 (1987).

9 . M. Furusawa, M. Tachibana, M. Fujishima, *Bull. Chem. Soc. Jpn.*, **56(11)**, 3509 (1983).

10 . M. Tachibana, M. Furusawa, *Bull. Chem. Soc. Jpn.*, **56(8)**, 2254 (1983).

11 . T. A. Kubic, F. X. Sheehan, *J. Forensic Sci.*, **28(2)**, 345 (1983).

12 . T. A. Kubic, C. M. Lasher, J. Dwyer, *J. Forensic Sci.*, **28(1)**, 186 (1983).

13 . E. L. Inman Jr, J. D. Winefordner, *Anal. Chem.*, **54(12)**, 2018 (1982).

14 . M. Furusawa, M. Tachibana, Y. Hayashi, *Bunseki Kagaku*, **31(5)**, 229 (1982).

15 . T. Vo-Dinh, P. R. Martinez, *Anal. Chim. Acta*, **125**, 13 (1981).

16 . J. B. F. Lloyd, I. W. Evett, J. M. Dubery, *J. Forensic Sci.*, **25(3)**, 589 (1980).

17 . J. B. F. Lloyd, *Analyst (London)*, **105(1247)**, 97 (1980).

18 . L. A. Spino, D. W. Armstrong, T. Vo-Dinh, *J. Chromatogr.*, **409**, 147 (1987).

19 . M. J. Kerkhoff, J. D. Winefordner, *Anal. Chim. Acta*, **175**, 257 (1985).

20 . T. Kato, S. Yokoyama, Y. Sanada, *Fuel*, **59(12)**, 845 (1980).

21 . M. Lazaro, A. Bermejo, H. Garcia, J. S. Rodriguez, *Fresenius' J. Anal. Chem.*, **343(6)**, 509 (1992).

22 . M. D. Prat, J. Guiteras, R. Compano, J. L. Beltran, *J. Fluoresc.*, **1(4),** 267 (1991).

23 . T. Naohide, C. Yamamura, Y. Masami, *Sekiyu Gijutsu Kyokaishi*, **56(3)**, 254, (1991).

24 . G. Morel, O. Samhan, P. Literathy, H. Al-Hashash, L. Moulin, T. Saeed, K. Al-Matrouk, M. Martin-Bouyer, A. Saber; et al., *Fresenius. J. Anal. Chem.*, **339(10),** 699 (1991).

25 . L. D'Huicque, O. E. Troccoli, Possidoni de Albinati, J. Flavia, *Acta Bioquim. Clin. Latinoam.*, **23(2),** 223 (1989).

26 . T. A. Taylor, H. H. Patterson, *Anal. Chem.*, **59(17),** 2180 (1987).

27 . S. G. Wakeham, *Environ. Sci. Technol.*, **11(3),** 272 (1977).

28 . P. Baudot, M. L. Viriot, J. C. Andre, J. Y. Jezequel, M. Lafontaine, *Analusis,* **19(3),** 85 (1991).

29 . Y. Weixi, C. Wenxian, X. Tao, X. Xiaobai, *Chin. Chem. Lett.*, **2(7)**, 551, (1991).

30 . Y. Du, Y. Yaoguo, L. Liansheng, S. Jinghong, *Kankyo Kagaku Kenkyu Hokoku (Chiba Daigaku),* **14**, 45 (1989).

31 . J. Wang, S. Chen, C. Shuqun, *Ziran Kexueban*, **(1),** 109 (1987).

32 . T. Vo Dinh, G. H. Miller, N. K. Wilson, *Proc. - APCA Annu. Meet., 79th (Vol. 2)*, **86/32.2**, (1986).

33 . L. A. Files, B. T. Jones, S. Hanamura, J. D. Winefordner, *Anal. Chem.*, **58(7),** 1440 (1986).

34 . T. Vo Dinh, *Indoor Air, Proc. Int. Conf. Indoor Air Qual. Clim., 3rd, Volume 4*, Issue PB85-104214, 325-30. Swed. Counc. Build. Res.: Stockholm (1984).

35 . M. J. Kerkhoff, T. M. Lee, E. R. Allen, D. Lundgren, A. Dale, J. D. Winefordner, *Environ. Sci. Technol.*, **19(8),** 695 (1985).

36 . T. Vo-Dinh, D. W. Abbott, *Environ. Int.*, **10(4),** 299 (1984).

37 . T. Vo Dinh, T. B. Bruewer, R. H. Jungers, T. J. Wagner, *Spec. Conf.: Meas. Monit. Non-Criter. (Toxic) Contam. Air*, **208**. Edited by: Frederick, Edward R. APCA: Pittsburgh, Pa. (1983).

38 . T. Vo-Dinh, T. J. Bruewer, G. C. Colovos, T. J. Wagner, R. H. Jungers, *Environ. Sci. Technol.*, **18(6),** 477 (1984).

39. R. H. Jungers, *NATO ASI Ser., Ser. C, 112 (Mobile Source Emiss. Incl. Polycyclic Species)*, **115** (1983).

40. T. Vo-Dinh, R. B. Gammage, P. R. Martinez, *Anal. Chem.*, **53(2),** 253 (1981).

41. J. Dujmov, P. Sucevic, *Chem. Ecol.*, **4(4)**, 189 (1990).

42. I. Kasa, G. Bajnoczy, M. Nagy, *Period. Polytech., Chem. Eng.*, **28(3-4),** 243 (1984).

43. F. J. Purcell, R. Kaminski, R. H. Obenauf, *ASTM Spec. Tech. Publ., 863 (Adv. Lumin. Spectrosc.)*, 81 (1985).

44. D. Stainken, U. Frank, *Bull. Environ. Contam. Toxicol.*, **22(4-5),** 480 (1979).

45. J. C. Andre, M. Bouchy, P. Baudot, M. Niclause, *C. R. Hebd. Seances Acad. Sci., Ser. C*, **284(17),** 667 (1977).

46. P. John, I. Soutar, *Proc. Anal. Div. Chem. Soc.*, **13(10),** 309 (1976).

47. D. M. Stainken, U. Frank, *ASTM Spec. Tech. Publ.*, 1062 (Waste Test. Qual. Assur.: Second Vol.), 381 (1990).

48. D. W. Abbott, R. L. Moody, R. M. Mann, T. Vo-Dinh, *Am. Ind. Hyg. Assoc. J.*, **47(7),** 379 (1986).

49. T. Vo-Dinh, R. B. Gammage, A. R. Hawthorne, *Report, CONF-781039-8, Avail. NTIS From: Energy Res. Abstr.* **4(6),** Abstr. No. 14148 (1979).

50. T. Vo Dinh, *Anal. Chem.*, **50(3),** 396 (1978).

51. Z. Zhao, W. Quan, *J. Environ. Sci. (China)*, **1(2)**, 109 (1989).

52. AU Zhao, Zhenhua; W. Quan, *Huanjing Kexue Xuebao*, **8(2)**, 242 (1988).

53. M. Uziel, R. J. Ward, T. Vo-Dinh, *Anal. Lett.*, **20(5),** 761 (1987).

54. K. Vahakangas, A. Haugen, C. C. Harris, *Carcinogenesis (London)*, **6(8),** 1109 (1985).

55. M. Tachibana, M. Furusawa, *Bull. Chem. Soc. Jpn.*, **56(8),** 2254 (1983).

56. F. Capitan, G. Sanchez-Palencia, A. Navalon, *Anal. Chim. Acta*, **259(2),** 345 (1992).

57. J. L. Beltran, R. Compano, A. Izquierdo, M. A. Pladellorens, M. D. Prat, *Appl. Fluoresc. Technol.*, **3(6),** 6 (1991).

58 . S. E. Cabaniss, *Environ. Sci. Technol.*, **26(6),** 1133 (1992).

59 . F. Capitan, E. Manzano, A. Navalon, J. L. Vilchez, L. F. Capitan-Vallvey, *Talanta*, **39(1),** 21 (1992).

60 . F. Capitan, A. Navalon, E. Manzano, L. F. Capitan-Vallvey, J. L. Vilchez, *Fresenius. J. Anal. Chem.*, **340(1),** 6 (1991).

61 . J. M. Cano Pavon, A. Garcia de Torres, M. E. Urena Pozo, *Talanta*, **37(4),** 385 (1990).

62 . F. Salinas, A. Munoz de la Pena, L. F. Capitan-Vallvey, A. Alberto, *Analyst (London)*, **114(10)**, 1297 (1989).

63 . M. W. Kabbani, S. Rubio-Borroso, L. M. Polo-Diez, *Anal. Chim. Acta*, **218(1),** 167 (1989).

64 . F. Salinas, A. Munoz de la Pena, M. S. Duran, *Anal. Lett.*, **21(8),** 1457 (1988).

65 . A. Munoz de la pena, F. Salinas, M. Sanchez, M. Elena, A. Jose, *Analyst (London)*, **113(9),** 1435 (1988).

66 . F. Garcia Sanchez, J. C. Marquez Gomez, M. Hernandez Lopez, *Analyst (London)*, **112(5),** 649 (1987).

67 . M. Urena Pozo, G. de Torres Encarnacion, C. P. Amparo; *Anal. Chem.*, **59(8),** 1129 (1987).

68 . F. Garcia Sanchez, M. Hernandez Lopez, *Talanta*, **33(10),** 785 (1986).

69 . F. Salinas, A. Munoz De la Pena, F. Munoz De la Pena, *Mikrochim. Acta*, **3(5-6),** 361 (1986).

70 . M. Salgado, E. Urena, A. Garcia de Torres, J. M. Cano Pavon, *J. Mol. Struct.*, **143,** 477 (1986).

71 . F. Garcia Sanchez, A. Navas, M. Santiago, *Anal. Chim. Acta*, **167,** 217 (1985)

72 . S. Rubio, A. Gomez-Hens, M. Valcarcel, *Anal. Chem.*, **57(6),** 1101 (1985).

73 . G. I. Romanovskaya, V. M. Pivovarov, A. K. Chibisov, *Zh. Anal. Khim.*, **42(8),** 1401 (1987).

74 . D. Chen, M. D. Luque de Castro, M. Valcarcel, *Anal. Chim. Acta*, **261(1-2),** 269 (1992).

75 . D. G. Konstantianos, P. C. Ioannou, C. E. Efstathiou, *Analyst (London)*, **116(4),** 373 (1991).

76 . P. Izquierdo, M. C. Gutierrez, A. Gomez-Hens, D. Perez-Bendito, *Anal. Lett.*, **23(3),** 487 (1990).

77 . G. I. Romanovskaya, A. K. Chibisov, *Zh. Anal. Khim.*, **43(6),** 1120 (1988).

78 . A. Munoz de la Pena, F. Salinas, I. D. Meras, *Anal. Chem.*, **60(22),** 2493 (1988).

79 . F. Garcia Sanchez, C. Cruces, A. L. Ramos Rubio, *J. Mol. Struct.*, **143,** 473 (1986).

80 . T. Vo Dinh, *Appl. Spectrosc.*, **36(5),** 576 (1982).

81 . Y. Li, X. Huang, J. Xu, G. Chen, *Anal. Chim. Acta*, **256(2),** 285 (1992).

82 . Y. Li, X. Huang, *Fenxi Huaxue*, **17(12),** 1154 (1989).

83 . M. J. Kerkhoff, L. A. Files, J. D. Winefordner, *Anal. Chem.*, **57(8),** 1673 (1985).

84 . L. A. Files, M. Moore, M. J. Kerkhoff, J. D. Winefordner, *Microchem. J.*, **35(3),** 305 (1987).

85 . M. J. Kerkhoff, E. L. Inman Jr., E. Voigtman, L. P. Hart, J. D. Winefordner, *Appl. Spectrosc.*, **38(2),** 239 (1984).

86 . E. L. Inman Jr., J. D. Winefordner, *Anal. Chim. Acta*, **141,** 241 (1982).

87 . L. A. Files, J. D. Winefordner, *J. Agric. Food Chem.*, **35(4),** 471 (1987).

88 . J. C. Andre, P. Baudot, V. Loppinet, *Anal. Lett.*, **19(9-10),** 987 (1986).

89 . S. Rubio, A. Gomez-Hens, M. Valcarcel, *Talanta*, **33(8),** 633 (1986).

90 . E. L. Inman, L. A. Files, J. D. Winefordner, *Anal. Chem.*, **58(11),** 2156 (1986).

91 . E. L. Inman Jr., J. D. Winefordner, *Anal. Chim. Acta*, **138,** 245 (1982).

92 . H.W. Latz, A.H. Ullman, J.D. Winefordner, *Anal. Chem.*, **50**, 2148 (1978).

93 . N.W. Tietz, Fundamentals of Clinical Chemistry, W.B. Saunders; Philadelphia, PA., (1976).

94 . M. M. Puchalski, M. J. Morra, R. Von Wandruszka, *Fresenius. J. Anal. Chem.*, **340(6),** 341 (1991).

95 . H. K. Chung, J. D. Ingle Jr., *Anal. Chem.*, **62(23),** 2541 (1990).

96 . C. M. Yappert, J. D. Ingle Jr., *Appl. Spectrosc.*, **43(5),** 759 (1989).

97 . K. Wiechelman, *Am. Lab.*, **18**, 49 (1986).

98 . J. Batke, *Anal. Biochem.*, **121**, 123 (1982).

99 . H. P. Lutz, P. L. Luisi, *Helv. Chim. Acta*, **66(7),** 1929 (1983).

100 . F. Van Geel, E. Voightman, J.D. Winefordner, *Appl. Spectrosc.*, **38**, 228 (1984).

101 . J.F. Holland, R.E. Teets, A. Timnick, *Anal. Chem.*, **49**, 706 (1973).

102 . D.R. Christmann, S.R. Crouch, A. Timnick, *Anal. Chem.*, **53**, 2040 (1981).

103 . K. Adamsons, J.E. Sell, J.F. Holland, A. Timnick, *Am. Lab.*, **16**, 16 (1984).

104 . M. L. Mertens, J. H. R. Kaegi, *Anal. Biochem.*, **96(2),** 448 (1979).

105 . A. Novak, *Collect. Czech. Chem. Commun.*, **43(11),** 2869 (1978).

106 . R. A. Leese, E. L. Wehry, *Anal. Chem.*, **50(8),** 1193 (1978).

107 . V. A. Mode, D. H. Sisson, *Anal. Chem.*, **46(2),** 200 (1974).

108 . J.B.F. Lloyd, *Anal. Chem.*, **52(1)**, 189 (1980).

109 . T. Vo-Dinh, *Appl. Spect.*, **36(5)**, 576 (1982).

110 . E.H. Ratzlaff, R.G. Harfmann, S.R. Crouch, *Anal. Chem.*, **56**, 342 (1984).

111 . D.G. Mitchell, J.S. Garden, K.M. Aldous, *Anal. Chem.*, **48**, 2275 (1976).

112 . R. van Slageren, G. den Boef, W.E. van der Linden, *Talanta*, **20**, 501 (1973).

113 . J. Ingle, S.R. Crouch, *Spectrochemical Analysis*, Prentice Hall, Engelwood Cliffs, New Jersey, 1988.

114 . R.M. Smith, K.W. Jackson, K.M. Aldous, *Anal. Chem.*, **49**, 2051 (1977).

115 . J.L. Dye, V.A. Nicely, *J. Chem. Ed.*, **48**, 443 (1971).

116 . J.N. Miller, *Standards in Fluorescence Spectrometry*, Chapman and Hall, London; New York, 1981.

117 . M. C. Yappert, J. D. Ingle, *Appl. Spect.*, **43,** 759 (1989).

118 . I.D. Caldwell, Highlight Fiber Optics, Product brochure MR-3, 1986.

119 . Z.Y. Zhu, M.C. Yappert, *Appl. Opt.*, **46**, 919 (1992).

120 . C. Komives, J. S. Schultz, *Talanta*, **39(4),** 429 (1992).

121 . Z.Y. Zhu, M.C. Yappert, *Appl. Opt.*, **46**, 912 (1992).

122 . T. Deaton, *Instrumentation and Methodology for Remote Fiber Fluorimetry*, Ph.D. dissertation, University of California at Davis (1984).

CHAPTER 2

A MATHEMATICAL MODEL
FOR THE BIFURCATED FIBER OPTIC FLUOROMETER

Historical

Since the inception of remote sensing via fiber optics [1], several authors have performed comprehensive reviews the analytical applications of fiber optic based sensors [2 -5]. The small size of fiber optic based sensors permits measurements on small volumes, in flowing streams in remote or inhospitable environments. The analytical volume viewed by a fiber optic probe has also been the subject of intense theoretical [6 -14] and experimental study [15]. Ideally we would like to derive an accurate equation which describes the interaction of the overlapping excitation/emission fibers of a bifurcated fiber optic fluorometer. Given the physical dimensions and composition of the fibers, claddings, flow cell, and solvent properties, it should be possible to derive an accurate equation describing such a fluorometer. Previous investigators have developed mathematical [16] and semi-empirical models [15, 17] describing the behavior of bifurcated fiber optic based instruments. Unfortunately, for the case of a bifurcated fiber optic with 63 total fibers, the expression involves 63 triple integrals. Although the expression can be written, an exact solution is difficult. It is possible to write an exact expression which is integrable for the case of a bifurcated optics consisting of only two fibers [6-8, 16-17]. Different investigators have explored the case of two fibers with fiber axis geometry's ranging from perpendicular to collinear [8, 18].

Theoretical Basis of the Mathematical Model

We can reduce the complexity of the mathematics via a numerical approximation relying on computing power and an accurate model. The model used creates a two dimensional array in memory. Each element of the array is analogous to a type of combination sensor/emitter. This computer simulated array of fibers and sensors is shown graphically in Figure 2-1. As mentioned earlier, the expression for the intensity from an infinitely thin slice at a known distance from the front surface of the cell is given by

$$F_O = P_0(\varepsilon c)_f G\left[\frac{1}{H}\left(1-e^{-Hb}\right)-\frac{1}{K}\left(1-e^{-Kb}\right)\right]$$

We can, by plotting the intensity vs distance, generate a curve that when fit to the equation will give valid fit parameters for H and K. This has allowed for generation of a correction factor based on the intrinsic physical properties of the analyte and the fiber optic fluorometer.

At zero distance into the cell, the finite width of the cladding prevents any sensor from being both illuminated and observed (Figure 2-2). Simulation of measuring from successive distances is performed by expanding the illumination radius of the excitation fiber to cover additional sensors. The increase in radius is calculated from the known numerical aperture of the fibers and the solvent refractive index. Simultaneously, the intensity reaching each sensor is reduced in proportion to the gain in the area illuminated.

Each sensor is thus compared to each fiber to determine how many fibers are illuminating the particular sensor. The known radiant intensity per fiber times the number of fibers illuminating a particular sensor gives the total illumination received by a selected sensor (Figure 2-1). Having accurately calculated the total excitation energy received by a particular sensor, the next task is to calculate how many observation fibers view the sensor.

This is not as straightforward as it may seem. As mentioned earlier, all light striking a fibers face is not necessarily transmitted. The effective numerical aperture of the fiber, which is usually monochromator limited, determines the minimum angle at which entering

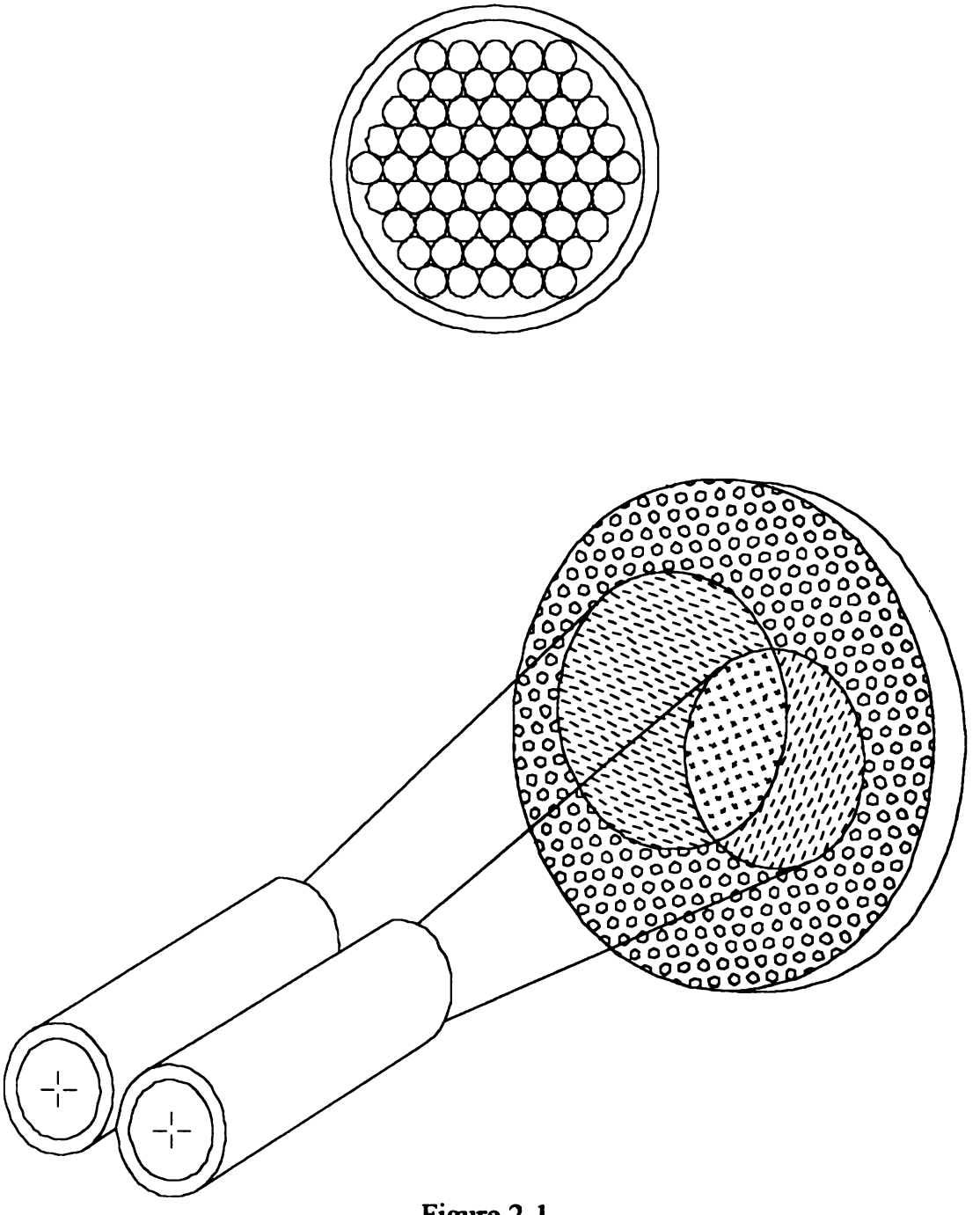

Figure 2-1

Pictorial View of Computer Simulation Model

The model simulates the observed fluorescence intensity vs distance by moving a computer generated sensor array relative to the fiber bundle. Each sensor array measures the simulated light intensity at various distances and generates an appropriate simulated fluorescence response.

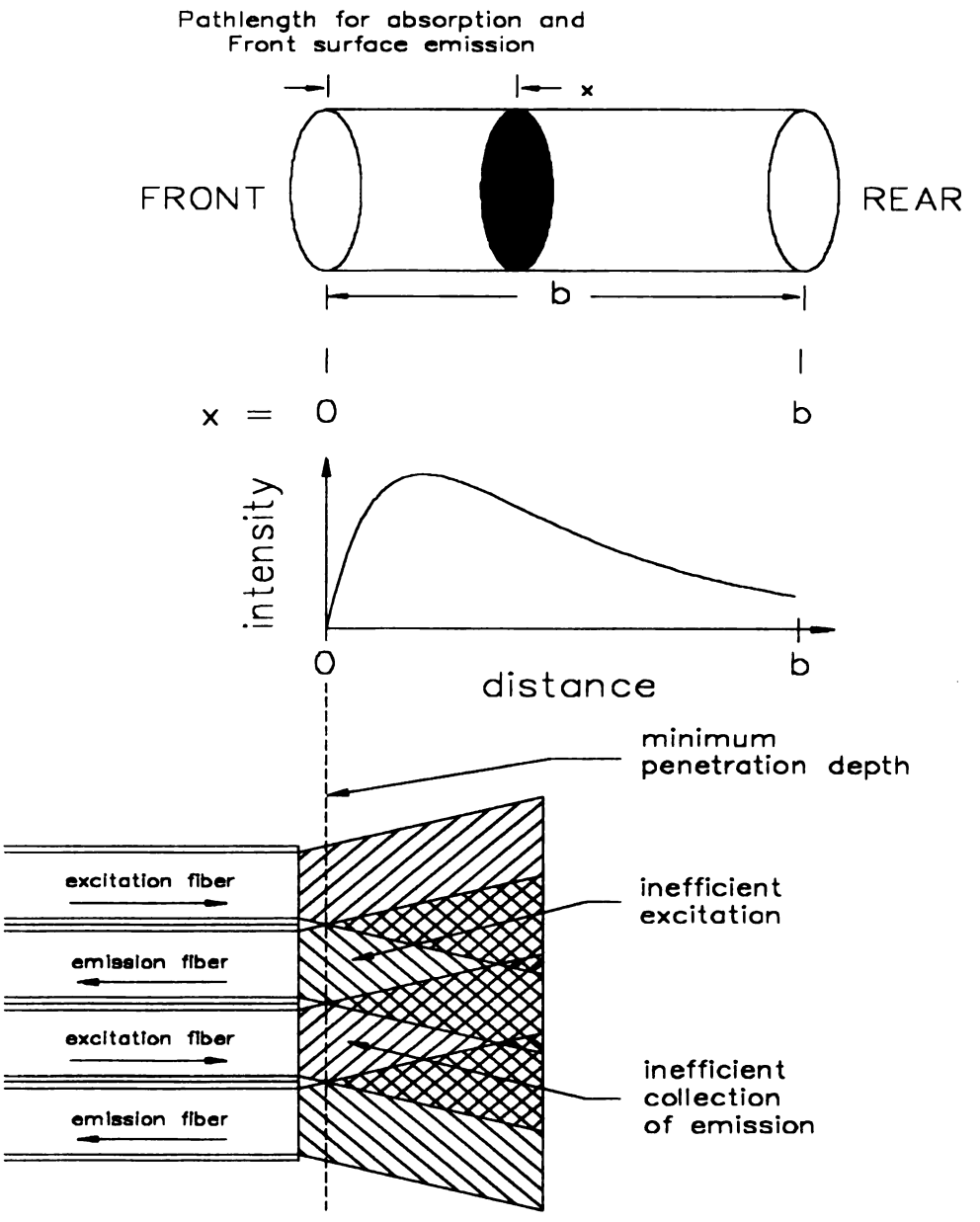

Figure 2-2

Excitation Emission Overlap as Related to the Minimum Penetration Depth

The top two figures are a representation of fluorescent intensity observed versus distance from an infinitely thin slice for a front surface bifurcated fiber optic fluorometer. This also demonstrates the spacial relationship between the minimum penetration depth and the fibers transfer function. The bottom figure shows that near the front surface of the excitation fibers the emission capture is negligible. Likewise directly in front of the emission fibers, illumination is zero. This accounts for the lack of any observable fluorescence until appreciable excitation/emission overlap occurs. Fluorescence occurs but is not observed until the excitation and emission cones overlap at the minimum penetration depth.

rays are successfully refracted down the length of the fiber. For the case of an emitter directly on-axis with a fiber, calculating the total solid angle captured by the fiber as a percentage of the total solid angle irradiated is straightforward. This is shown in Figure 2-4 for an on-axis emitter. This figure is drawn with the relative size of the elements dimensionally correct. When the emitter is off axis with respect to the center of fiber, the solid angle captured takes on the shape of an ellipsoidal based cone (Figure 2-3), rather than a circular based cone (Figure 2-4).

Nevertheless, each sensor that is emitting is compared against all the fibers to ascertain how much, if any, of the total irradiance is captured by an emission fiber. For the case of a coaxial fiber and emitter, we would predict the greatest capture efficiency. From Figures 2-5, and 2-6 we can surmise that the total capture efficiency in the coaxial case remains constant. The intensity will remain constant until the emitter is a sufficient distance from the fiber that the capture percentage is no longer numerical aperture limited. After this distance, the intensity is expected to decrease inversely with respect to distance. By calculating the area of the solid angle of capture as a percentage of the total solid angle of irradiance for all emitters against all fibers, we can calculate the percentage of emission captured as a function of distance into the cell (Figures 2-4, 2-3, and 2-5).

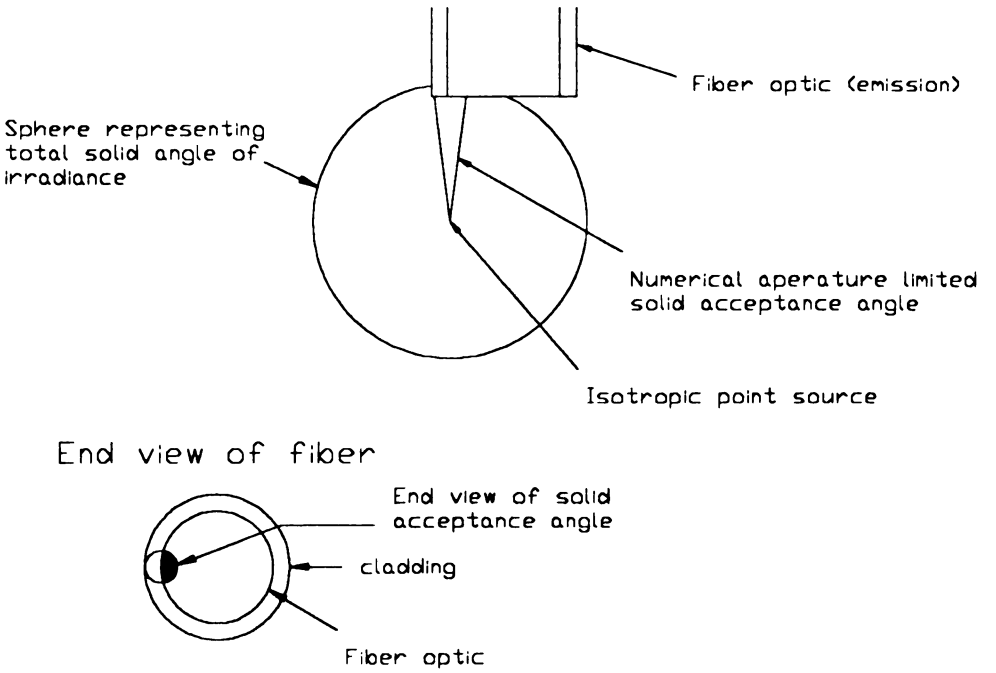

Figure 2-3

Fiber Emitter Overlap, Off-Axial Alignment

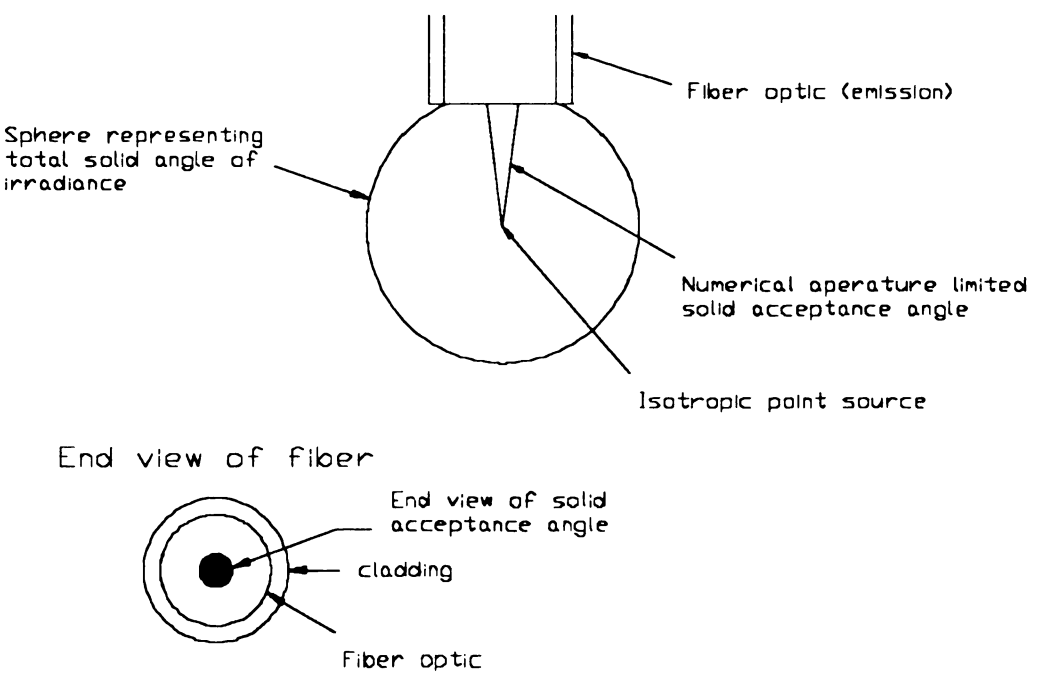

Figure 2-4

Fiber Emitter Overlap, Co-Axial Alignment

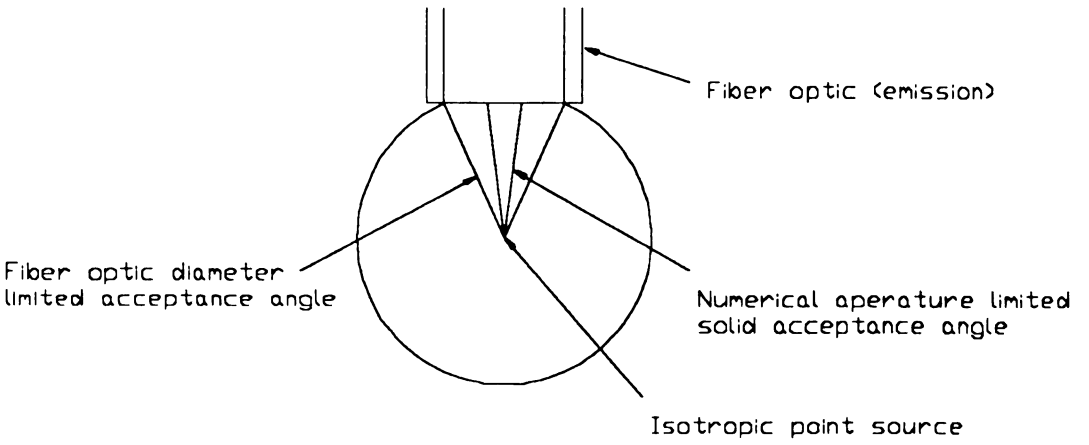

Figure 2-5

Capture Efficiency
Numerical Aperture Limited vs Fiber Geometry Limited

Shown graphically are the acceptance cones (capture efficiency) for the numerical aperture limited case and the fiber geometry limited case. The picture is not to scale but is dimensionally proportionate assuming an effective numerical aperture limited case. As the point source becomes more distant, the divergence angle which is fixed by the numerical aperture, overfills the fiber face and the capture efficiency drops.

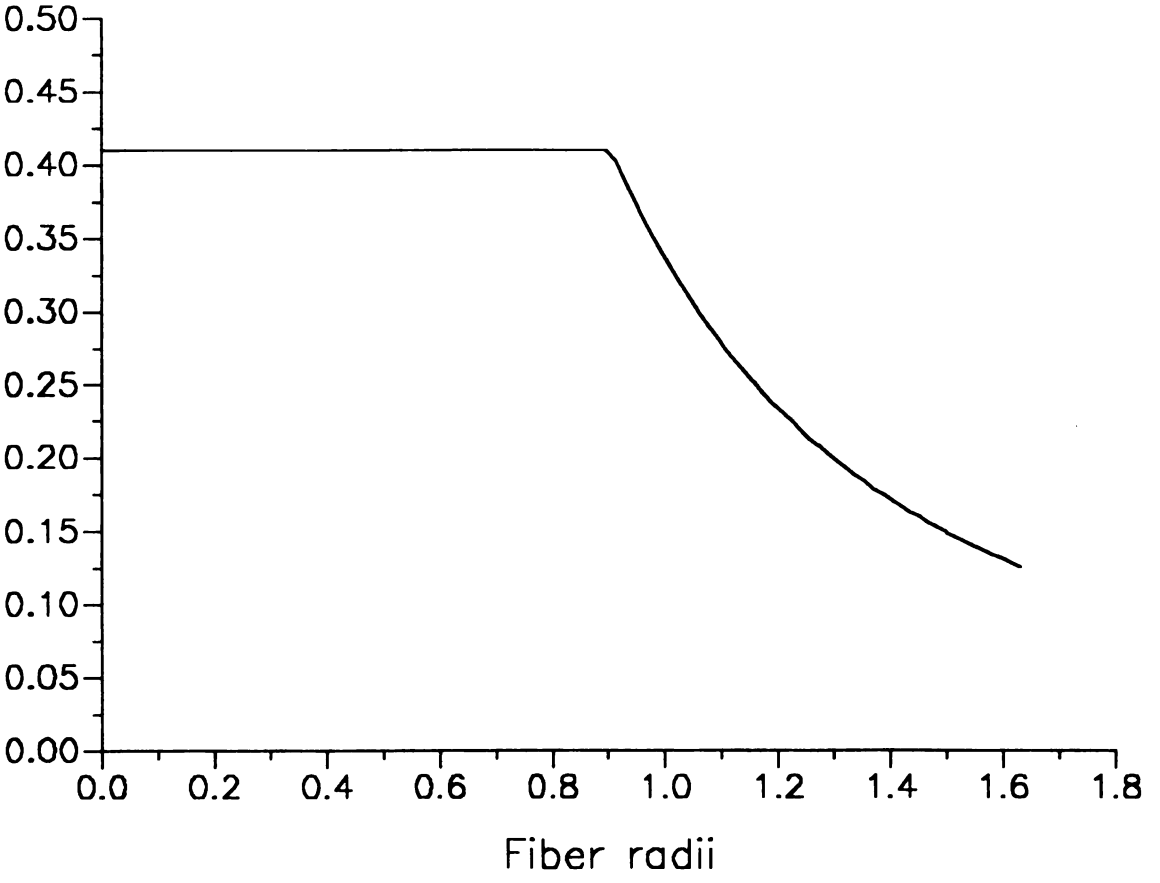

Figure 2-6

Capture Efficiency vs. Fiber Radii

co-axial fiber alignment

Show above is the capture efficiency (in percent), vs. distance from the front of the cell (expressed in units of fiber radii). As predicted by a monochromator numerical aperture limited capture efficiency, the percentage transmitted down the fiber remains constant until the fiber is overfilled. The capture efficiency then decays inversely with distance.

RESULTS

As can be seen from Figure 2-2, the model predicts the transfer function to be zero close to the front of the cell. In reality, this is has not been observed from the solid phosphor scattering experiments. Scattering experiments with an untreated brass rod have been able to measure appreciable signal levels at nearly zero distance. Likewise, when the fiber was immersed in a concentrated potassium permanganate solution to absorb the excitation beam, significant signal was found along the excitation channel. This is due partially to crosstalk among fibers in the common arm of the bifurcated fiber optic. Additionally, the assumption that the optical power in the cladding is zero is not true. If the electric field model is used to describe the propagation of light, instead of the ray model, it is found that an 'evanescent field' [8] in the cladding produces a measurable signal.

When the resulting curve was regressed about the transfer function equation $T(x) = \left(e^{-Hx} - e^{-Kx}\right)$, the values of H and K were found to be 0.798 and 1.087 respectively. As can be seen in Table 2-1, when using these values to calculate correction factors for a range of simulated absorbances, wide disagreement was found with the correction factors calculated by other methods.

Table 2-1

Correction factors (CF) obtained via modeling and Quinine Sulfate fluorescence probe		
Absorbance	Correction Factor via Quinine Sulfate probe	Correction Factor via Modeling
1	2.54	3.48
2	4.82	8.51
3	7.80	16.79

DISCUSSION

It is obvious these values will not produce valid correction factors for absorption-corrected fluorescence studies. We believe our model to be valid because of the excellent agreement of this modeling study with the work of other researchers [18] (see earlier Figure 1-13). Our belief in the validity of the model leads to several conclusions. The most obvious conclusion is that additional processes occur within the real cell that are not accounted for in the model. These effects include, reflections from the cell walls, reflections from the fiber on the far end of the cell, solvent scattering, fiber cross talk, stray light, and absorption and scattering by the analyte. By adding these factors to the model and hand "tuning" the parameters, agreement could be obtained between the model and experimental data consistent within experimental error. However, the unreasonable range of adjustment required to the additional parameters to "fit" the model to the data did not fall within norms expected of such values.

The only additional observation concerning a reason for the poor fit is to examine in detail the theoretical calculation of the transfer function by Doherty [16]. The derivation is similar to that of Plaza [6], with basically two differences. The first involves the use of a Cartesian instead of a polar coordinate system, while the second is a more generous assumption of the capture efficiency of the observation fiber. Doherty assumes the solid angle of collected light is approximated by, $r^2/\pi\left(R^2+z^2\right)$, where $\left(R^2+z^2\right)^{1/2}$ is the distance from the center of the overlap area to the center of the emission fiber. By noticing Figure 2-5, which depicts the fiber geometry limited capture efficiency drawn to actual scale using a CAD package, the capture efficiency for the case of an emitter coaxial with the fiber would remain constant with distance until the fiber face was overfilled. At greater depths into the cell, the observed percentage of the solid angle would drop as $1/x^2$, this is shown in Figure 2-6. When the two expressions are compared on the

same scale along with the transfer curve (Figure 2-7), it can be seen that the fiber diameter limited case drastically overestimates the capture percentage.

This itself is uninteresting until we re-run the modeling program using the fiber diameter limiting expression, $r^2/\pi\left(R^2+z^2\right)$, to express the fibers capture efficiency. The results of this experiment are shown in Figure 2-8. The coefficient of determination for this fit is 0.998. This is better than any of the other data sets, either theoretical or experimental. The fiber diameter limiting capture percentage overestimates the capture percentage more severely during the exponentially rising portion of the transfer curve. The rising portion of the curve primarily determines the parameter H in the transfer function equation. When calculating the correction factor, the smaller value H, weights much more heavily in the resulting correction factor due to negative exponential term containing both H and K. By having the capture percentage artificially skewed during the rising portion of the transfer curve, the best fits to the predicted form of the transfer function were obtained. The skewed model produces values for H and K which when substituted into equation 1-1 produce excellent corrections for all experimental cases. These results are well within experimental error.

From the known behavior of a fiber optic's numerical aperture, we can assume that 20 percent capture near the fiber face is unrealistic, in reality the figure is closer to 0.041 percent. However, the physical effect of artificially skewing the capture percentage

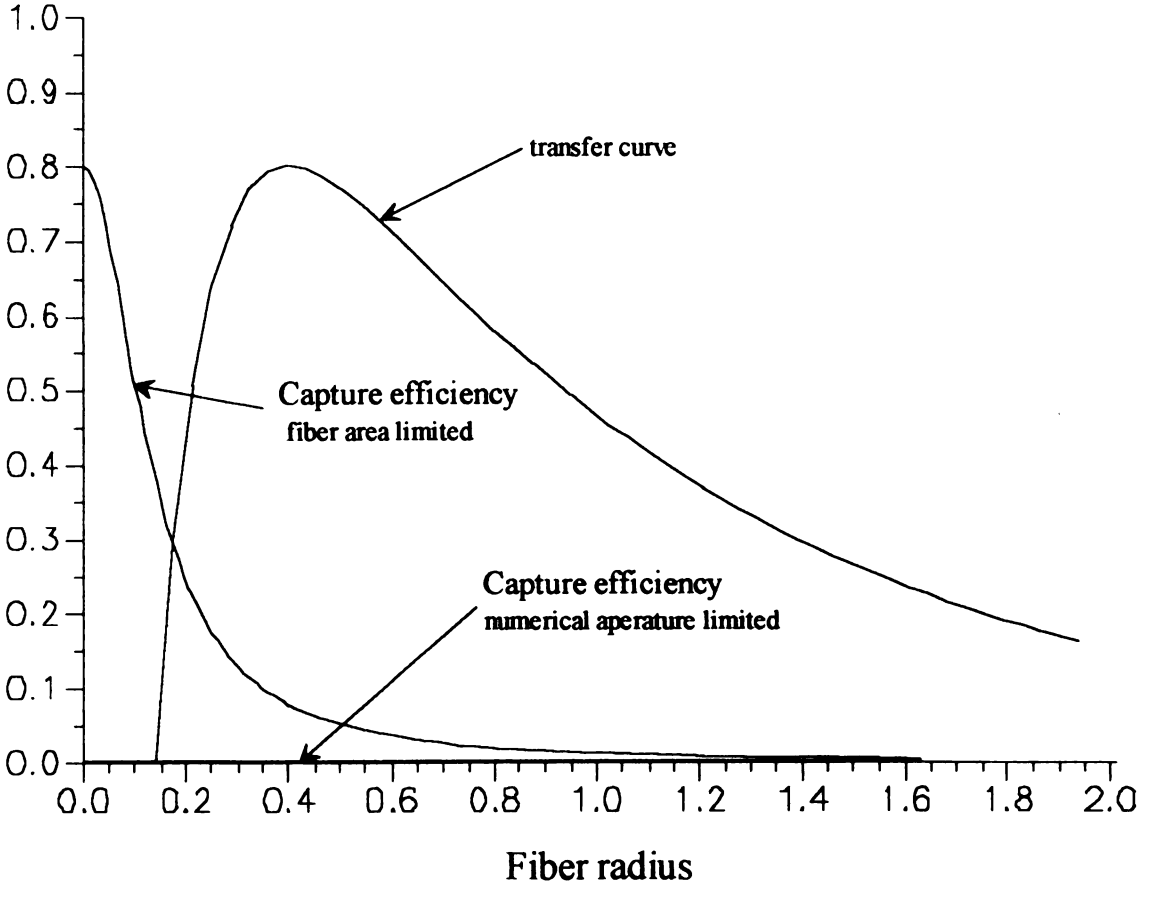

Figure 2-7

Calculated Capture Percentages for Several Models vs the Fibers Transfer Function

Shown is the calculated transfer function plotted against the capture efficiency calculated by two different methods. The fiber area limited method overestimates the capture efficiency 100 fold over the numerical aperture limited method in the critical exponential rising portion of the curve. The rate of the exponential rise is what determines the parameter H. Being the smaller of the two parameters, it affects the correction factor to a greater extent.

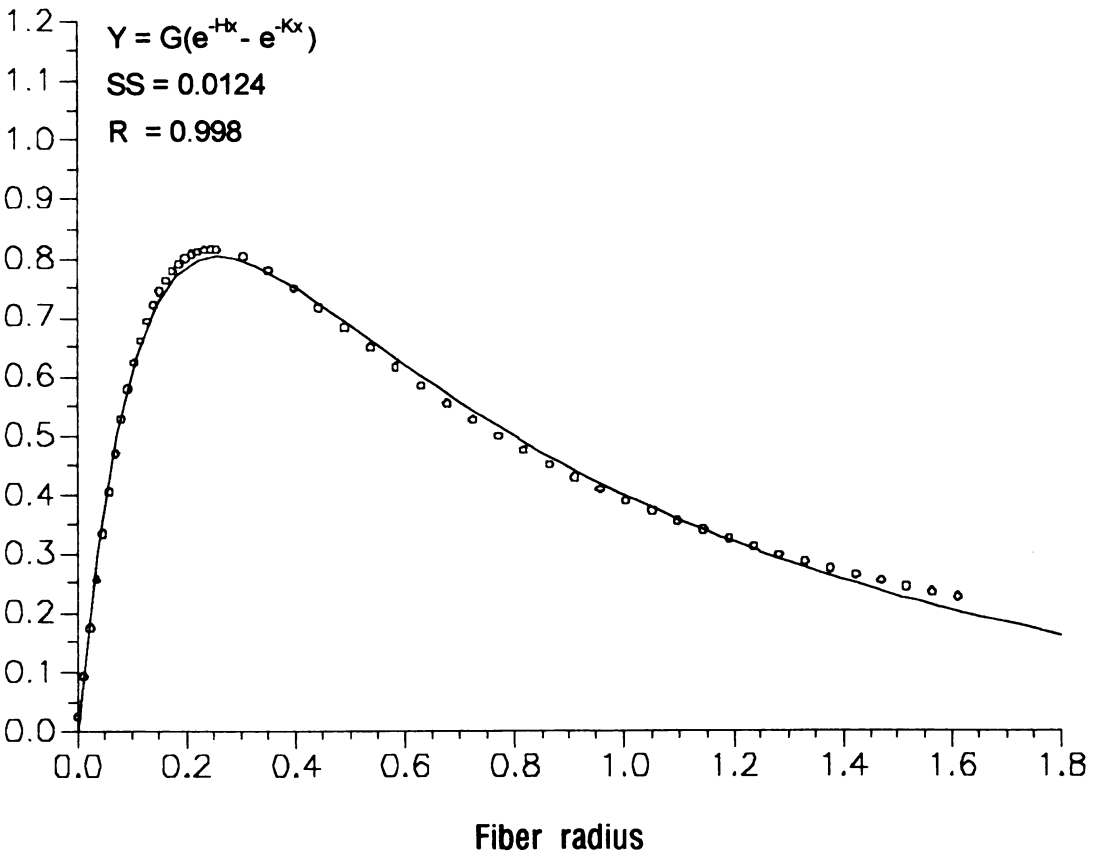

Figure 2-8

Modeling Data Curve for the Fiber Geometry Limited Capture Percentage

The modeling program, assuming fiber optic diameter limited capture efficiency, produces an excellent fit to the equation describing the transfer function $T(x)=G(e^{-Hx} - e^{-Kx})$. The fit coefficients for the theoretical fit are better than any of the fits for the experimental data. The offset due to the minimum penetration depth (≈0.18 fiber radius) has been subtracted.

produces analytically useful correction factors. Obviously, the known numerical aperture of the system is not off by a factor of 40, for such a case to be true, the monochromators f number would have to be at least f/0.5. Either serious flaws exist with the model or other physical effects must account for the difference. Because the model relies solely on simple geometry and ray tracing we can assume it accurately predicts ideal fiber behavior. Additionally the model is corroborated by a similar study done using polar coordinates [6] as shown in Figure 2-9.

We can attribute the differences then to non-ideality in the physical fibers, flow cell, and the analytes. Photomicrographs of fiber optics [19] show anything but the smooth perpendicular faces assumed in the model. The particular fiber bundle used in this investigation is a veteran of 8 years usage in our laboratory. Many fibers have been chipped, scarred, and etched during its lifetime. As mentioned earlier, crosstalk within this particular bifurcated fiber bundle is rather severe. The fibers had been etched in an earlier investigation which employed aqueous NaOH. In addition, the epoxy filler used in the construction of the bifurcated fiber bundle has an affinity for quinine sulfate (QS). Previous investigations with this analyte have permanently contaminated the fiber optic bundle to the point that virtually any pure solvent analyzed by fluorometry with this bundle appears to have a concentration of 20 ppm QS.

At this point, modeling alone cannot be relied upon to yield accurate correction factors. However, the theory and assumptions of Ratzlaff [15] appear to be valid. Experimentally derived correction factors produce analytically correct results. This extends the utility of fluorometry when analyzing optically thick solutions. Analytical corrections have been made to solutions with aggregate absorbances of over 5 AU with good results. Clearly synchronous fluorescence, which is expected to operate in complex matrices containing multiple chromophores can benefit from the application of this technique.

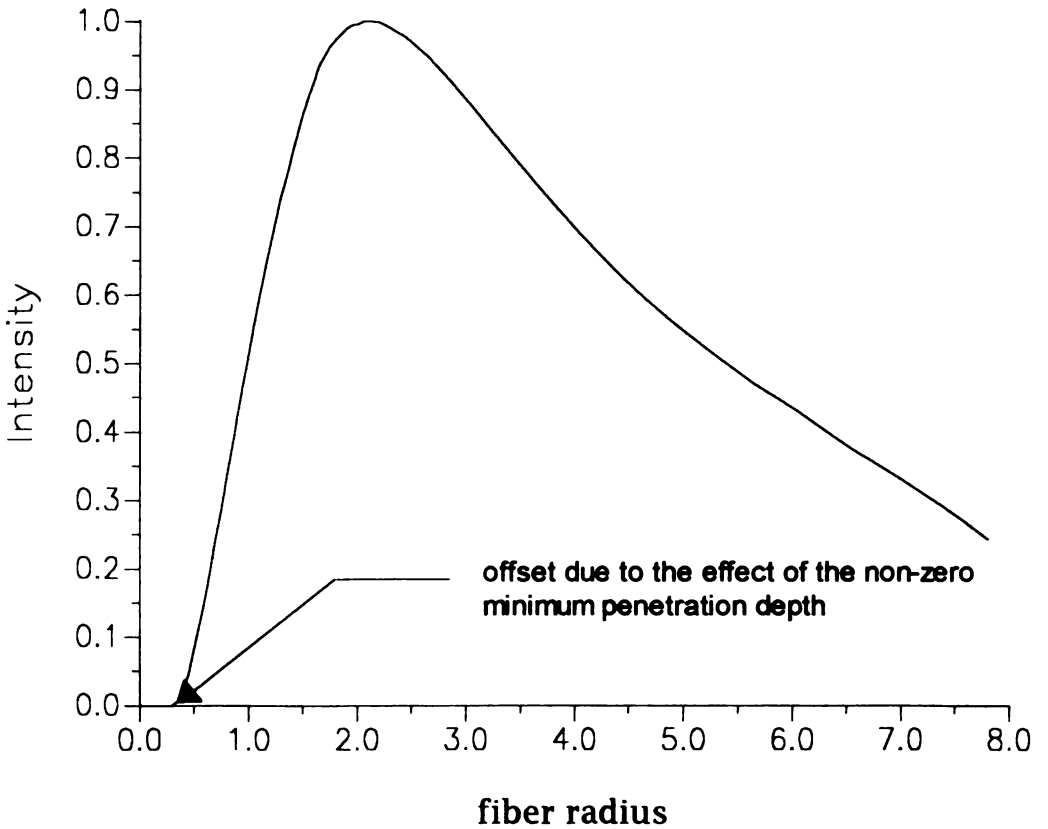

Figure 2-9

Transfer Function Curves

Polar vs Cartesian Coordinates

Shown is the calculated transfer function curve obtained by modeling. It superimposes almost perfectly over the curve obtained by calculating the transfer curve in polar coordinates using the method of Plaza et.al. [6]. Modeling was performed for the case of a single pair of excitation/emission fibers. The modeled curve was obtained by calculating with 10,240 simulated sensor/emitter objects.

FUTURE WORK

It would be preferable not to have to prepare multiple solutions of several fluorophores not of analytical interest in order to calibrate a bifurcated fiber optic based fluorometer. Punching the physical constants and dimensions of the components into a computer and having a suitable correction factor evaluated would be preferable. Future work could involve a basic investigation into the interaction between excitation/emission fibers in a bifurcated fiber optic. The most reasonable course is to construct a single fiber optic based fluorometer for which the model can be solved exactly (Figure 2-10).

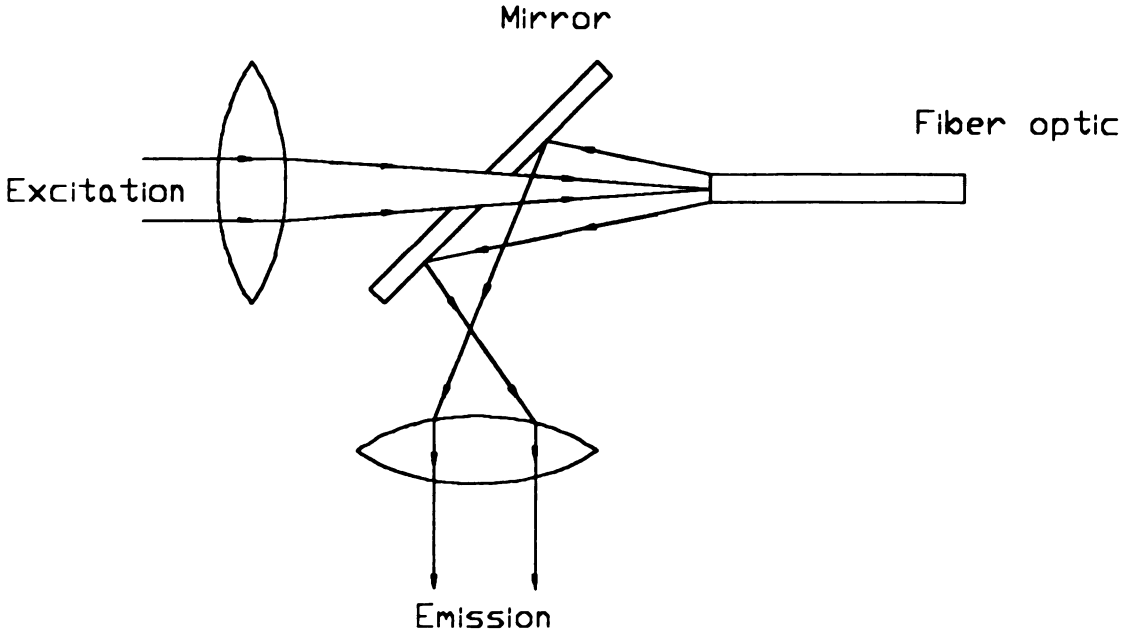

Figure 2-10

Proposed Single Fiber Based Fluorometer for Transfer Function Studies

The simplest case would be for a bifurcated fiber optic consisting of only two fibers. The overlap integral for the excitation and emission fibers of a two fiber front surface instrument can be evaluated exactly in equation 4. The empirical approximation of the degree of overlap, equation 6, would not be necessary. The experimental behavior for such an instrument against a soluble fluorophore and a solid phosphor could then be compared to theoretical behavior in the hopes of better understanding the physical process governing excitation/emission coupling dynamics [10, 11].

Other techniques employed in remote sensing technology can further reduce the complexity of the model by dealing with only one fiber. By having the same fiber carry both excitation and emission rays, experimental behavior can be compared with respect to an exact model.

REFERENCES:

1. V. Vali, R.W. Shorthill, *Appl. Opt.*, **15**, 1099 (1976).

2. W.R. Seitz, *Anal. Chem.*, **56**, 16A (1984).

3. L. Chabay, *Anal. Chem.*, **54**, 1071A (1982).

4. S.M. Angel, *Spectroscopy*, **2**, 38 (1987).

5. W.R. Seitz, CRC Crit. Rev. *Anal. Chem.*, **19**, 135 (1989).

6. E. R. Ratzlaff, Ph.D. Dissertation, Michigan State University, East Lansing, MI, 1982.

7. P. Plaza, N.Q. Dao, M. Jouan, H. Feurier, H. Saisse, *Appl. Opt.*, **25,** 3448 (1987).

8. P. Schwab, R.L. McCreery, *Anal. Chem.*, **56**, 2199 (1984)

9. T. Deaton, *Instrumentation and Methodology for Remote Fiber Fluorimetry*, Ph.D. dissertation, University of California at Davis (1984).

10. Z.Y. Zhu, M.C. Yappert, *Appl. Opt.*, **46**, 912 (1992).

11. Z.Y. Zhu, M.C. Yappert, *Appl. Opt.*, **46**, 919 (1992).

12. D.N. Modlin, F.P.Milanovich, in *Fiber Optic Chemical Sensors and Biosensors*, O.S. Wolfbeis (ed.), pp 237-303. CRC Press, Boca Raton, 1991.

13. C. Komives, J.S. Schultz, *Talanta*, **39(4)**, 429 (1992).

14. J.S. Schultz, in *Biosensors: Fundamentals and Applications*, A.P.F. Turner, I. Karube, G.S. Wilson (eds.) pp 638-654. Oxford University Press, Oxford, 1987.

15. E.H. Ratzlaff, R.G. Harfmann, S.R. Crouch, *Anal. Chem.*, **56**, 342 (1984).

16. T.P. Doherty, Ph.D. Dissertation, Michigan State University, East Lansing, MI, 1988.

17. H.W. Latz, A.H. Ullman, J.D. Winefordner, *Anal. Chem.*, **51(1)**, 191 (1980).

18. R.A. Leese, E.L. Wehry, *Anal. Chem.*, **50(8)**, 1193 (1978).

19. Ping Yuan, D. Walt, *Anal. Chem.*, **58**, 2391 (1987).

CHAPTER 3

DESIGN AND CHARACTERIZATION OF A RESEARCH GRADE INTENSIFIED DIODE ARRAY SPECTROMETER

Introduction

The diode array was the instrumentation focus of a major grant for simultaneous multiwavelength studies of various of kinetic systems. These studies involved stopped flow, continuous flow, flow injection, and HPLC. This required special attention be given towards optimizing the system for acquisition speed, a wide and variable wavelength range, low light sensitivity, and easy interfacing when being re-deployed among different experimental stations. The variety of applications, and the non-standard conditions encountered in an R&D environment typical of a university setting were best met by maximizing instrumental versatility with flexible design considerations.

In this chapter the interrelations between the instrument's specifications and the design goals are examined. A block diagram and overview of the instrument are presented, followed by a detailed discussion of individual components and their relationship to the systems performance. The following sections deal with the computer interface, as well as the diode array and it's associated optics. The discussion concludes by detailing the high speed data acquisition interface board. The next chapter will discuss the control software that binds the system together.

INSTRUMENT OVERVIEW

The system consists of three basic components. The intensified diode array and it's wavelength dispersive grating, the microcomputer interface card, and the control software. A block diagram of the instrument (Figure 3-29), and a brief summary of the various modules that make up the instrument and their interaction are as follows.

The diode array spectrometer is different from a conventional spectrometer in that multiwavelength measurements are made simultaneously and digitized and stored

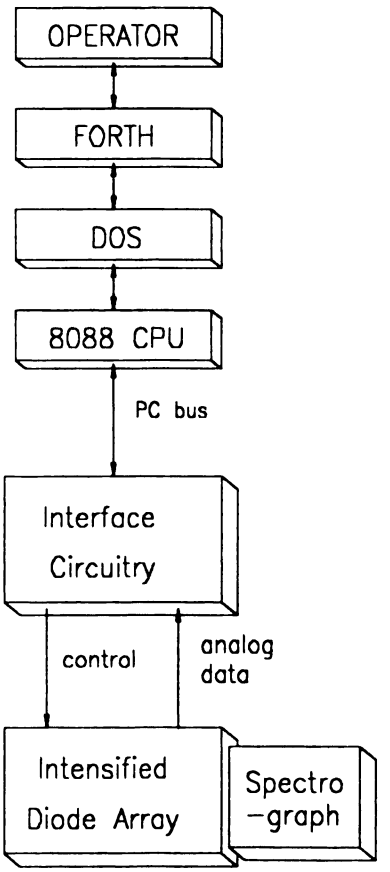

Figure 3-1

Block Diagram of Instrument

sequentially. The array is a TN-6123 (from Tracor Northern, Middleton, WI.) composed of 512 separate diodes, of which 510 are active. The array uses a circular non-gated microchannel plate as a 2-D image intensifier. The microchannel plate provides photon gains of roughly 3000 fold [1 , 2]. A concave holographically ruled grating with a fixed focal length disperses a 400 nm slice of the electromagnetic spectrum across the linear diode array. The grating is mounted on a rotating stage with micrometer control. This allows any 400 nm range to be dispersed across the array. The microchannel plates S-20 photocathode limits measurements to the 200-1200 nm regions of the UV-VIS spectrum [1]. Control signals to generate data are sent to the diode array through a programmable interface board mounted inside an IBM compatible Personal Computer (PC). An interface board mounted inside the PC sends timing and digital control signals to the array. Additionally the board provides for high speed data acquisition and storage of analog data from the diode array into the memory and disk drives of the PC for later display and processing. A PC version of the FORTH programming language running under Disk Operating System (DOS) provides instrument control and an interface language suitable for a novice operator.

INSTRUMENTAL COMPONENTS

Introduction

The remainder of this chapter deals in depth with the actual chips, diode array components, lenses, gratings, mirrors, and software that comprises the instrument. Each component is discussed in its entirety with special emphasis on its specifications and how they relate to the overall instrument's performance. The first sections deal with the hardware components. The control and processing software are discussed last.

Overview of the Diode Array Detector Head Assembly

The function of the TN-6123 detector head is to convert spectral information into a series of analog pulses. The ultimate source of these pulses is a linear, self-scanned, silicon photodiode array consisting of 512 elements on 25 micron centers. This corresponds to 40 diodes/mm, thus giving a wavelength coverage of 400 nm with the grating used in our spectrograph. Each element is 2.5 mm high, giving each diode a 100:1 aspect ratio. These dimensions are desirable as they match the aspect ratio of the slits of our spectrograph. During normal operation the spectrum to be examined is projected across the face of the photodiode array by the spectrographs grating. The individual diodes of the array are interrogated sequentially, producing a train of pulses. The height of each pulse is proportional to the cumulative radiation striking a particular array element prior to its last readout. Spectrum wavelength information is reconstructed from the position of the pulses in the readout sequence. The TN-6123 uses an image intensifier for low light work. The spectral range of the TN-6123 is determined by the S-20 extended red multi-alkali photocathode that comprises the photoactive portion of the microchannel intensifier. Incorporated into the detector head is a Peltier cooling element that reduces dark current by cooling the array. Dark current is reduced by 50% for each 7^{o} C drop in the array's

temperature [3]. Provisions exist for purging the array head with dry N_2 to prevent water condensation when the array is cooled below the dew point.

Equivalent Circuit of a Diode Array

Figure 3-2 is an electronic equivalent circuit of a Linear Diode Array (LDA). The capacitors represent the inherent capacitance seen across the P/N junction of a reverse biased photodiode. Incident radiation forward biases the photodiode. This induces a photocurrent that bleeds charge from the individual diode in direct proportion to the incident radiant power. Elements are interrogated by sequentially closing MOSFET switches and dumping out any residual charge onto a common video output line. This is performed by loading a "1" into a shift register and clocking it through the length of the array. The residual charge is inversely proportional to the radiant power striking the element prior to the last readout.

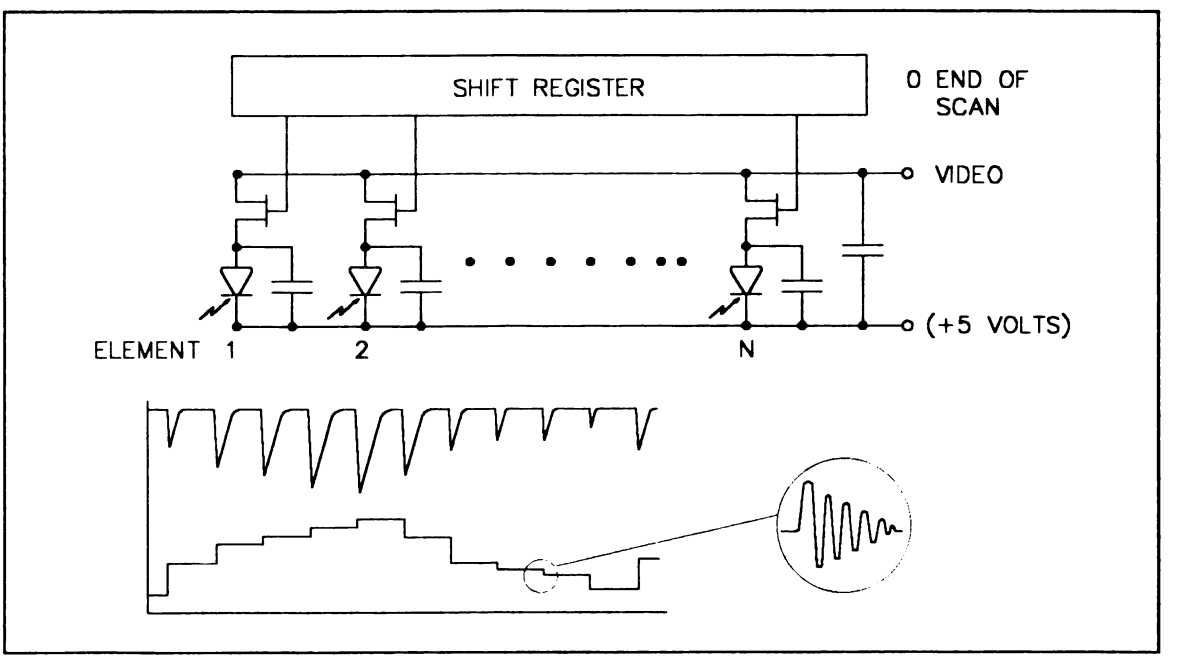

Figure 3-2

Diode Array Equivalent Circuit

Signal Requirements of the Diode Array Detector

Handshaking between the detector head and the control system is performed primary with two signals. The signals are Scan Time Base (STB) and Start (START) (Figure 3-4). Prior to the start of the scan all the diodes have been connected to the +5 volt bus. This charges all the diodes to the same positive 5 volt potential. The START pulse loads a binary "1" into the first bit of the shift register. This connects the first array element to the common video output line. A combination of photon-induced reverse current and thermal dark current leakage cause charge to bleed from the capacitance of the P-N junction of the

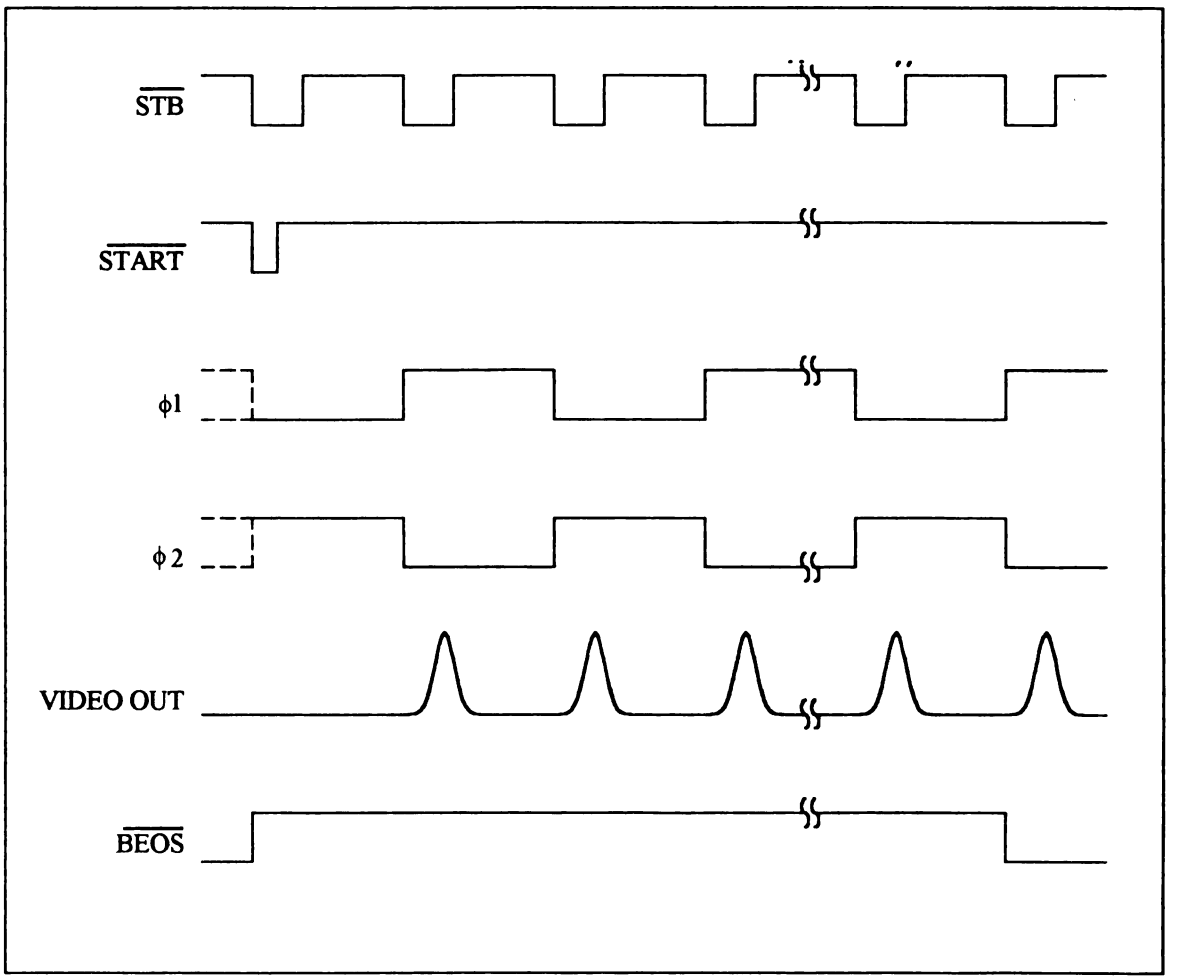

Figure 3-3

Timing Diagram for the 2-Phase Diode Array Driver

photodiode. The residual charge, which is inversely proportional to the incident intensity striking the element prior to the last readout, is dumped out as an analog pulse on the common video output line. An inverting amplifier in the diode array head assembly turns this into a positive analog pulse from 0-4 volts and drives it into a 50 Ω load. Subsequent Scan Time Base (STB) pulses push the binary "1" down the shift register. This successively closes the MOSFET switches and sequentially interrogates the entire diode array. Before the "1" falls off the end, it closes a MOSFET switch that recharges all the diodes to a +5 volt potential in preparation for the next scan. Finally, the "1" toggles a flip-flop to a high state, the buffered output of which the diode array returns as the handshaking signal Buffered End Of Scan (BEOS). The START pulse from the PC clears the same flip-flop).

In reality, the process is not quite so straightforward. As Figure 3-2 shows, closing of the MOSFET switch produced substantial ringing on the VIDEO OUT line. The two end diodes in the array are intentionally "dead". They consist only of MOSFET switches without a companion active diode. These dummy diodes are read out each time an active diode is scanned. The output of the blind diodes is used as a reference on the VIDEO OUT amplifier to subtract the ringing effect induced by the closing of the MOSFET switch. The array is driven by a multi-phase clock such that all the odd and even number diodes have separate clock drives, level shifters, shift registers, video lines, and amplifiers. Proper phasing the clock drives to the two shift registers allows all of the diodes to be sampled in the proper sequence. Figure 3-4 shows the pinout for the tandem drive circuits of the ODD/EVEN shift registers of the integrated circuit which is the actual diode array [4]. The two video lines are connected together to provide a continuous train of output pulses. Multiphase clock drive circuits with tandem readout amplifiers can produce a synthetic "noise" if any of the charge pre-amplifiers is unbalanced. The effect is that charge from every other diode is amplified by a different gain factor than its neighbor. This produces a pseudo noise in the

readout proportional to the STB clock readout frequency. Figure 3-4 gives the pinout of the EG&G Reticon (Princeton, NJ.) Linear Diode Array (LDA) chip.

Figure 3-3 shows the timing relationship between the user supplied handshaking signals and the appearance of video pulses on the VIDEO OUT line. The $\overline{\text{START}}$ pulse clears a flip-flop that drops $\overline{\text{BEOS}}$ low. The start pulse also loads a binary "1" into the first element of the shift register. The user supplied time base $\overline{\text{STB}}$ drives the binary "1" along the shift register successively dumping the residual charge from each element on the VIDEO OUT line. The clock is made multiphasic by dividing the $\overline{\text{STB}}$ signal by 2 with a J-K flip-flop. This provides identical timing to the ODD and EVEN shift registers shifted 90^{o} out of phase. Notice that there is a delay between the falling edge of $\overline{\text{STB}}$ and the peak maximum of the analog VIDEO OUT peak (Figure 3-3).

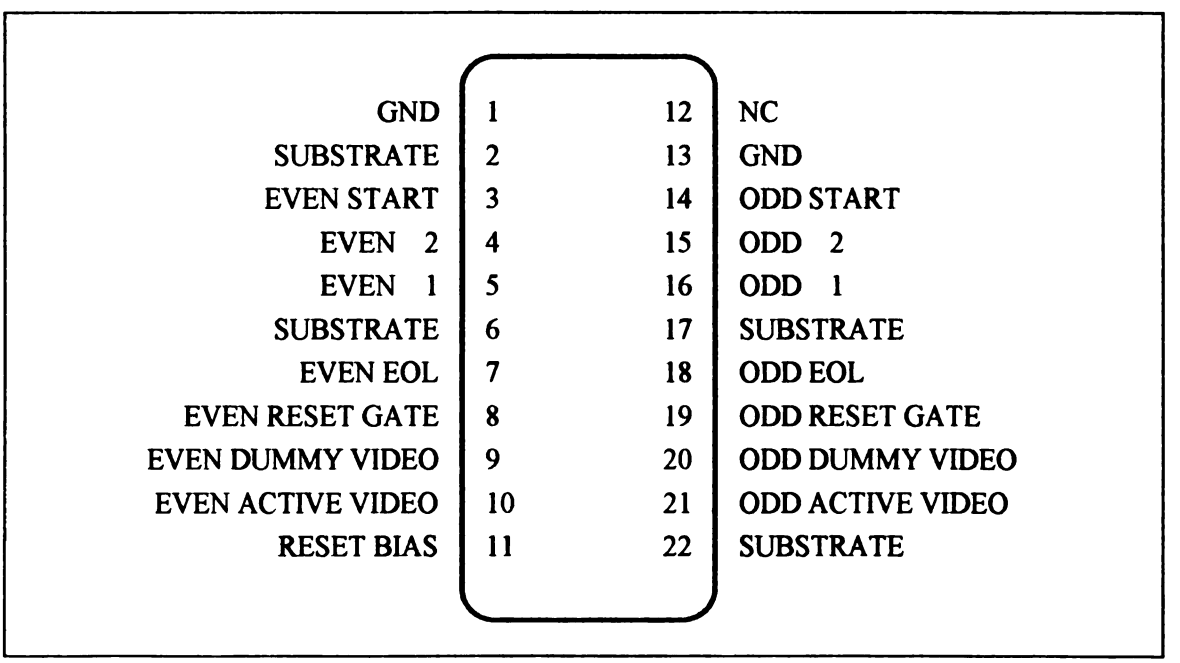

Figure 3-4

Pin Configuration for the Diode Array Integrated Circuit

The Microchannel Plate Image Intensifier

The major difference between an earlier diode array system developed in our lab [5] and the current system is the microchannel plate proximity focus image intensifier. A microchannel plate (MCP) is a secondary electron multiplier consisting of an array of glass capillaries (channels) of like internal diameters ranging from 10 μm to 20 μm fused into a thin disk approximately 1 mm thick (Figure 3-5). The inside of each channel is coated with a secondary electron emissive material which is doped to give the proper resistance across the microtubule. Both ends of the channel are covered with a thin metal film that

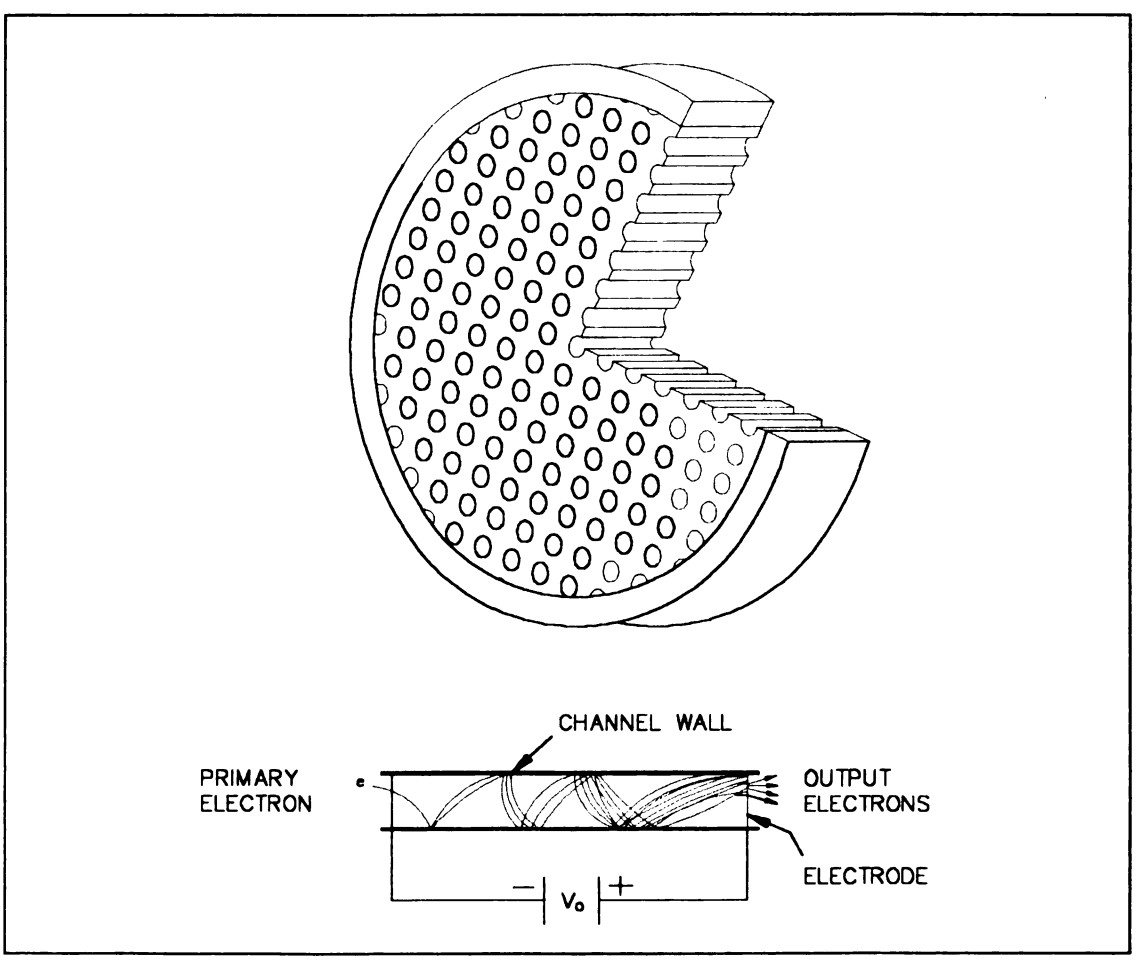

Figure 3-5

Microchannel Plate Image Intensifier

form the electrodes. Each channel thus acts as an independent secondary electron multiplier.

The application of a voltage V_D between the sides of an MCP, as shown in Figure 3-5, generates an electronic field along the channel axis. When a primary electron, generated by an S-20 extended red sensitivity photocathode, strikes the entrance wall of the channel, secondary electrons are produced. These secondary electrons are accelerated by the electric field, and travel along parabolic trajectories determined by the potential and their initial velocities. This process is repeated along the length of the channel with an exponential increase in current near the phosphor. Subsequent cascading produces electron gains on the order of 10^4 [1, 2]. In the instance of the TN-6123 detector head, a thin phosphor coating converts the amplified output current into 540 nm visible radiation.

Features of the MCP image intensifier such as high gain, 2-dimensional image intensification, fast time response, immunity to magnetic fields, sensitivity to charged particles, UV, and X-rays, low power consumption, small size, and rugged nature make MCP useful in a variety of application. Image intensification across a linear diode array is a spin-off of early military applications involving night vision technology.

The gain of a microchannel plate is a function of the length-to-diameter ratio of the channel $(\alpha = L/d)$, and the electric field strength defined as a voltage drop per given length $\left(V_D = V_D/\alpha\right)$ and is represented as follows:

$$\text{Gain} = \exp(G * \alpha)$$

where G is a gain factor related to the secondary electron emissivity characteristics of the channel wall. Above gains of 10^4, electron depletion within the channel wall and ion feedback noise occur. Non linear gain effects can occur when a weak signal is spatially near a much stronger signal.

Dark current signals in MCP's originate through physical phenomena such as thermionic emission, electric field emission, ionization of residual gases, discharge in a high electric field, and photoelectron emission from photons produced in an electric field. Individual contributions from each effect are difficult to separate and their contributions have yet to be quantitated. When a MCP is cooled, the dark current decreases proportionally with temperature [6].

Gain saturation is related to the disturbances in the potential distribution near the output end due to an increase in the strip current that supplies the current released from the channel wall [2]. Gain saturation occurs when the ratio of the output current (I_0) to the strip current (I_S) reaches a value of about 10%. The spatial proximity of strong and weak signals will produce non-linear gains for the lesser signal due to a significant charge depletion in the resistive electrode surface near the stronger signal. Charge depletion in an area of the MCP will cause a pincushion effect reducing the effective gain of nearby channels. This is called the pin cushion effect, named because of the shape of the potential density drop in the proximity of the saturated channels.

The most commonly used MCP's have internal channel diameters of 12, 15, and 20 μm. Typical values of the length-to-diameter ratio of a channel $\alpha = L/d$, which is a figure of merit for gain, have values around 45. MCP's are manufactured by slicing a fused bundle of many small capillaries into thin disks. A slice angle of from 3-7^{o} is selected to prevent primary electrons from passing through the channel without touching a wall. In tandem MCP applications this is useful to prevent ion feedback. On both input and output surfaces of the capillary disk Fe-Cr is evaporated; its thickness is adjusted to give a surface resistance of 50 to 100 Ω across the diameter of the disk. Roughly 300-350 channels service an individual element of the diode array. Photon gains are typically 3000-4000 times greater for a MCP equipped array over an unintensified array [1].

Other Specifications of the TN-6123 Array Detector

The TN-6123 detector head consists of an EG&G Reticon 512-S spectroscopic grade linear diode array with an 18 mm diameter proximity focused intensifier. The 512 elements are 10 μm wide, 1 mm high, on 25 μm centers. The MCP's photocathode is an S-20 extended red (S-25) with a fused quartz fiber optic window. The peak sensitivity of the S-25 occurs between 450-550 nm with a peak quantum efficiency of approximately 12% [1]. Gain control is accomplished through a 50 kiloohm potentiometer with a precision turn counting dial. The potentiometer provides for a 1:100 nominal gain range for an internal relative gain of 6000 when compared to an equivalent unintensified array. The response time is limited by the phosphor persistence. This persistence decays from 90% to 10% in 1 ms (typical), 2 ms maximum [1]. When uniformly illuminated, the detector will have a spatial gain variation of less than 62% [1]. The gain lifetime is roughly 1000 hours. After 1000 hours, the gain degrades to 50% of its initial value [1]. The intensifier/array assembly aggregate saturation exposure is 12 pwatt sec/cm^2 [1]. The sensitivity of the detector head is such that 6 counts per photoelectron are possible when VIDEO OUT is digitized with a 12 bit analog-to-digital converter (ADC) [1].

Incorporated into the detector head is a Peltier cooler, which serves as the mounting block of the LDA chip. The integral MCP is cooled by induction. Water inlet/outlet connectors are provided to pass cooling water through the Peltier heat pump. There are purge tubes present for dry nitrogen to keep moisture from forming in the detector head and on the array when operated below the ambient dew point. A set screw adjustment is provided to set the equilibrium temperature of the Peltier cooler. The analog output from a resistance thermometer, integral with the Peltier cooler, allows an absolute temperature measurement of the array when used with the manufacturers supplied nomograph [1]. A set screw adjustment allows setting of the equilibrium temperature in the range from room temperature to -40°C (with an antifreeze type coolant). The detector head additional

returns a CooLeR stabilized not signal, which is a TTL level signal to indicate the array has reached the preset temperature.

The TN-6123 detector head contains the necessary circuitry to drive the EG&G Reticon 512 element array when provided the user signals $\overline{\text{START}}$ and $\overline{\text{STB}}$. A 25 pin DB-25 connector provides for the input of these as well as additional drive signals. These are summarized in Table 3-1.

Additionally the TN-6123 detector head has a DB-9, 9 pin connector that provide communication and drive signals for the MCP intensifier assembly. A description of the pins and their functions are shown in Table 3-2.

Table 3-1

Diode Array Control Signals and Descriptions		
Pin #	Signal	Description
2	BEOS	Buffered End-Of-Scan not. TTL Zero indicated End-Of-Scan
3	Vout	Video OUT, Video output from amplifier
4	COMM	Video COMM, analog ground
6	CLR "STAB"	CooLeR STABilized not. TTL output indicating the cooler has reached the preset temperature.
8	+12	+12 volt supply for detector-preamp and drive circuitry. Normally 120 mA load.
9	-12	-12 volt supply for detector-preamp. Normally 100 mA load.
10	I RTN	Current ReTurN. 2 Amp (2.5 Amp max) current supply for the Peltier cooler.
11	+I	+5 volt current supply or the Peltier cooler
12	START	START not. Negative true TTL input to initiate the start of the scan. Driver must sink 10 mA to GND.

Table 3-2

Intensifier Control Signal Descriptions		
Pin #	Signal	Description
2	GN1	Gain Control, 50 KΩ potentiometer (minimum resistance is maximum gain between GN1 and GN2. Caution !! Intensifier power is on.
3	GN2	
4	GN3	
5	+2.7 v	2.7 volt supply to intensifier. Nominal load is 30 mA.
7	GND	Intensifier's supply ground.
8	SHIELD	Cable shield, connected to ground.

FUNCTIONAL DESCRIPTION OF THE INSTRUMENTS

PC COMPATIBLE CONTROL MICROPROCESSOR SYSTEM

The PC consists of an IBM compatible or "clone", with an Intel 8088 microprocessor and an 8087 mathematical coprocessor. System memory consists of 640 Kbytes of dynamic random access memory. Two 360 Kbyte 5 1/4 inch floppy disk drives provide for limited data storage. A graphics card supports bit mapped monochrome graphics in 720 by 348 pixel mode. A serial port gives access to several VAX minicomputers via Kermit. Kermit is a software program from CUCC (Columbia University Computing Center) which combines a file transfer protocol with terminal emulation.

In addition, the PC motherboard architecture supports facilities for Direct Memory Access (DMA) memory transfers and hardware initiated software interrupts. To understand the system hardware and software integration, a complete description of both services is necessary.

System Direct Memory Access (DMA) Hardware Services Available on the PC Motherboard

A rapid scanning diode array systems demands that data be offloaded as quickly as possible. To achieve this goal, the interface board uses the INTEL 8237A-5 DMA controller present on all PC motherboards. The newer model PCs employ very large scale integrated circuits (VLSIC) to reduce chip count and do not have discrete INTEL 8237A-5 chips, but faithfully emulate the functions (and shortcomings) of the original INTEL part. A single 8237 DMA controller has 4 independent channels, only 2 of which are used by the system itself.

The DMA manipulates data by taking control of the memory read (MEMR) and memory write (MEMW) control lines on the system bus. The MEMR and MEMW lines are active low

when either a memory read or write cycle is occurring. Input/output cycles (I/O) are identified to the system bus by either the I/O-READ or I/O-WRITE lines becoming active. These lines (MEMR, MEMW, I/O-READ, I/O-WRITE) along with the 20 address lines, are how the system determines the source and destination of data on the data bus. When the 8088 requires memory access, it generates the appropriate 20 bit address and toggles either the MEMR or MEMW lines depending on whether read or write accesses are desired. The system bus decodes the address and requests memory to retrieve or place the data to or from the address as the case may be. The data bus will then either deliver or accept the data requested by the processor. The 8237 DMA controller arbitrates memory-data transfers, but neither sources nor sinks data. Instead the 8237 DMA controller will generate the necessary address and toggle either the MEMR or MEMW and I/O-READ or I/O-WRITE lines depending on its programmed mode.

Sequence of Events in a Typical DMA Transfer

The following list describes in detail the actions taken by a PC during the course of a typical DMA cycle.

1. Before a DMA operation can occur the 8237-5 controller must be initialized to perform the proper type of cycle. The following list is a summary of the items requiring initialization before transfers can begin.

    - Select read to or write from memory function.
    - Type of transfer: burst or single byte.
    - Byte count to be transferred
    - Priority of channels.
    - Memory address for start of transfer.
    - Unmask and enable the channel's request signal.

2. A card in one of the slots on the system bus sends a DMA request signal (DRQ) to the controller requesting a data transfer on a specific channel. The chip has 4 channels, 0, 1, 2, 3. Channels 1, 2, and 3 are available for user interface cards.

3. The 8237-5 controller prioritizes this request with requests from other channels and sends a Hold ReQuest (HRQ) to the 80x8x processor wait state generation circuitry thereby informing the processor of a pending DMA request.

4. The wait state circuits scan the processor's status lines and look for a processor-passive state. This indicates either no bus activity or a bus cycle about to end.

5. When a passive state is detected, the DMA control logic sends a not ready signal to the 80x8x processor. The processor goes into a wait state at time T3 of the next 80x86 cycle. Time T3 of a processor cycle occurs just before the CPU performs any kind of data bus access. A HOLD Acknowledge (HOLDA) signal is sent to the 8237-5 controller by the wait state generation circuitry. This indicates that the bus will be free at the next clock cycle. Signals are also sent to the bus address, control and data buffers, which isolate the CPU from the system bus by tristate logic chips. It is noteworthy that CPU cycle T3 occurs in the middle of most 80x8x instruction cycles. This allows the DMA circuitry access to the bus even though the processor is interrupted in the middle of processing an instruction.

6. The 8237-5 will detect the HOLDA signal and send a Dma ACKnowledge (DACK) signal to the requesting interface adapter. The system bus supports three such signals, DACK1, DACK2, and DACK3. One signal line for each of the 8237-5 controller's available channels. The DACK signal acts as a chip select to the data acquisition interface card, enabling it on the system bus.

7. The 8237-5 controller will now drive an address onto the system bus, pointing to the memory address where the data transfer will take place. The 8237-5 controller will also take control of the bus control lines (MEMR, MEMW, IOR, IOW), and perform the actual read and write operation on the bus. It should be noticed that the 8237-5 controller neither sources or sinks data, but acts as a bus arbitrator. The 8237-5 controller generates memory addresses and provides chip selects for interface adapters to either read data in or strobe data from memory.

8. The device that generated the DRQ signal, after receiving the DACK signal, will then drop the DRQ signal to the 8237-5 DMA controller. The controller, after completing the cycle, will drop the HRQ to the wait-state control logic. The wait-state controller will then drop the HOLDA signal to the DMA controller, indicating that the 80x8x microprocessor will again take over the bus.

8237-5 Control Registers

Command Register

The command register defines the basic operating modes of the chip. Because the 8237-5 controller is integral to the normal function of the PC bus architecture, any modification of the command register from its normal mode will cause the PC to fail within a heartbeat.

Bit 0 enables memory-to-memory transfers. Because the 8237 controller can only perform these transfers between channels 0 and 1 this feature must be disabled (channel 0 is used to refresh system memory). Bit 1 is enabled only for memory-to-memory transfers. Bit 2 is used to enable or disable the DMA controller. Bit 3 is for a special compressed DMA cycle using only 3 clock cycles instead of the normal 5. This feature should not be enabled as it would reduce the pulse widths generated for memory and port I/O addresses below their limits thereby causing unreliable operation. Bit 4 selects a rotating priority mode

which is incompatible with normal PC operations. This is because DMA channel 0 performs a refresh cycle on the systems dynamic ram every 15.12 μseconds. As the system's memory refresh circuitry must have the highest priority bit 4 is set to 0. Bit 5 selects the timing of the bus cycle's write signal. Because the system's dynamic memory cycles are triggered from the leading edge of the write signal this bit is programmed to perform DMA transfers on the late write selection. To program otherwise would trigger DMA write cycles before MEMR, MEMW lines were valid. Bits 6 and 7 select the active levels for the DRQ and DACK signals. If bit 6 is set to 0, DRQ is active high, while if bit 7 is were set to 0, DACK would be active low. The PC's Read Only Memory (ROM) Basic Input Output System (BIOS) programs this register with a hex value of 00 on power up. The bit fields for this register are summarized in Figure 3-6.

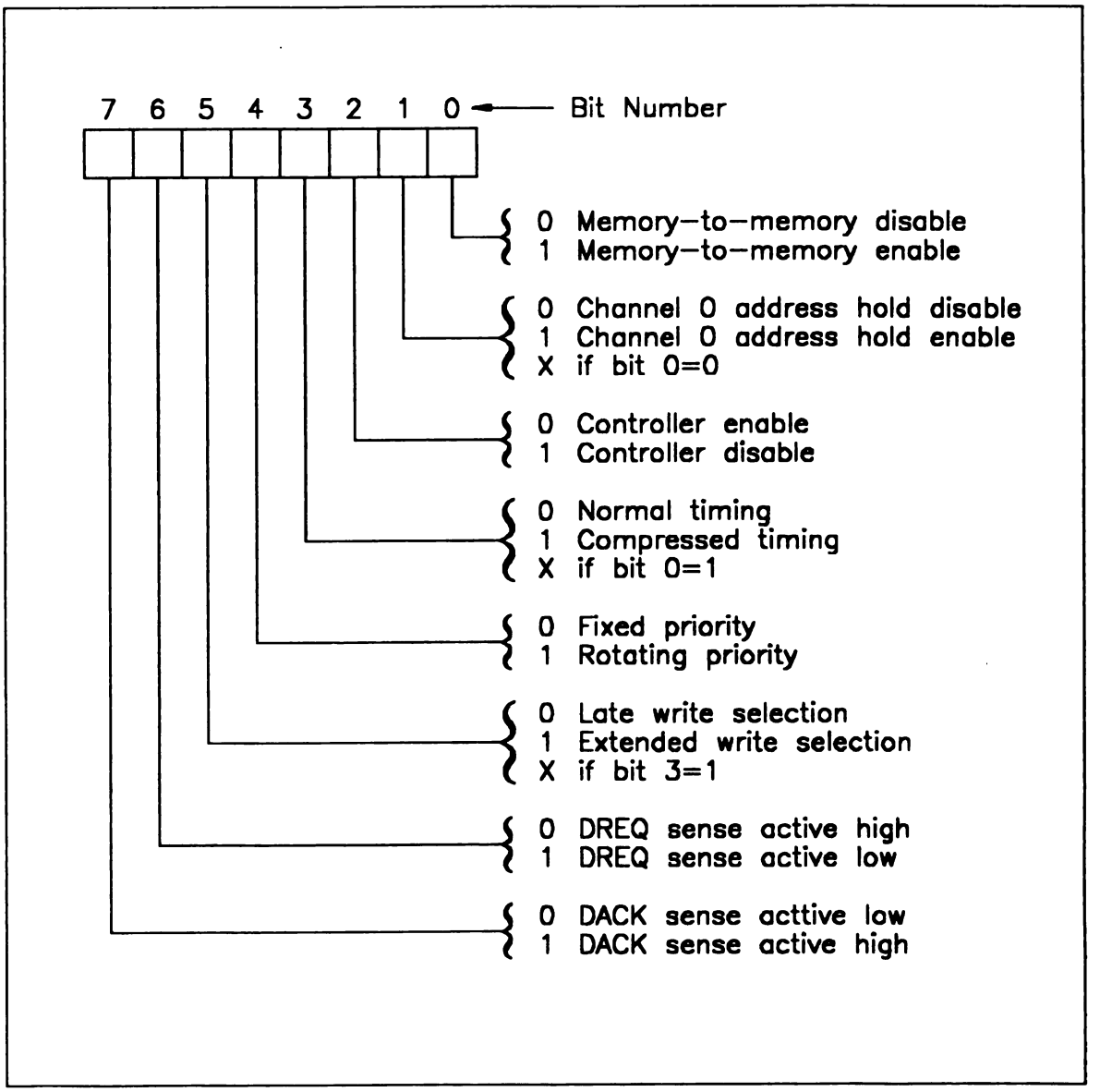

Figure 3-6

8237 DMA Controller Command Mode Register

Write Request Register

The write request register is located at I/O port hex 0009. This register can be used to generate a DMA request under software control. The bit definitions explaining its uses are shown in Figure 3-7.

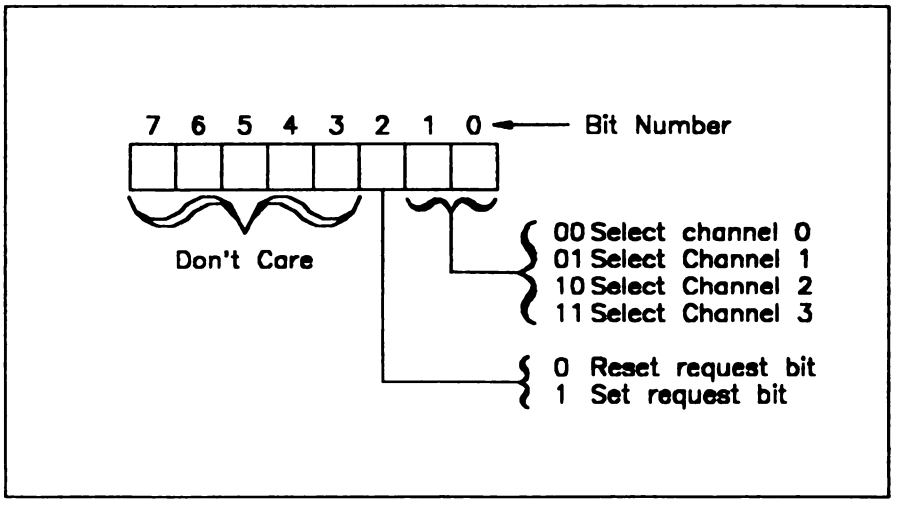

Figure 3-7

DMA Write Request Register

Single-Mask Bit Register

This register permits disabling/enabling of any individual DMA channel. The bit pattern that describes its behavior is illustrated in Figure 3-8. It is located at hex 000A in the PC's I/O address space.

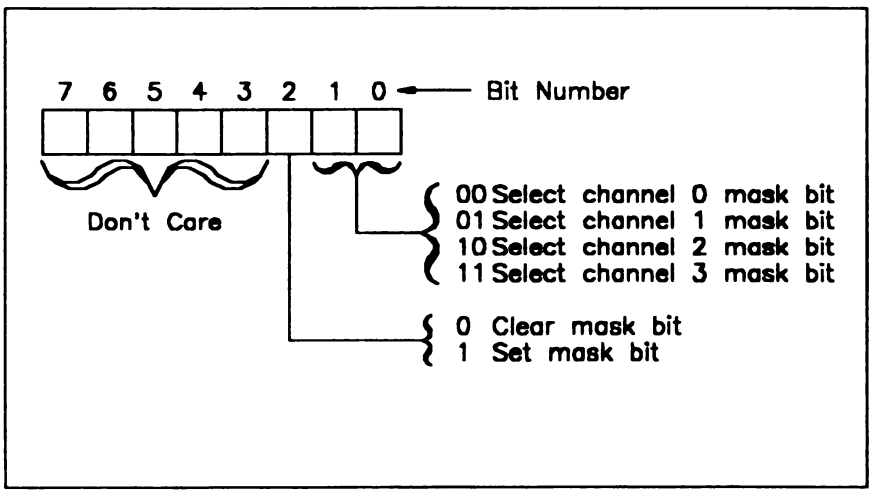

Figure 3-8

DMA Single Mask Bit Register

Mode Register

These write only register defines the basic mode of operation for each of the four DMA channels. Its configuration is summarized in Figure 3-9. It can be loaded by writing to I/O port address hex 000B. Bits 0 and 1 are used to select the DMA channel to which the mode command will apply. Bits 2 and 3 describe the type of DMA cycle that are to occur. There are three types of bus cycles available: (1) a verify operation that performs a bus cycle without a write operation occurring (used by channel 0 to refresh systems dynamic ram), (2) a write operation that takes data from an interface or adapter and writes it into system memory, (3) a read operation that takes data from memory and writes it to the interface adapter. Bit 4 enables a special auto-initialization mode for a specific channel.

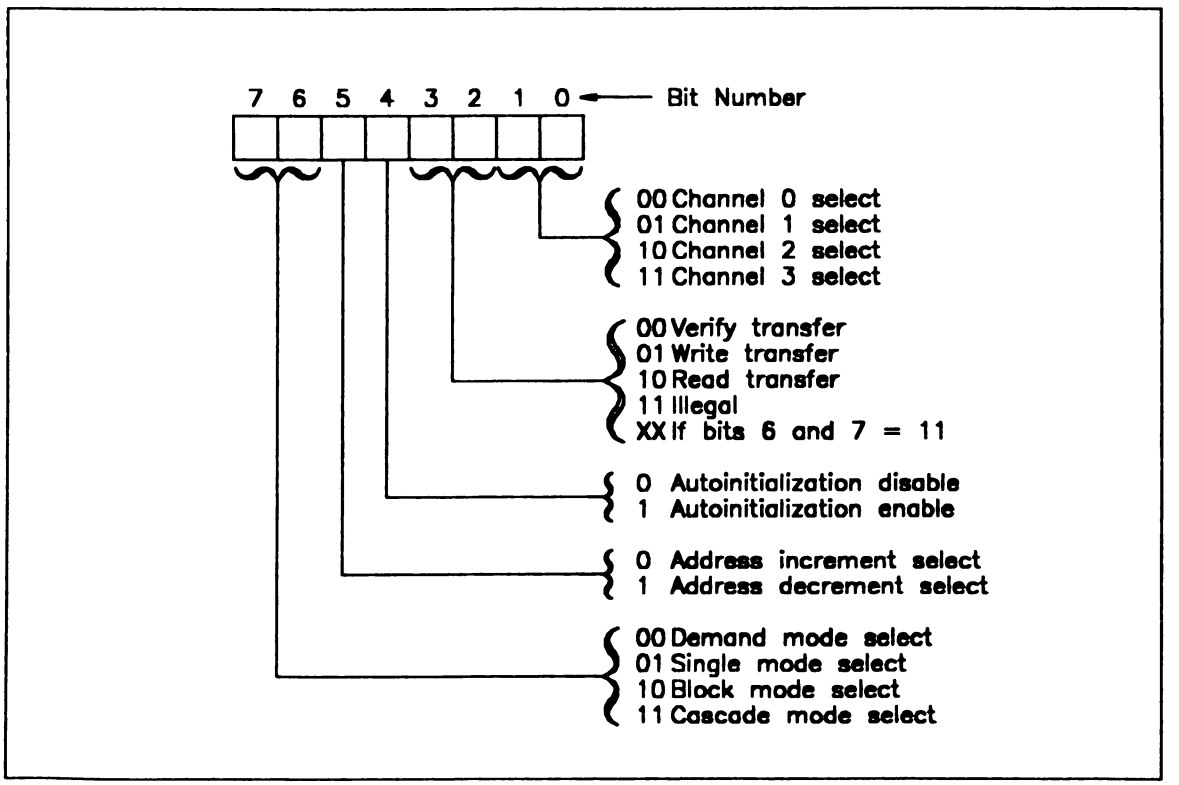

Figure 3-9

DMA Mode Register

When the 8237-5 controller is either reading or writing from memory it keeps track internally of the starting memory address to read to or write from, the number of bytes to read or write, and the memory address currently being accessed. When the controller has read or written the last byte for which is was programmed, it generates a terminal count (TC) signal. If auto-initialization is enabled, the 8237-5 DMA controller will reload itself with its initial parameters and continue to service DMA requests from the active channels. If auto-initialization is disabled, any further DMA requests received for that particular channel are ignored. This feature is useful for repeatedly strobing the same block of memory out to an interface adapter. If the adapter contained a fast digital-to-analog (D/A) converter, the stored digital waveforms could be displayed on an oscilloscope. Bit 5 selects either an increment or decrement function for the selected DMA channel's current address selector. Bits 6 and 7 are used to select the type of DMA operations permitted on the selected channel. The 4 basic modes available are:

1. Single Transfer Mode - where the DRQ signal must be raised for each and every byte transferred.

2. Block Transfer Mode - a single DRQ request will initiate the transfer of an entire block of data. The transfer is stopped when the terminal count is reached. Because this function uses DMA channel 0 to point to the source block and DMA channel 1 to designate the destination, it cannot be used on the 8088 class PCs. The 8088 class PCs have only one DMA controller, while AT class PC's have two (DMA channel 0 is used by the system for memory refreshes and is unavailable for other use).

3. Demand Transfer Mode - data are transferred as long as the terminal count has not been reached and the DRQ request signal is active. This mode can be used if the DRQ line is dropped frequently to permit periodic memory refresh cycles to occur.

4. Memory to Memory Transfer Mode - data are transferred from the memory space addressed by DMA channel 0 to the memory location addressed by DMA channel 1. Because DMA channel 0 is dedicated to refreshing the system's dynamic RAM, this mode is unavailable on XT's. The AT class computers have a second uncommitted 8237 DMA controller that provides 4 additional DMA channels. This allows AT class computers to perform this type of memory-to-memory DMA transfer.

Other DMA Control Ports

Other I/O ports used to program the control parameters for the 8237-5 are as follows. A master clear of the 8237-5 controller is performed by any write to I/O port address hex 000D. The controller requires initialization after the master clear is sent. Any write to I/O port hex 000E will reset all 4 DMA mask register bits, thus enabling all four channels. The write all mask register bits reside at PC port address hex 000F. This port will individually and simultaneously write all four of the DMA channel's mask register bits. The bits in this register are defined in Figure 3-10. The controller's status register can be obtained by reading PC I/O port address hex 0008. This register contains status bits that indicate if a channel has reached terminal count. The bits are defined as shown in Figure 3-11.

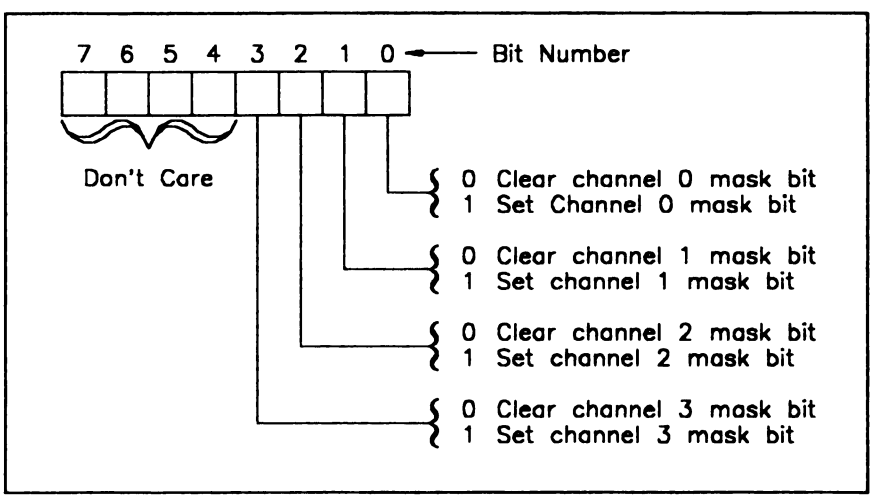

Figure 3-10

DMA Write All Mask Registers

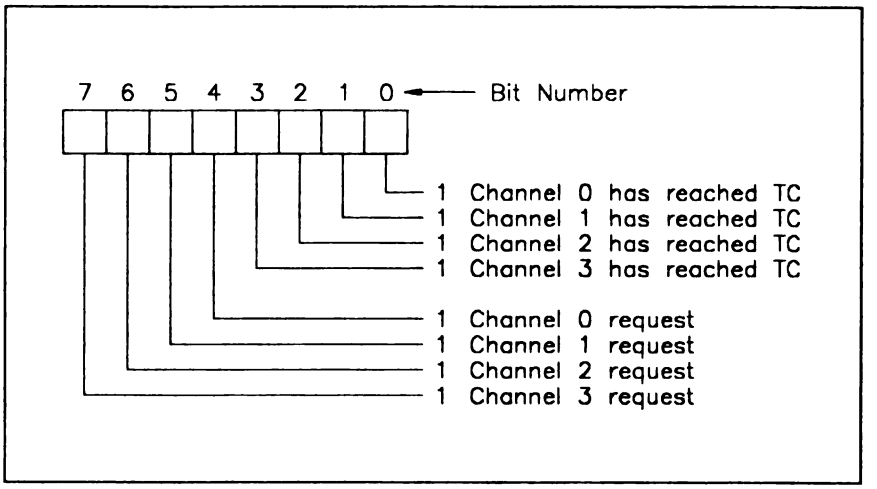

Figure 3-11

DMA Status Register Bits

Address and Counter Registers

Each DMA channel has four 16-bit registers that are used to designate the memory location for the transfer and the number of bytes to transfer. The starting memory address where transfers are to occur is loaded into the base count register of the DMA controller by writing to a write only PC I/O address. A read from the same address will return the current address where the memory transfer will take place during the next DMA cycle. A base and current address pair exist for all four channels. A write to any base address register simultaneously updates the current address register.

The number of bytes to be transferred before the operation is terminated or reinitialized is written to the base and current word count address. Table 3-3 gives a list of the address and count registers. The status of an internal flip-flop determines whether the high or low byte of any register is accessed. The flip-flop toggles whenever a read or write operation occur at any of the four address or count registers. The flip-flop can be brought to a known state (high), by any write to the PC I/O address port hex 000C.

Table 3-3

Port Addresses for the PC Word-Count and Address Registers

Channel	Register	Operation	I/O Address	Internal Flip-Flop	8-Bit Data Bus DB0-DB7
0	Base and Current Address	Write	0000	0	A0 - A7
				1	A8 - A15
	Current Address	Read	0000	0	A0 - A7
				1	A8 - A15
	Base and Current Word Count	Write	0001	0	W0 - W7
				1	W8 - W15
	Current Word Count	Read	0001	0	W0 - W7
				1	W8 - W15
1	Base and Current Address	Write	0002	0	A0 - A7
				1	A8 - A15
	Current Address	Read	0002	0	A0 - A7
				1	A8 - A15
	Base and Current Word Count	Write	0003	0	W0 - W7
				1	W8 - W15
	Current Word Count	Read	0003	0	W0 - W7
				1	W8 - W15
2	Base and Current Address	Write	0004	0	A0 - A7
				1	A8 - A15
	Current Address	Read	0004	0	A0 - A7
				1	A8 - A15
	Base and Current Word Count	Write	0005	0	W0 - W7
				1	W8 - W15
	Current Word Count	Read	0005	0	W0 - W7
				1	W8 - W15
3	Base and Current Address	Write	0006	0	A0 - A7
				1	A8 - A15
	Current Address	Read	0006	0	A0 - A7
				1	A8 - A15
	Base and Current Word Count	Write	0007	0	W0 - W7
				1	W8 - W15
	Current Word Count	Read	0007	0	W0 - W7
				1	W8 - W15

DMA Page Registers

The 8237-5 DMA controller made its debut in 1978 as a high speed data transfer coprocessor on 8-bit computer systems. The chip, therefore, only supports memory transfers throughout a 64Kb address space. To span the 1 Mbyte address space offered by the early PC's requires, however, 20 bits. The 8237-5 DMA controller therefore requires that additional circuitry (in the guise of a page register) be present to augment the DMA controller and facilitate 20 bit addressing. The page register for DMA channels 1, 2, and 3, can be read and loaded using the PC I/O port addresses 81 hex, 82 hex, and 83 hex, respectively. These page registers are simply 74LS614 4 byte data latches. The corresponding page register for each channel is chosen by the appropriate DACK signal through activating the chip select (CS) input. The full 20 bit address is comprised of a 16 bit word and a 4 bit nibble. These are combined to give the composite 20 bit address (Figure 3-12).

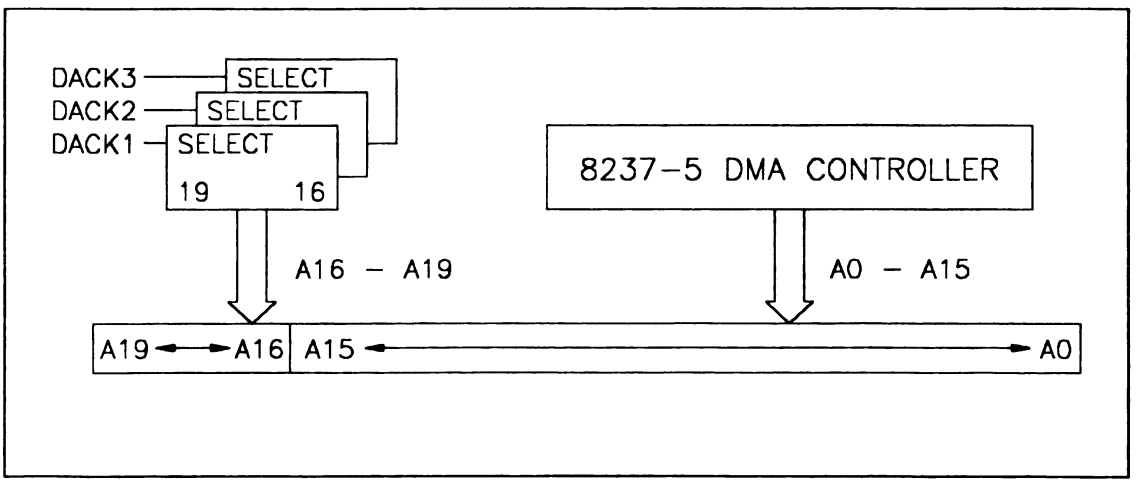

Figure 3-12

DMA Memory Address Generation

DMA Performance

Programmable 8237-5 DMA controllers previously existed only on discrete chips. With the preponderance of Very Large Scale Integrated Circuits (VLSIC) chip sets, the original 130+ Integrated Circuits (IC's) present in the original PCs have been condensed into, or onto, two VLSICs. Condensed down along with the mundane collection of 74LSxxx series chips was the DMA controller. The functionality and register compatibility of the original 8237-5 controller has been maintained and improved by the VLSIC chips that replaced the discrete 8237-5 DMA controller. This discussion pertains to the original 8237-5 controller, which has since fallen out of use. The specifications for the PC On A CHip ((POACH) set manufactured by Chips and Technology of Milpitas, CA) are almost identical to those of the discrete 8237-5 controller. The only exception arises because the POACH set can operate with a 10 MHz clock, as opposed to the 5 MHz limit for the discrete chip 8237-5 controller.

Each DMA cycle requires 5 processor clock cycles. The baseboard logic inserts an extra clock cycle as a wait state. This wait state is added to ensure sufficient time for transfers to occur between memory and the slower I/O interface channel. Each DMA cycle should therefore take 6 clock cycles to complete. However the PC's design requires the DMA controller to be run in the single-byte-transfer mode. This means that at least one 80x8x CPU bus cycle must occur between each DMA cycle. Since the 8088 CPU bus cycles are 4 clock cycles long, this time must be added to the minimum DMA cycle time. This gives a 4.77 MHz PC with a 210 ns clock cycle a maximum DMA transfer rate of $210\frac{\text{ns}}{\text{clock-cycle}} \times 10\frac{\text{clock-cycles}}{\text{transfer}} = 2.1\frac{\mu\text{s}}{\text{transfer}}$ or 476 kilobytes/second. The original 4.77 MHz PC is actually faster than the newer 8 MHz AT's when performing byte sized DMA transfers. This is because in the PC design the DMA controller is clocked at 4.77 MHz. In the original AT design the 8237-5 is clocked at only 3 MHz. The 16 bit

80286 and the 32 bit 80386 based PC's can, however, perform 16 bit memory transfers. IBM PCs or compatibles based on the 80286/80386 contain the equivalent of two 8237-5 controllers. The second controller present in AT class machines is offset wired one bit on the address bus. The low bit is asserted as a zero whenever the second 8237-5 controller generates an address. This means the second controller can only generate even number addresses. This is done so that the second controller can only perform word size transfers starting on even byte boundaries. This offset wiring allows word size transfers as well as byte size transfers to be accommodated. Relatively low cost (under $600) 80286/80386 PC's with 8-10 MHz I/O channels (typical spec) can perform memory transfers at $\approx$ 2.5 MHz per word.

OTHER HARDWARE SERVICES AVAILABLE ON THE PC MOTHERBOARD

The 8259 Interrupt Controller

The 8088 microprocessor has two interrupt ports available: a maskable interrupt input and a nonmaskable interrupt (NMI) input port. The NMI port is only available on the motherboard and is used exclusively to support the math coprocessor, handle baseboard RAM parity errors, and service an I/O channel check request. An Intel 8259A interrupt controller is attached to the maskable interrupt port. The 8259A extends the maskable interrupt port to eight prioritized interrupt levels. Of these 8 interrupt ports available, only 6 are available to user I/O cards. A summary of all interrupt ports and their usage is shown in Figure 3-13 and described in Table 3-4.

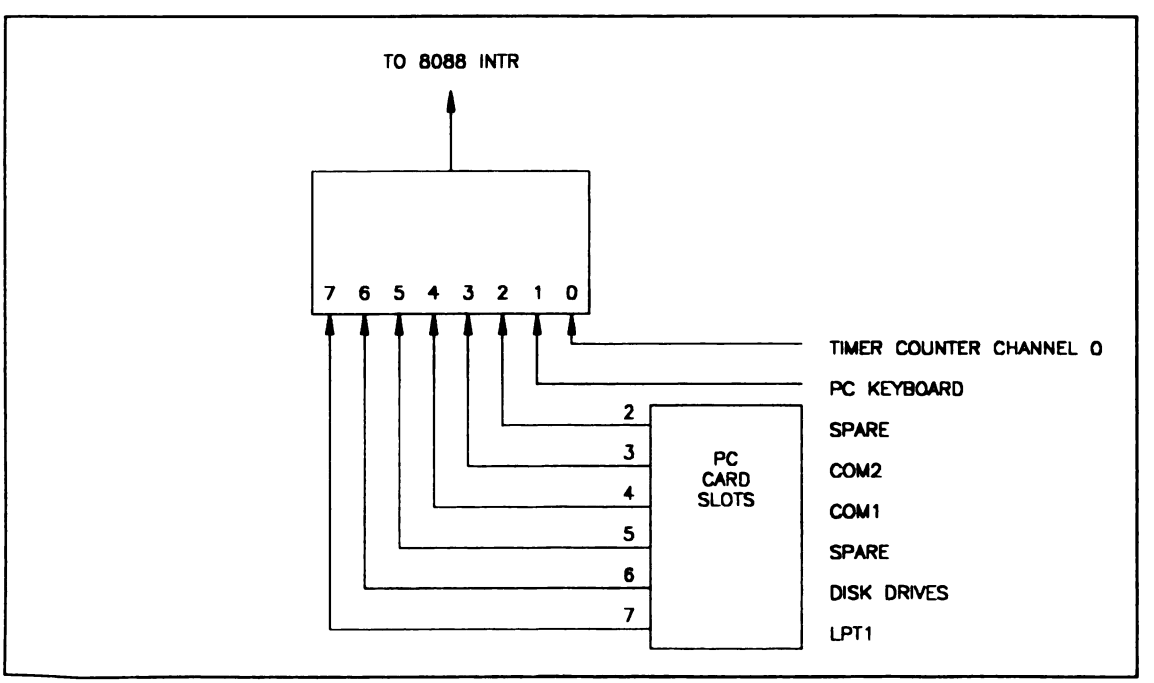

Figure 3-13

Interrupt System Block Diagram

Table 3-4

PC Interrupt Usage		
Interrupt Level		**Usage**
Highest Level	NMI	Baseboard RAM parity. I/O channel check, numeric processor
	IRQ0	System timer output (8253-5 channel 0
	IRQ1	Keyboard hardware interrupt (key struck)
Available on System Bus	IRQ2	No official use in PC, used sometimes to service mouse interrupts. Unavailable on an AT, this is cascaded to another (slave) 8259A to provide another 8 interrupts.
	IRQ3	RS-232 serial port, COM2:
	IRQ4	RS-232 serial port, COM1:
	IRQ5	Not used at present
	IRQ6	Diskette/Hard drive
	IRQ7	Parallel printer port, LPT1: (usually unused)

Figure 3-13 represents graphically the key elements of the PC interrupt system. The integral nature of the 8259A interrupt controller to the systems operation prohibits the user from altering the chips programming from its default values. The following list describes the sequence that occurs when an interrupt is detected and serviced.

1. An interrupt request is received by the 8259A controller from one of its 8 inputs. The interrupt source is either the motherboard or a peripheral in a system bus expansion slot.

2. The interrupt controller receives the request and prioritizes it with the other requests that may be either coming in or pending.

3. If the request is the only one, or is the highest level pending, an interrupt request is sent to the 80x8x processor.

4. The 80x8x processor sends two INTerrupt Acknowledge (INTA) pulses to the 8259A interrupt controller. The first freezes the priority of pending interrupts and sets the levels in the service latch. The second INTA request an 8 bit pointer value.

5. The 8088 then receives the 8 bit pointer value on the data bus. This pointer value is used to index into a low memory table, which contains the far address of the software interrupt-service routine for the specific level that is being serviced.

6. Next, the 80x8x processor fetches the far address of the current instruction being executed and pushes it on the system stack along with the current flags, and then, branches to the newly fetched far address retrieved from the low memory table.

When the processor drops whatever its doing to service a "hot" interrupt, a certain amount of housekeeping is performed to assure system integrity. In the highly likely event the Interrupt Service Routine (ISR) is going to use some 80x8x registers, they should be pushed onto the stack. Thus when the ISR is finished and is ready to return, the registers can be restored. It will also be necessary to notify the 8259A of interrupt service completion, (by sending it an End Of Interrupt (EOI) signal) so that additional interrupts can be received . Additional requests from the 8259A to the 80x8x processor are still masked off. This occurs automatically within the 80x8x whenever an interrupt is serviced. The status of the 80x8x processors maskable interrupt is available as a bit in the processors flag register. This bit can be enabled by the 80x8x assembly language instruction STart Interrupts (STI), or by POPing the old status register from the stack during the RETurn.

System Initialization for Interrupts

1. The PC initializes all the interrupt vectors in low memory to point to an address in the system Read Only Memory (ROM) which contains an IRET instruction. The first 1024 bytes of the 8088 address space are reserved for a four-byte pointer to any of 256 possible interrupts. The four-byte nibble consist of an IP and a CS value. The basic input output system (BIOS) initializes only the interrupt vectors it is using.

2. The 8259A is initialized, this includes programming the chip for non-rotating priority mode and unmasking the interrupt port for all initialized interrupt vectors.

3. Unmask the system interrupt in the 8088 CPU by setting the status bit in the flag register.

4. A peripheral generates a hardware interrupt with a rising edge at one of the 6 available interrupt request lines on the 8259A.

5. The 8259A gets the request and sets the request latch and sends an INTR request to the 80x8x microprocessor.

6. The 80x8x responds with an INTA (INTerrupt Acknowledge) pulse which prioritizes the request in the 8259A's request latch. This freezes the priority of all pending interrupts currently being handled by the 8259A.

7. The 80x8x sends the second INTA pulse, which the 8259A controller responds to by sending a value from 0-7 to the 80x8x processor. This value corresponds to the 8259A port that requested the interrupt.

8. The 80x8x masks off all interrupts, pushes its flag register onto the stack, along with the current CS and IP. Then it fetches the new CS and IP generated using the pointer into the interrupt vector table returned by the 8259A controller in the previous step.

9. The interrupt service routine pushes onto the stack all registers that it will use and could destroy.

10. The interrupt routine will now execute, performing its designed task. The interrupt routine may issue an EOI signal to the 8259A controller to permit additional interrupts to occur while the current one is being serviced.

11. At the completion of the service routine, the previously PUSHed registers are restored by POPing them from the stack.

12. Lastly, the service routine executes an Interrupt RETurn (IRET) instruction that unmasks the interrupts (by POPing the previously PUSHed flag register), pops the old CS and IP from the stack, and branches to these values and picks up execution from where it was interrupted.

Interrupt Servicing Latency

In instances where the time required before the processor begins servicing an interrupt is critical, it is necessary to understand those factors that determine interrupt service latency.

1. The actual processing time from the point of the processor receiving the interrupt request from the 8259A, getting the interrupt level and pointers from the 8259A controller, pushing the current CS and IP on the stack and branching into the interrupt service routine is 61 clock cycles for an 8088 (39 for an 80286). At 210 nanoseconds per clock cycle in a 4.77 MHz PC this is 12.81 μseconds.

2. Interrupts are only serviced at the end of an 80x8x instruction. An interrupt request received at the beginning of an instruction won't be serviced until the end. Typically instructions require 4-20 clock cycles to execute (1 to 5 μseconds). Some 8088 instructions such as MULTiply and DIVide require 180+ clock cycles to execute, while certain 8087 instructions, such as calculating a logarithm require 997 clock cycles (≈ 200 μseconds).

3. If the interrupt request is a low priority it must wait for higher priority interrupts to be serviced. Likewise, if a time-critical lengthy interrupt service routine is being processed, the pending routine must wait until the current routine releases the 8259A controller and the 80x8x processor.

As is the case with the 8237-5 DMA controller, the 8259A interrupt controller rarely exits in its discrete form. The 8259A is incorporated onto on of 4 VLSICs along with the functional equivalents of the rest of the 90+ discrete logic chips which used to comprise the PC motherboard.

80x8x Address Segmentation

A brief description of the 80x8x address segmentation is in order before a presentation of the steps necessary to prepare the system to properly service interrupts, The 80x8x processors running the DOS operating system operates in "real mode". When operating in real mode, the processor can only address 64Kb at a time. The full address of the currently executing instruction is the sum of two 80x8x registers. The first register is the Code Segment (CS) register and the second is the Instruction Pointer (IP). Both registers are 16 bits wide. The 8088 address space is 1 Mb, requiring 20 bits to specify any unique location. The 8088 CS register views this address space as being comprised of 65,536 paragraphs, each paragraph being 16 bits in size. The full address is constructed from the CS and IP by using the CS to point to the starting paragraph while the IP points to an offset from the starting paragraph. Figure 3-14 shows how the CS and IP are combined to generated any address in a 20 bit (1 Mbyte) address space (each hex number is 4 bits). This is why it is necessary to save both CS and IP if the processor is to return from any point in memory.

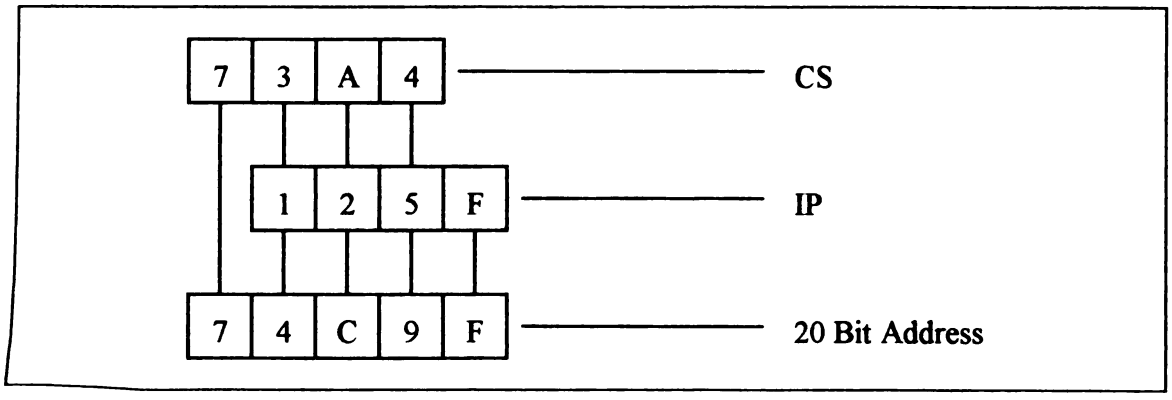

Figure 3-14

8086/8088 20 Bit Address Generation

PC DISK OPERATING SYSTEM (DOS) AND OTHER SYSTEM SOFTWARE SERVICES

The original FORTH operating system made rather rigid and logical use of disk storage devices. FORTH views the disk as a random block device, each block being 1024 bytes in length. The logical blocks are sequentially mapped to physical sectors. Therefore logical block one was the first physical sector on the disk. Any coherence between blocks was up to the imagination of the programmer. Random disk entry and retrieval required an excellent memory as typical mass storage devices contained between 360 to 3000 blocks. FORTH makes no provisions for the logical mapping of associated blocks into files and could only copy physical blocks in sequential order.

The PC's Disk Operating System (DOS) provides for such mapping to allow related sectors to be associated as files. High level commands such as COPY and TYPE reduced file manipulations to triviality compared to the sequential mapping of FORTH. Along with structured files, DOS provides provisions for the allocation of system memory between several concurrent applications. Support and drivers exist for a multitude of hard disks and graphics cards, making unnecessary the custom drivers required by earlier FORTHs.

HIGH SPEED DATA ACQUISITION INTERFACE BOARD DESCRIPTION

The function of the interface adapter is to generate the necessary signals to drive the TN-6123 detector, digitize the VIDEO OUT signal, and store the digitized data. This was accomplished using a custom designed interface card based on commercially available components. The basis for the interface card is the JDR PR-2 prototype board (JDR Microdevices, Los Gatos, CA.). The JDR PR-2 is a standard full length size card with address decode logic, buffered I/O, data lines, and test point circuitry silk screened onto the card. The card is gridded with plated through holes on 0.1 inch centers. The front is rimmed with a ground plane while the back has +5 volt power connections. The JDR PR-2 has approximately 10.5 by 4 1/2 inches of usable board space for design. The card fits conveniently into any of the systems available 62 pin interface slots. The interface card was used without modification to respond to the I/O port addresses 300-31F hex. Unfortunately the address decode logic on the card disabled the buffered data lines to the PC whenever the PCs bus Address ENable (AEN) line was asserted true. This only happens when a DMA cycle occurs. The AEN signal disables the processor from the system bus during DMA cycles. This has the undesirable side effect of disabling the interface card's data lines from the PC's bus. The buffered data lines on the card are therefore not used.

To successfully digitize and archive the information from a single array element in real time, the interface card must provide the following basic signals in the order shown.

Required Signals and Timing to Drive the PDA

1. After a start pulse has loaded a binary "1" into the array's shift register, signal STB (see fig 3-15) will cause the TN-6123 to drive an analog pulse onto the VIDEO OUT line. The appearance of the peak of the analog pulse appears after a delay of duration time T1 (as shown in fig 3-15).

2. The sample and hold amplifier then latches the analog VIDEO OUT signal. A delay of time T2 gives the sample and hold amplifier (DATEL SHM-20, DATEL Inc., Mansfield, MA.) sufficient settling time, typically 700 ns.

3. After the held analog signal has stabilized, it is digitized by a 12 bit analog-to-digital converter (HAS-1202, Analog Devices, Sunnyvale, CA.). This occurs during time period 3 (Figure 3-15), which is 2.8 μseconds worst case conversion time.

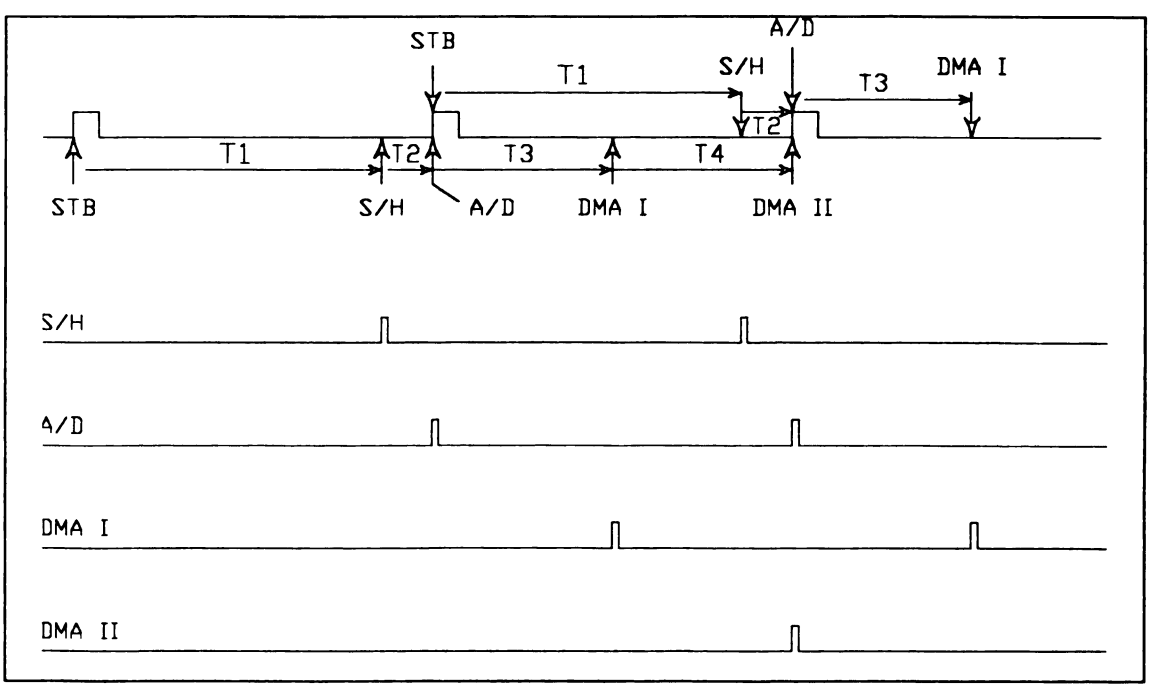

Figure 3-15

Array Scanning Sequence Timing Diagram

4. A properly initialized DMA controller then transfers the digitized signal to a pre-determined memory location. Two DMA cycles are required because a PC bus bandwidth limits data transfers to 8 bits per cycle. Circuitry on the interface board generates two successive DMA transfers from a single request.

8254 Counter-Timer

Precision timing is necessary to accomplish the entire sequence rapidly enough to acquire a complete spectrum on the stopped flow time scale (>>10 ms). To scan the entire array in this time frame requires sampling, digitization, and storage of 12 bits of data in no more than 18 μseconds. To achieve the necessary resolution in timing control, a pair of Intel 8254-2 programmable timers were used. These timers are software compatible with the 8253 timer used on the PC's motherboard. The 8254-2 timer is able to accept a 10 MHz clock as opposed to a 2 MHz rate for the 8253 timer. Each timer chip consist of 3 independent timers. By cascading 2 chips and having the output of one counter serve as the trigger input to the following counter, a series of precision timing pulses suitable to run the array and acquire data was generated .

As each counter is driven by a 10 MHz clock, timing pulses can be made to appear reproducibly within a 100 ns resolution window. The interface board uses two 8254-2's, each with three independently programmable timers. Each 8254-2 timer has separate pins for the three control signals required to drive each timer. These signals are labeled OUT, GATE, and CLOCK. The operating modes of the counters are programmed independently by writing a control word to the control word register. The bit definitions for the control word are as shown in Figure 3-16.

The interface board uses the 8254 counters only in modes 1, 3, and 5; therefore only these three modes will be described.

D7	D6	D5	D4	D3	D2	D1	D0
SC1	SC0	RW1	RW0	M2	M1	M0	BCD

SC - Select Column

SC1	SC2	
0	0	Select Counter 0
0	1	Select Counter 1
1	0	Select Counter 2
1	1	Read Back Command (Reads present status)

M - Mode

M2	M1	M0	
0	0	0	Mode 0
0	0	1	Mode 1
X	1	0	Mode 2
1	0	1	Mode 5

R/W Read Write

RW1	RW2	
0	0	Counter Latch Command
0	1	Read/Write least significant bit (LSB)
1	0	Read/Write most significant bit (MSB)
1	1	Read/Write LSB first then Read/Write MSB

BCD

0	Binary Counter 16-bits
1	Binary Coded Decimal (BCD) Counter (4 Decades)

Figure 3-16

8254-2 Programmable Timer Command Mode Register

8254 Counter Timer Operating Modes

Square Wave (Mode 3)

Mode 3 is the square wave mode and produces an output waveform with a 50% duty cycle (Figure 3-17). The counter serves as a divide by "n" counter, where "n" is the count programmed into the counters input. The signal OUT will be initially high. When half the initial count has expired, OUT goes low for the remainder of the count. Mode 3 is periodic with the sequence being repeated indefinitely. An initial count of N results in a square wave with a period of N CLOCK cycles. When the input GATE = "1", counting is enabled, conversely a low at GATE disables counting. A rising edge at GATE causes the counter to be reloaded with the initial count ("n") on the next clock pulse. Thus the GATE input can be used to synchronize the counter. Writing a new control word and count to the command register causes the counter to be reloaded on the next clock pulse. This allows the counter to be synchronized by software as well.

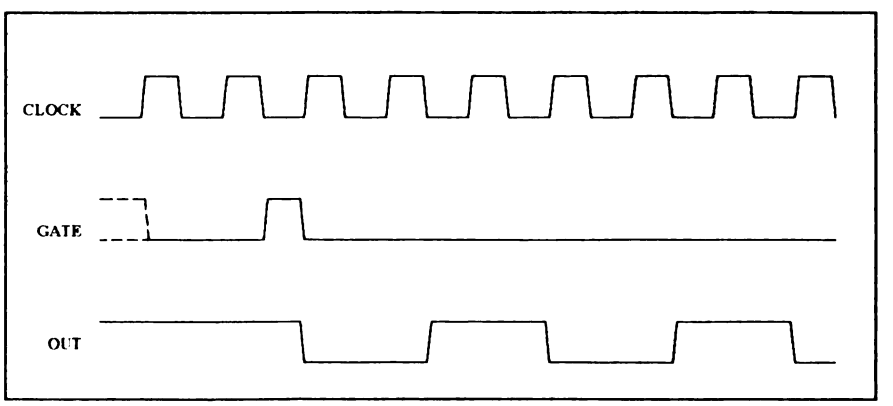

Figure 3-17

Mode 3 square wave mode

Hardware Retriggerable One-Shot (Mode 1)

In mode 1, the counter operates as a hardware retriggerable one-shot (Figure 3-18). Output signal OUT will be initially high, OUT will go low on the CLOCK pulse following a rising edge at GATE, and will remain low until the counter reaches zero. OUT will then go high and remain high until the CLOCK pulse after the next trigger. After writing the control word and the initial count, the counter is armed. A trigger (rising edge at GATE) results in loading the counter and setting OUT low on the next clock pulse, thus starting the one-shot pulse. An initial count of N will result in a one-shot pulse N CLOCK cycles in duration. The one-shot is retriggerable; thus, OUT will remain low for N CLOCK pulses after any trigger. The one-shot can be repeated without rewriting the same count into the counter.

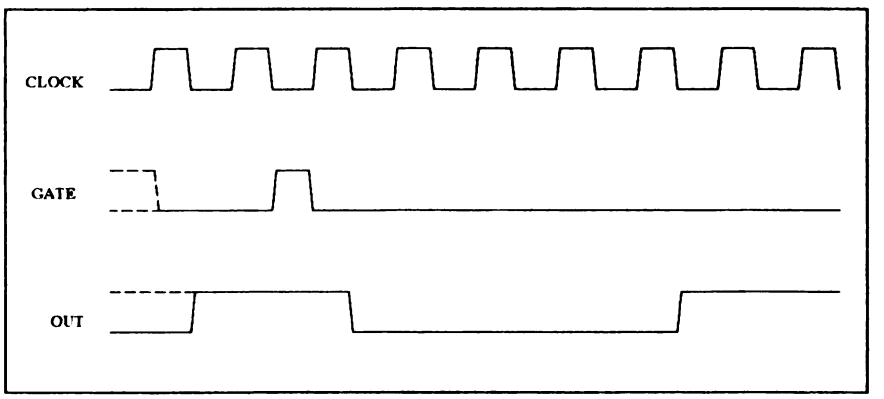

Figure 3-18

Mode 1 hardware retriggerable one-shot

Hardware Retriggerable Strobe (Mode 5)

Mode 5, called the hardware triggered strobe mode, is similar to mode 3. Initially OUT will be high. Counting is triggered by a rising edge of GATE. When the initial count has expired, OUT will go low for one CLOCK pulse and then go high again (Figure 3-19). After writing the control word and initial count, the counter will not be loaded until the CLOCK pulse after a trigger (rising edge at GATE). This first CLOCK pulse does not decrement the count; hence, for an initial count of N, OUT does not strobe low until N+1 pulses after a trigger. A trigger results in the counter being loaded with the initial count on the next CLOCK pulse. The counting sequence is retriggerable.

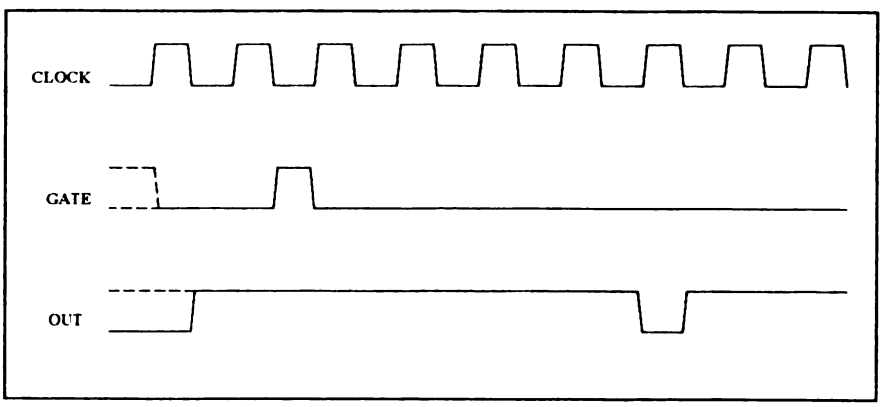

Figure 3-19

Mode 5 hardware retriggerable strobe

Control Signal Synchronization and Generation

As previously described, the 6 independent digital counters are chained together to provide precision timing pulses for data generation, capture, digitization, and storage. The following section gives an explanation of the processes involved in pulse generation and data acquisition.

Start Pulse Generation

As its name would imply, the generation of the START pulse is the logical first step in initializing the array. The START pulse loads a logical "1" into the diode array's shift register that subsequent STB pulses use to generate sequential data. When the software is loaded, counter 1 is programmed to operate in mode 3, which is the symmetrical square wave mode. It is desirable to have the processor issue the START pulse so that it can perform any housekeeping chores required between scans. Such chores include modifying the DMA registers, modifying scan rates, adjusting the page registers, or watching for the termination flag. Because the rising edges of the STB pulses occur every 6 μseconds, the processor cannot successfully watch for the occurrence of the edges and trigger the START pulse. It is necessary for the processor to issue a "request" to the hardware for a START pulse to be generated and let the start pulse generation circuitry handle the timing.

When it wants a scan is to begin, the processor issues a start request, which is just a rising edge to an edge triggered 74LS74 D type flip-flop. This causes the Q output of the 74LS74 to go low immediately. This low output is fed to the inverting input of an AND gate (pin 9 Figure 3-20) on the 74LS423 monostable multivibrator. Any occurrence of a rising edge at pin 10 of the monostable and a low at pin 9 will fire the monostable. This produces a single negative going pulse synchronous with the rising edge of STB. The duration of the START pulse (≈1.5 μseconds) is given set by the values of R and C attached to pins 6 and 7. The rising edge of the synchronized START pulse is fed into the PRESET

input to reset the D-Flip-flop (Figure 3-20). The START pulse is buffered on the interface board with an open collector pull-up type driver.

Once generated, the START pulse initiates the readout sequence of the diode array. The rising edge of signal STB is repowered on the board. The START signal must power several loads on the board and be driven through the 25 foot long interface cable supplied with the array head. The rising edge of STB is fed to the input of counter 2, which controls the timing sequence of the sample and hold S/H amplifier (SHM-20 DATEL Inc., Mansfield, MA.).

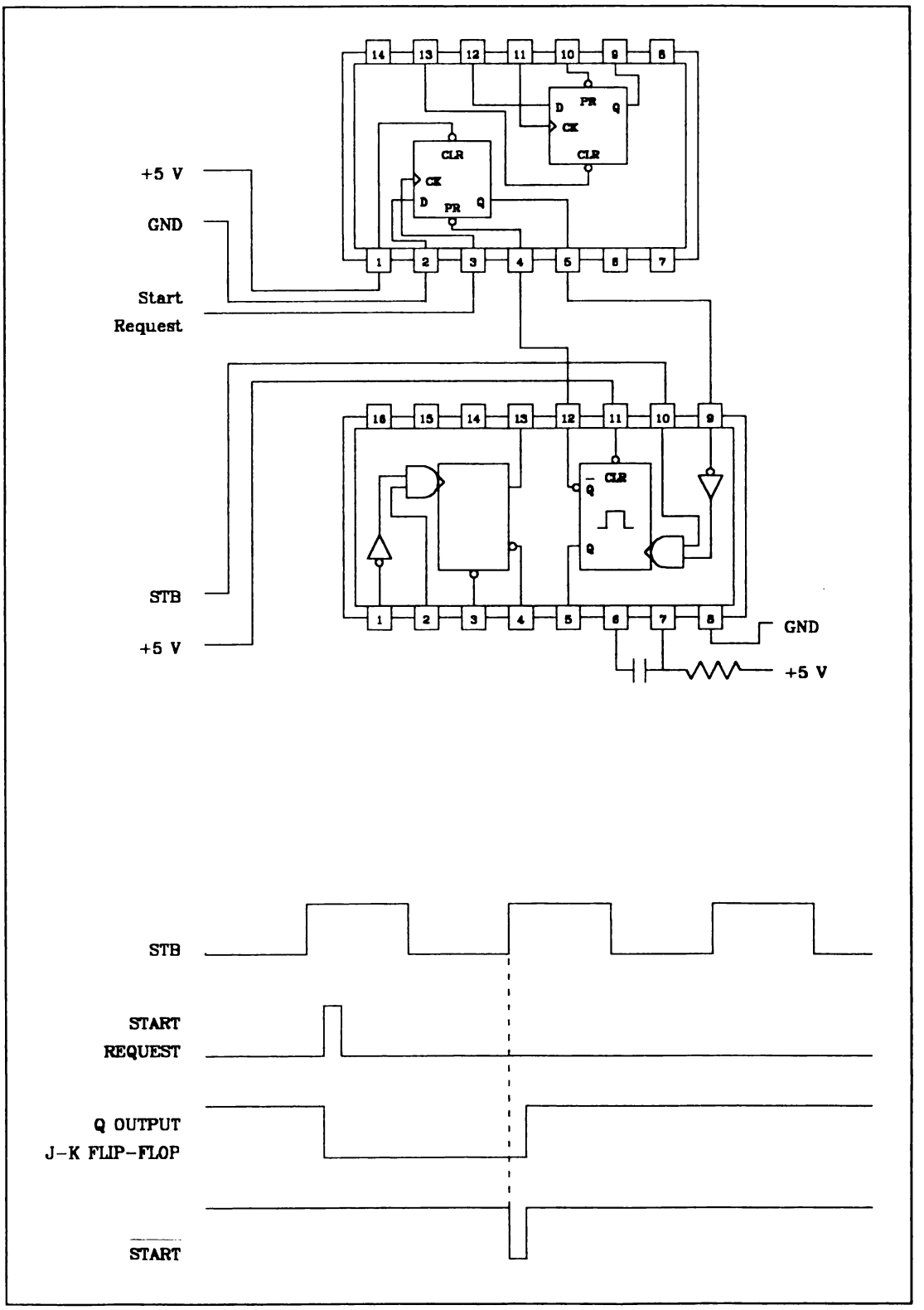

Figure 3-20

START Pulse Generation Circuitry and Timing

S/H Pulse Generation

The S/H amplifier is run in the track and hold mode on the interface board. The analog data pulses appear at a constant time after the application of a rising edge of signal STB (Figure 3-21). The peak amplitude of the analog video signal was found experimentally to occur 700 nanoseconds after the rising edge of STB. The rising edge of STB is used as a GATE signal to counter 2, whose clock input is driven by a 10 MHz oscillator. Because counter 2 is initialized with an initial count of 7 it will wait for 7 clock cycles (700 ns), before going low for one clock cycle. The rising edge of STB also goes to PRESET (pin 10) of the 74LS74 D-Flip-flop, which sets the Q output of the flip-flop high immediately. The Q output is used to engage the S/H amplifier into the track mode, whereby it follows the analog input signal. The retriggerable one-shot pulse from counter 2 arrives 700 ns later at the clock input of the 74LS74 flip flop to latch the D input (Figure 3-21). This causes the S/H amplifier to stop tracking the analog input signal and hold the present value.

The optimum time delay of 700 ns for the occurrence of the peak maximum was determined by trial and error. From 700 ns to 900 ns the output analog signal changes by less than 5%. If the 100 ns resolution of the counters was insufficient to find the peak height accurately, the addition of a monostable between OUT 2 and pin 11 (CK) of the 74LS74 would have provided for more precise timing control.

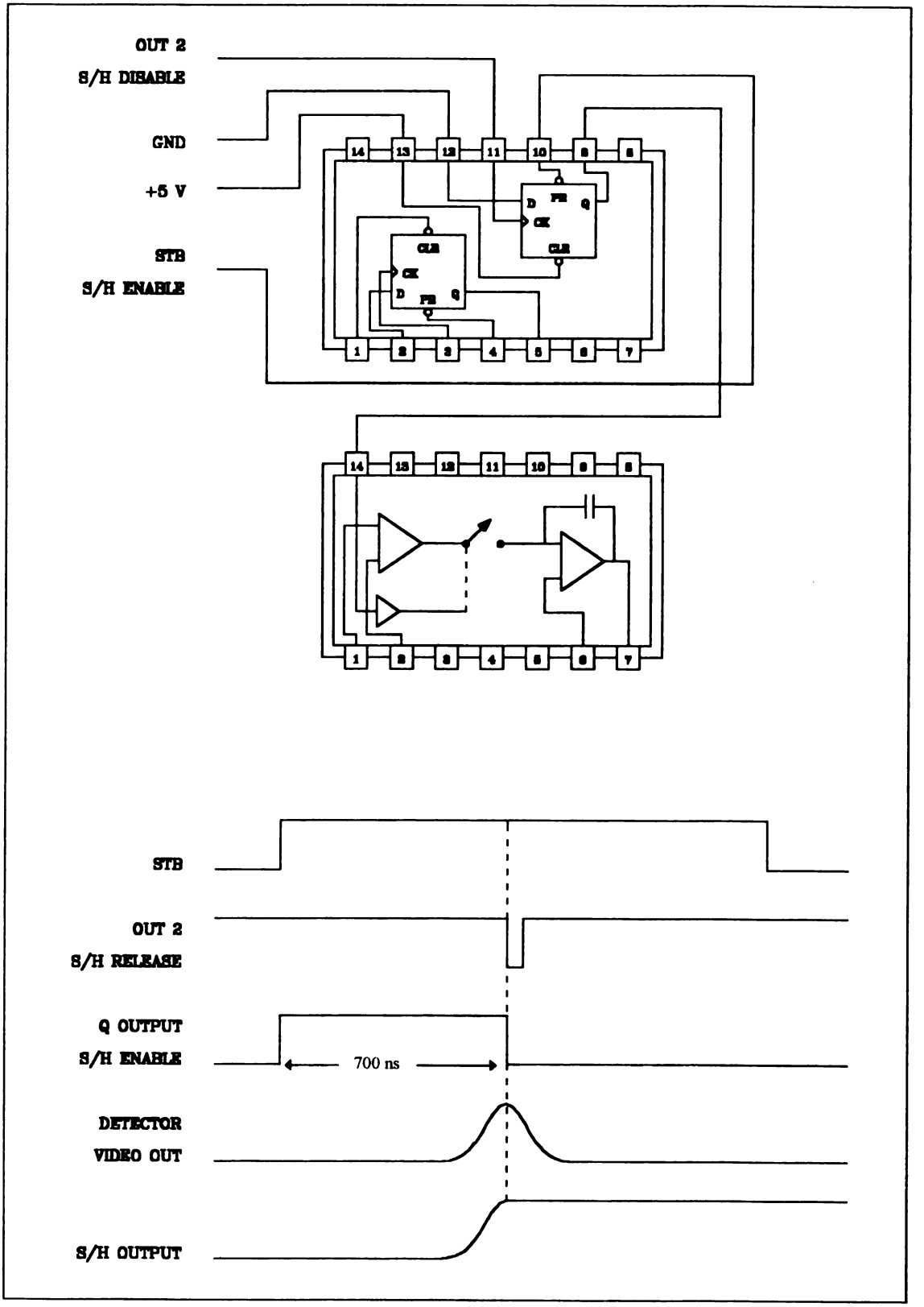

Figure 3-21

S/H Pulse Generation Circuitry and Timing

A/D Converter Pulse Timing

The Analog-to-Digital (A/D) converter (HAS-1202 Analog Devices, Grand Rapids, MI) is activated by a rising edge of a 100 ns wide pulse. The timing for this signal was the easiest to generate, and was accomplished inverting the output of counter 3 (OUT 3). Counter 3 is programmed to operate in the same mode as counter 2, (e.g., a hardware retriggerable one-shot). The counter is triggered by using the S/H convert disable signal (OUT 2) as an input to the trigger of counter 3 (GATE 3). Counter 3 is programmed with a count of 4. This gives a time delay of 400 ns to allow the S/H time to settle to a steady level (see Figure 3-22).

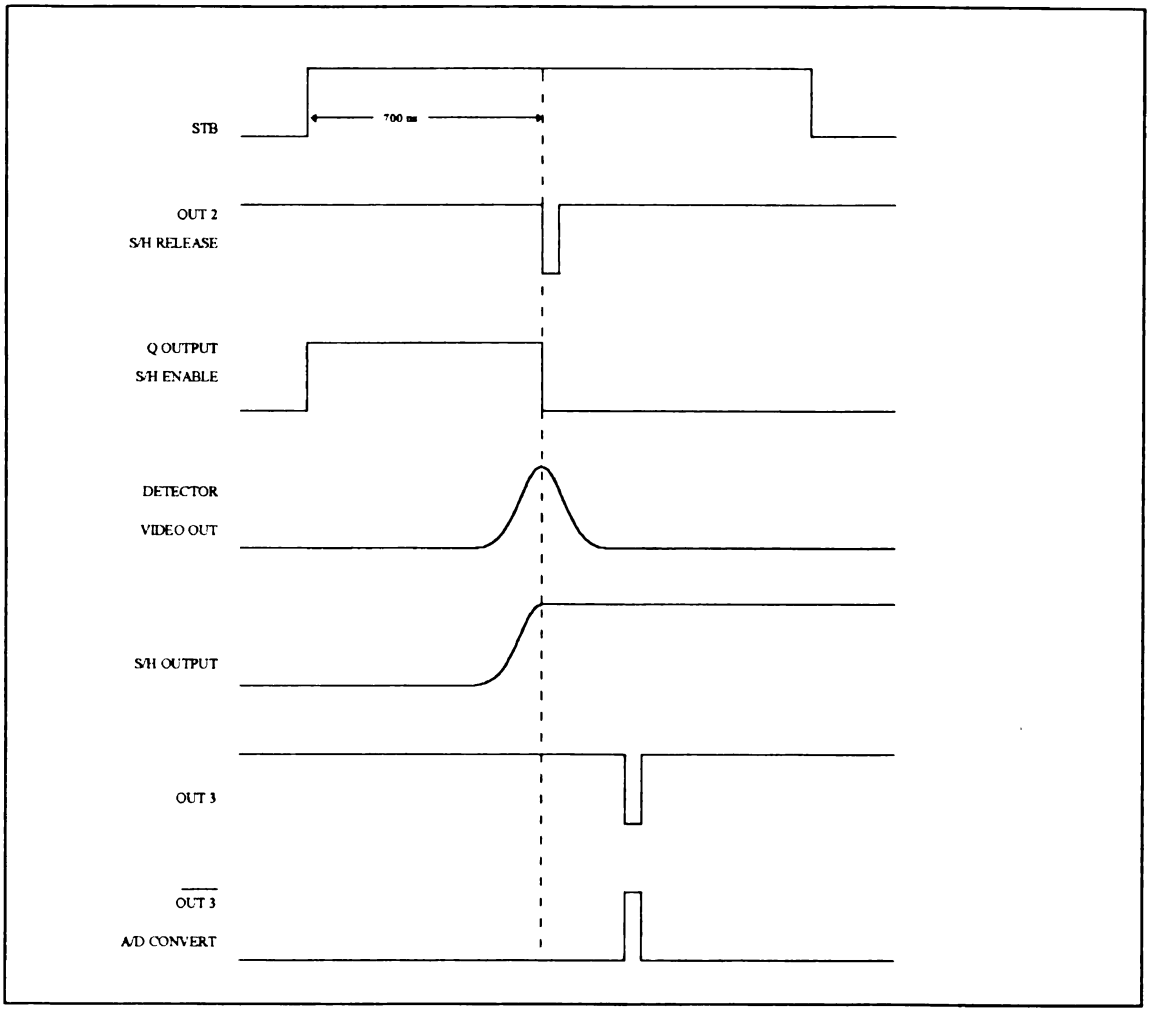

Figure 3-22

Analog-to-Digital Pulse Generation Circuitry and Timing

DMA Logic and Circuitry

In the present system the rate limiting step in capturing data from the array detector is DMA throughput. The A/D converter has a resolution of 12 bits and the PC's data bus is only 8 bits. We must therefore contend with trying to fit a 12-bit wide peg into an 8-bit wide hole. A useful tool is the 74LS604, an octal 2-input multiplexed latch. This chip will latch 16 bits of data on the rising edge of a clock signal and then present either the low (A), or high (B), eight bits at the outputs (Y) depending on the status of its select line (Table 3-5).

Table 3-5

74LS604 Octal 2-Input Multiplexed Latch Truth Table				
INPUTS				OUTPUTS Y1 - Y8
A1 - A8	B1 - B8	SELECT A/B	CLOCK	
A data	B data	L	↑	B data
A data	B data	H	↑	A data
X	X	X	L	Z or Off
X	X	L	H	B register stored data

Assuming the software has initialized the 8237-5 DMA controller by setting the mode, unmasking it, loading the count of bytes to transfer, and pointing the chip to a safe area of memory to perform the transfer, the hardware handshaking necessary to facilitate a high speed data transfer is relatively straightforward. The peripheral requiring DMA services raises one of three available DRQ lines to request DMA service from the appropriate channel. When the PC motherboards wait state logic determines that the PC bus is free, it informs the 8237-5 DMA controller, which pulls the corresponding DACK line active low.

This acts as a signal to the interface adapter to put the data on the PC's bus. When DACK goes high, the transfer is complete and the interface adapter should tri-state itself from the data bus. So, briefly, the sequence is, raise DRQ, drop DRQ and enable data on PC's bus when DACK goes active low, then tri-state the data lines off the bus when DACK goes high.

Unfortunately this process must be repeated twice for each A/D conversion. As mentioned earlier, DMA cycles do not occur at our convenience, but rather at the convenience of the PC's motherboard. Therefore, it would be a waste of time to wait for a worst case DMA cycle to occur each time a data transfer was required. The logic described in Figure 3-23, "DMA Control Logic Timing Sequence", is used to latch the data from the A/D into the 74LS604. Then trip two successive DMA cycles while toggling the 74LS604 between the DMA cycles to transfer low-byte then high-byte.

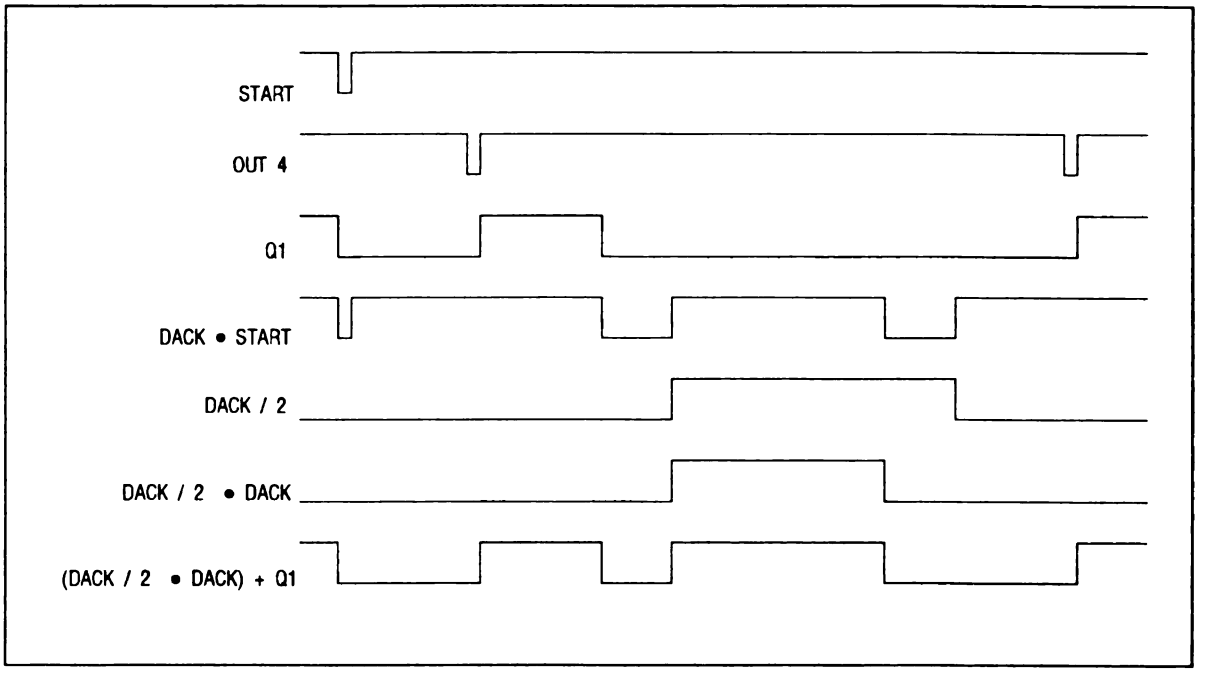

Figure 3-23

DMA Control Logic Timing Sequence

DMA Pulse Generation Sequence

1. The START signal is used to clear both flip-flops on the 74LS109 to bring their Q outputs to an initial low state at the beginning of a scan (Figure 3-24).

2. Signal OUT2, which sends the S/H amplifier from track mode into hold mode, is used to clock the data from the A/D converter into the 74LS604 octal multiplexer. Because the first S/H disable latch signal occurs before the A/D converters start signal, the data actually latched is invalid. The timing sequence is such that on any given cycle, we are DMAing the valid data from the previous cycle. This renders invalid the first and last data points taken. However, because the first and last diode in the array are "dead", nothing important is lost.

3. Signal OUT4 is counter 4 operating in mode 5 (one-shot hardware retriggerable). This signal is initiated by connecting OUT3 to GATE4. Signal OUT3 initiates the A/D conversion cycle; therefore, counter 4 is programmed to wait for 3.0 μseconds (30 counts of the 100 ns clock). This time should be ample to assure the A/D has valid data, as the worst case conversion time for the chip is 2.8 μseconds, (2.2 μseconds typical).

4. The rising edge of OUT4 initiates the request for two successive DMA transfers. The process is best followed by examining (Figure 3-23, "DMA Control Logic Timing Sequence". Simply put the first flip-flop acts as a divide by 2 frequency divider for OUT4, while the second flip flop performs the same function for DACK.

5. Flip-flop output Q1 is initially low due to the low START pulse being present at its CLR input. Signal OUT4 clocks the first flip-flop sending its output high. This signal generates the first DMA request (Figures 3-23 and 3-24).

6. The PC senses this request, and when it can be serviced, signals so by dropping the DACK line (active low). This active low DACK line is used to clear the first flip-flop (dropping the DRQ to the PC bus). Notice that the first flip-flop is cleared by either a low at START or an active low DACK signal (DACK • START). The signal $\overline{DACK}$ is generated to enable a 74LS244 latch, which drives the data from the 74LS604 onto the PC bus (Figure 3-24).

7. When the transfer is complete, the PC raises the DACK signal. This rising edge is used to clock the output of the second flip-flop Q2 (DACK/2). Output Q2 (DACK/2) is ANDed with the DACK signal to produce the signal $((DACK/2) \bullet DACK)$ (see Figure 3-24). This signal goes high immediately after every other DMA request is serviced and goes low whenever the DACK signal is active. This makes it convenient for requesting the second DMA transfer from the PC bus.

8. By allowing signal $((DACK/2) \bullet DACK)$ or signal Q1 to request DMA services, we produce the following logic statement $((DACK/2) \bullet DACK) + Q1$, which is shown graphically in Figure 3-23, "DMA Control Logic Timing Sequence".

9. Because the output Q2 (DACK/2) is high only when the second DMA transfer is occurring, it is used to drive the SELECT A/B input of the 74LS604 octal 2-input multiplexed latch (Figures 3-23 and 3-24).

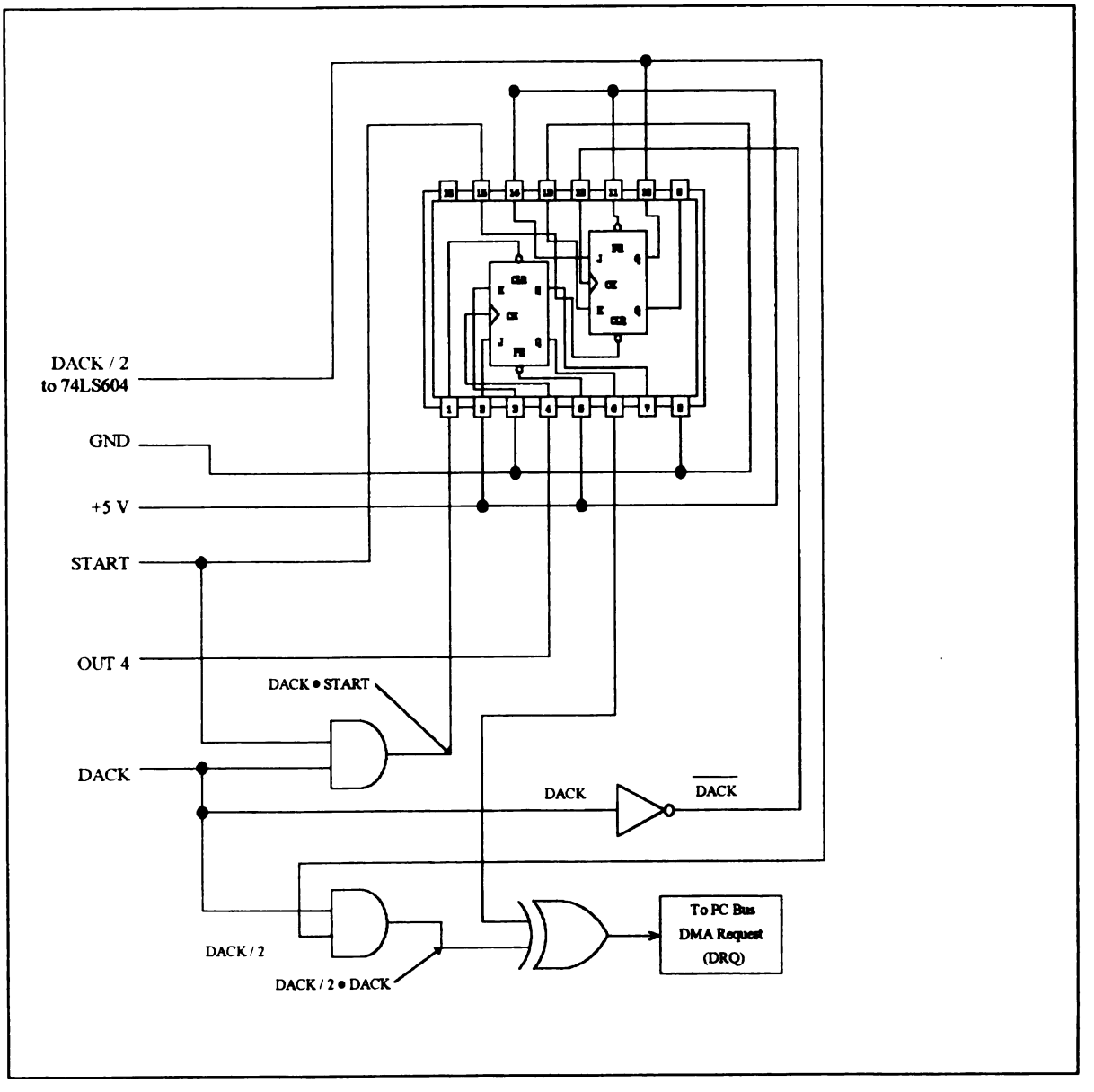

Figure 3-24

DMA Request Circuitry

Maximum Data Rates for Multiple Scans

The interface board repeats the previously described process for all 512 elements in the array. The process repeats every time a START pulse is received. To strobe and collect the data from a single channel requires a maximum of 6.0 μseconds. The bulk of the time is the roughly 4.2 μseconds required for the DMA to transfer a single word. The remainder of the time is spent waiting for amplifiers and analog switches to settle. The maximum practical frequency of the occurrence of start pulses is $\frac{6.0\ \mu\text{seconds}}{\text{pixel}} \times 512\ \text{pixels} \cong 3\ \text{milliseconds}$. The frequency of START pulses, and the scanning frequency of repetitive scans is thus limited to this time frame. Provisions on the interface board are provided for acquiring scans more rapidly by sacrificing resolution. The signal from OUT1, which is STB is used to gate OUT2 (S/H), which gates OUT3 (A/D), which gates OUT4 (DMA). Signal OUT2 is passed through a 74LS191 counter that divides the input by 1, 2, 4, 8, and 16. These divided signals are sent to a 74LS151 1 of 8 multiplexer that selects one of the divided inputs to gate OUT3, and so on. By using sub-multiples of the data sampling and storage pulses (OUT2 through OUT4) data are collected from every 2, 4, 8, or 16th successive diode (Figure 3-25). The benefit of this is the array can be scanned much faster by sacrificing resolution (diodes). The 74LS191 is loaded with an initial count so that the operator maintains control over what the starting array element is, as well as the data acquisition frequency.

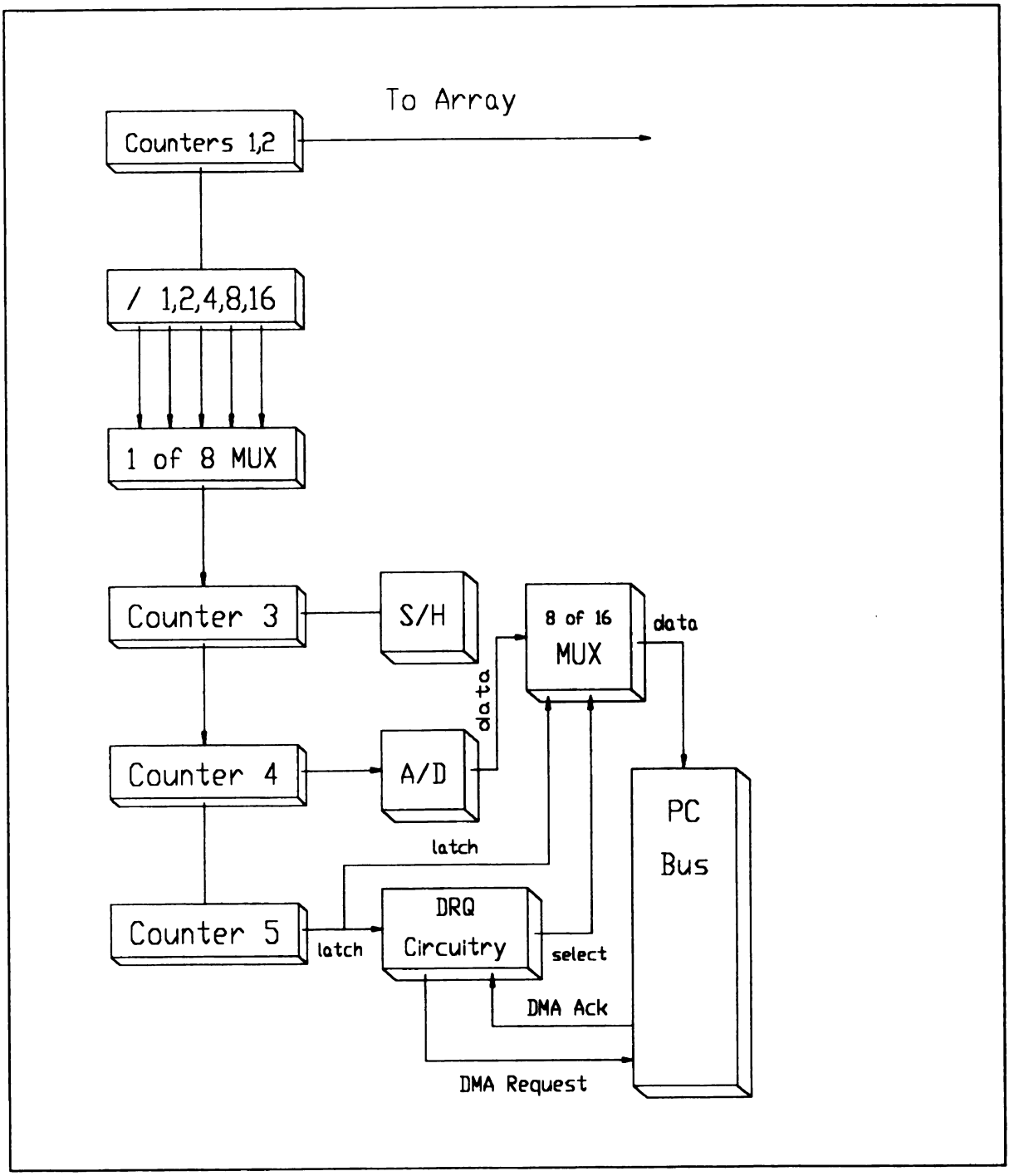

Figure 3-25

Information Flow Chart

Data Acquisition Interface Card

DMA Cycle Summary

Counter 0 is programmed in mode 3, which is the symmetrical square wave mode. Counter 5 is programmed in mode 1, which is the hardware retriggerable one-shot. The START signal is used as a reset for counter 0 and as a trigger for counter 5. Counter 0 is programmed with a count of 10,000, giving is a symmetrical square wave output with a frequency of 1000 Hz. The output of counter 0 is used as the GATE signal to counter 5. Signal OUT5 will go low on the clock pulse following this trigger and remain low until counter 5 has reached terminal count. Counter 5's output will then go high and remain high until the clock pulse after the next trigger. The rising edge of OUT5 is used to signal to the 8259 interrupt controller that a scan has been completed and software intervention is necessary to prepare the system for the next scan (Figures 3-25, 3-26,).

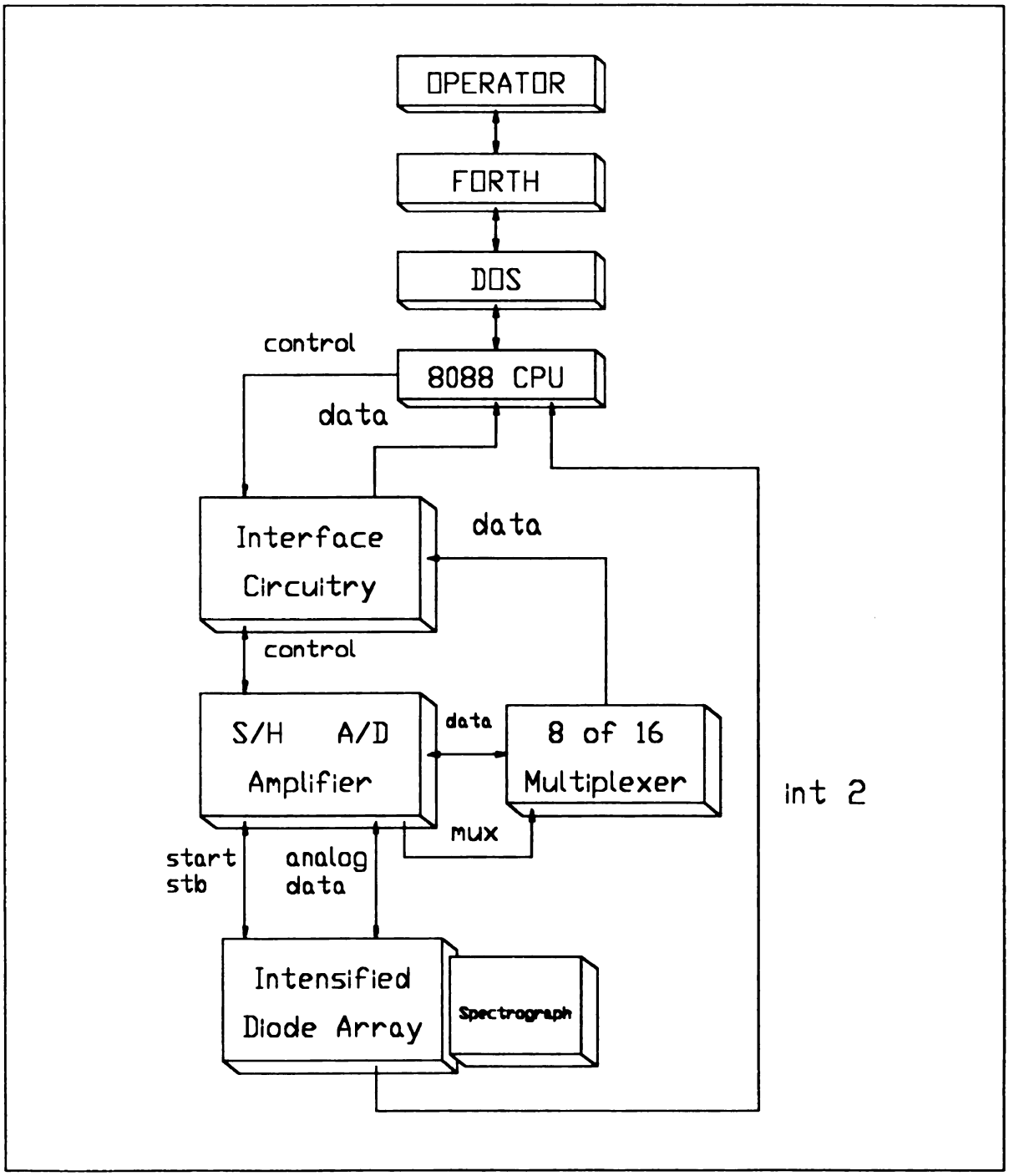

Figure 3-26

Information Flow Chart

Intensified Diode Array Data Acquisition Control System

Analog Signal Conditioning

The VIDEO OUT signal from the array detector ranges from 0-4 V and is driven into a 50 Ω load. To match the 10 volt full scale dynamic range of the A/D converter the signal is fed into an adjustable gain amplifier as shown in Figure 3-27. The output of the amplifier goes into the S/H amplifier. The output of the S/H amplifier has an RC filter with a time constant of roughly 0.2 μs. This was determined experimentally as the best compromise to pass the original VIDEO OUT signal and reject the high frequency bus noise associated with the PC's 14.31818 MHz oscillator and its harmonics.

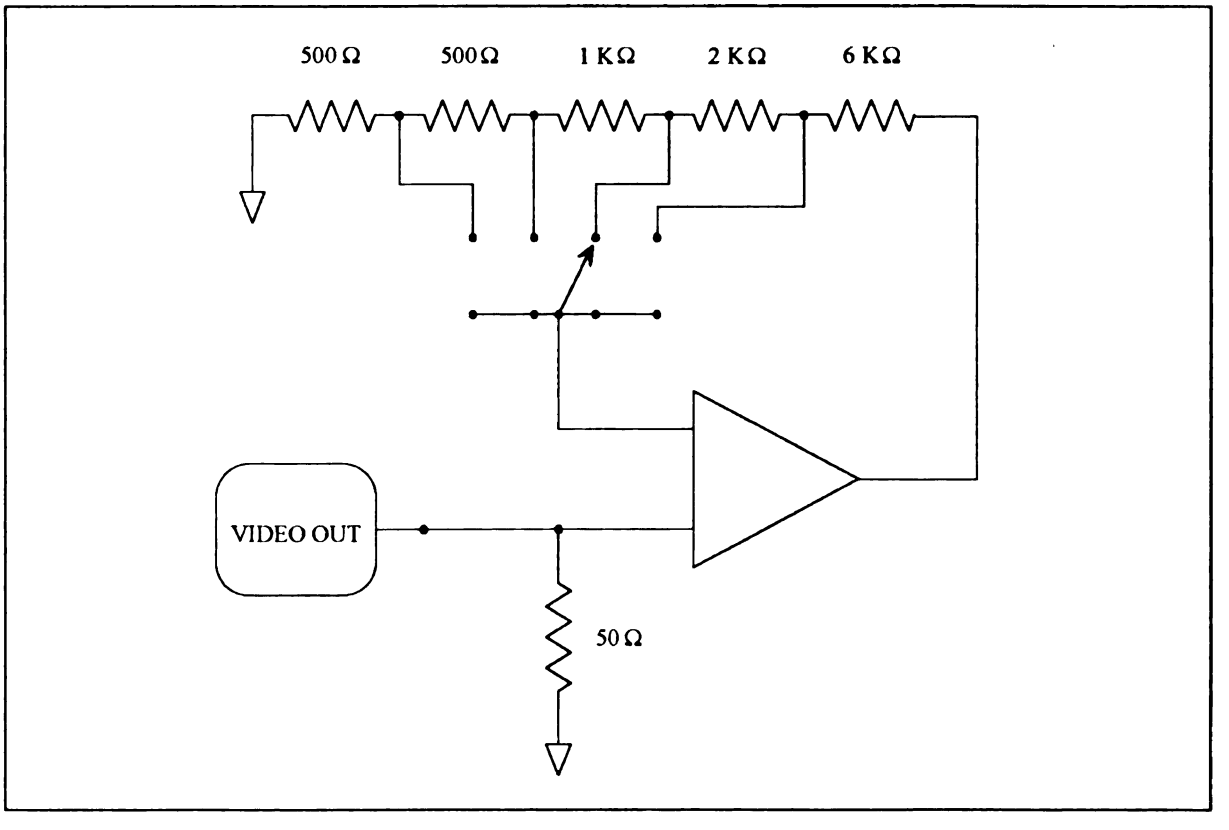

Figure 3-27

Analog Signal Conditioning

SYSTEM OPTICS

This section deals with the design and construction of the system optical bench. The system was designed to detect the low light levels associated with fluorometry. It was also desirable to have the instrument accept several standard sizes of fiber optics. A fiber optic interface would allow the instrument to be moved quickly and easily between different experimental stations with minimal down time. The fiber optic interface does not require considerable realignment time whenever the instrument or the sample cell is moved. The overall optical system is illustrated in Figure 3-28.

The entrance slit assembly (Jobin Yvon Division of Instruments S. A., Princeton NJ.), has interchangeable slits of 25, 50, 100, and 1000 μm widths. Additionally, a V shaped wedge

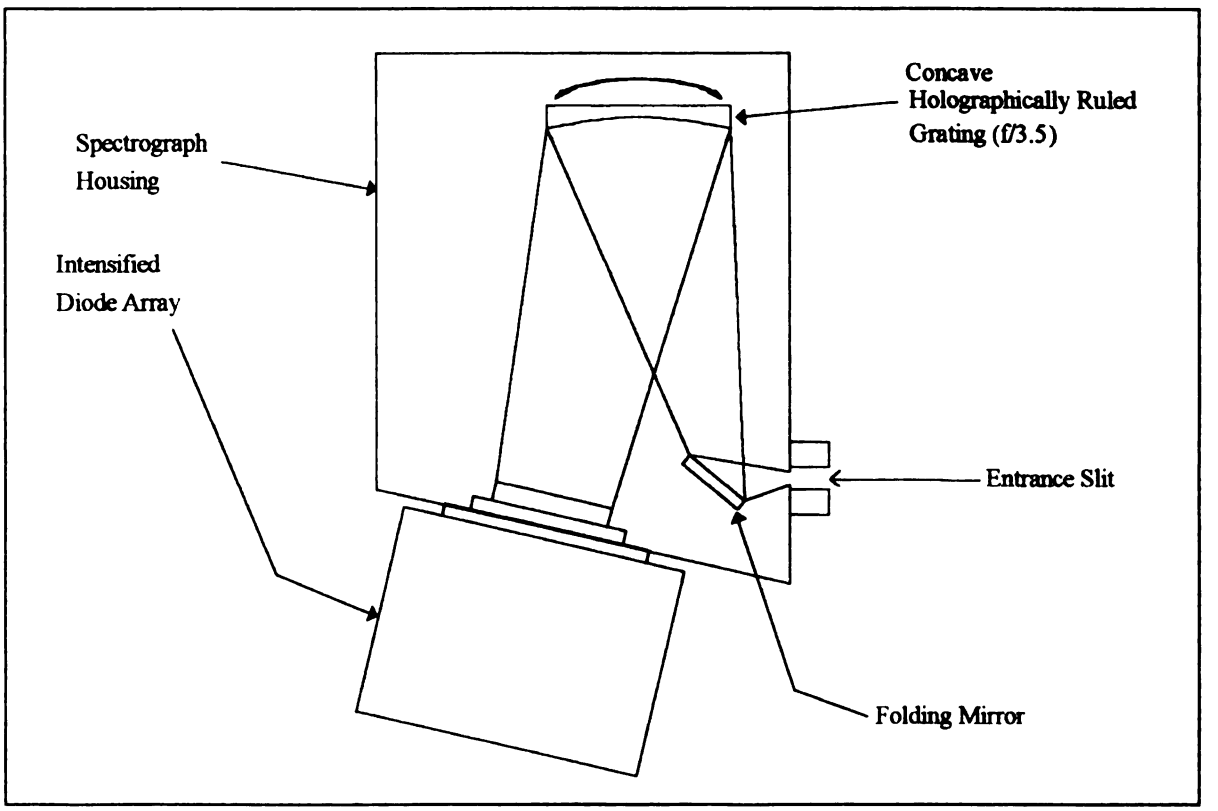

Figure 3-28

Spectrograph with Intensified Diode Array Detector

can be moved horizontally across the face of the slit to adjust its height. This assembly is either found on, or has been adapted to, most of the small monochromators found in our laboratory. The slit assembly is also surrounded by a threaded ring. This threaded ring accommodates adapters that allow us to interface various sizes of fiber optics to our monochromators. The end ferrules of the fiber optic were either round or slit shaped, to interface to either a flow cell or the spectrograph respectively (Figure 3-29). Usually no slits were used when the fiber optic interface was attached. The end ferrule of the fiber served as its own slit, giving a 5 nm bandpass.

As light enters the spectrograph (Figure 3-28), it is reflected by a folding mirror onto a concave, holographically ruled grating (Jobin Yvon Division of Instruments S. A., Princeton NJ.). The concave grating had an experimentally determined focal length of 96.3 mm and a diameter of 50 mm (f/2.0). The flat field spectrographic, concave, aberration-corrected grating was preferred because its blaze gave us a reciprocal linear

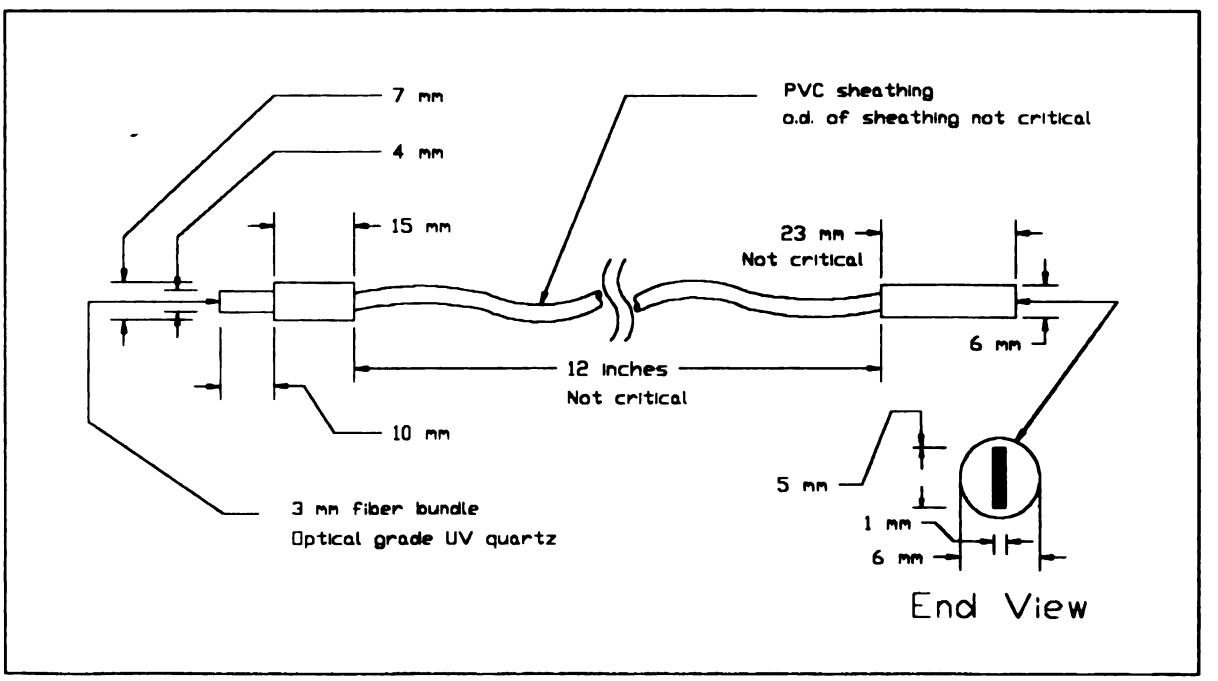

Figure 3-29

Single Fiber Optic Bundle

dispersion of 31.25 nm/mm. As the diode array is 12.8 mm long, the instrument has a wavelength range of 400 nm. To extend the tuneable wavelength range of the instrument, the grating was mounted on a rotating micrometer driven stage. By mounting the stage on the bottom, outside the spectrograph, light leakage is eliminated. The precision micrometer allows for precise and reproducible rotations of the grating. With this configuration, the instrument can cover any 400 nm window from 200-1200 nm.

The spectrograph contains an integral faceplate with an overlapping edge. This faceplate was ringed by set screws which lock into a matching bevel on the Tracor Northern PDA detector head. By making the opening in the spectrograph recessed, and just large enough to accommodate the front of the PDA, an overlap was achieved to give a light tight seal.

The spectrograph also contains two openings for purge gas. The inlet is at the bottom, while the outlet is at the top of the box. Dry N_2 is usually the usual purge gas. Being heavier than air, it fills the spectrograph from the bottom. The lighter moist air is displaced out the top. The whole assembly is bolted to an aluminum block, which in turn is bolted to a stand which has a dovetail that fits an optical rail. Grating alignment and other internal adjustments are made through the top. The lid was machined oversize and cut with a recessed groove to keep the dark from leaking out. The inside (exclusive of the optical elements of course) was painted with ultra flat black paint to absorb stray light.

REFERENCES:

1. *TN-6100 Series DARSS Detector Head Manual,* Technical Manual PCN-278, Tracor Northern Inc., Middleton, WI. 53562 (1983).

2. *Characteristics and Applications of Microchannel Plates*, Technical Manual RES-0795, Hamamatsu Corporation, Middlesex, NJ., 08846 (1984).

3. *TN-6100 Series DARSS Detector Head Manual,* Technical Manual PCN-278, Tracor Northern Inc., Middleton, WI., 53562 (1983).

4. *S-Series Solid State Line Scanners,* EG & G Reticon Corp., Sunnyvale, CA., 94066 (1976).

5. P.J. Aiello, Masters Dissertation, Michigan State University, East Lansing, MI., (1982).

6. K. Oba et al; *IEEE Trans. on Nucl. Sci.*, Vol NS-26, (1979).

CHAPTER 4

SYSTEM SOFTWARE

Introduction

Today most people conceive of the data station as the instrument itself. There is judgment bias of an instruments "quality" based on their perception of the control software that interfaces the actual instrument to the user. Research and development efforts spent on software will bear a higher yield on investments than efforts in any other area. In Universities, it is difficult to justify time and effort directed towards software development. To compete even marginally with the functionality offered by commercial instruments would be impractical. Industry can bring greater resources, in terms of man years of programming, on product development. The ease of software development and the degree of system customization possible made FORTH a reasonable choice. The early version of FORTH available to this project was lacking in certain features considered essential today. Provisions were lacking for any type of graphics support, such as plotting pixels, drawing lines, or even printing text on our HERCULES video card. An inordinate amount of time was spent writing code to fill these voids; this makes for very boring reading, but nonetheless was a cornerstone of the project. These drivers will not be discussed in this thesis as their context would be better presented in an article on DOS device drivers.

System Memory Map

Figure 4-1 shows a memory map for the PC based, FORTH driven, diode array data station. The low portion of memory consists of DOS and BIOS system variables. The first 1024 bytes are occupied by the pointers to the 256 hardware and software interrupt vectors. Other system variables kept in low memory are various addresses of devices

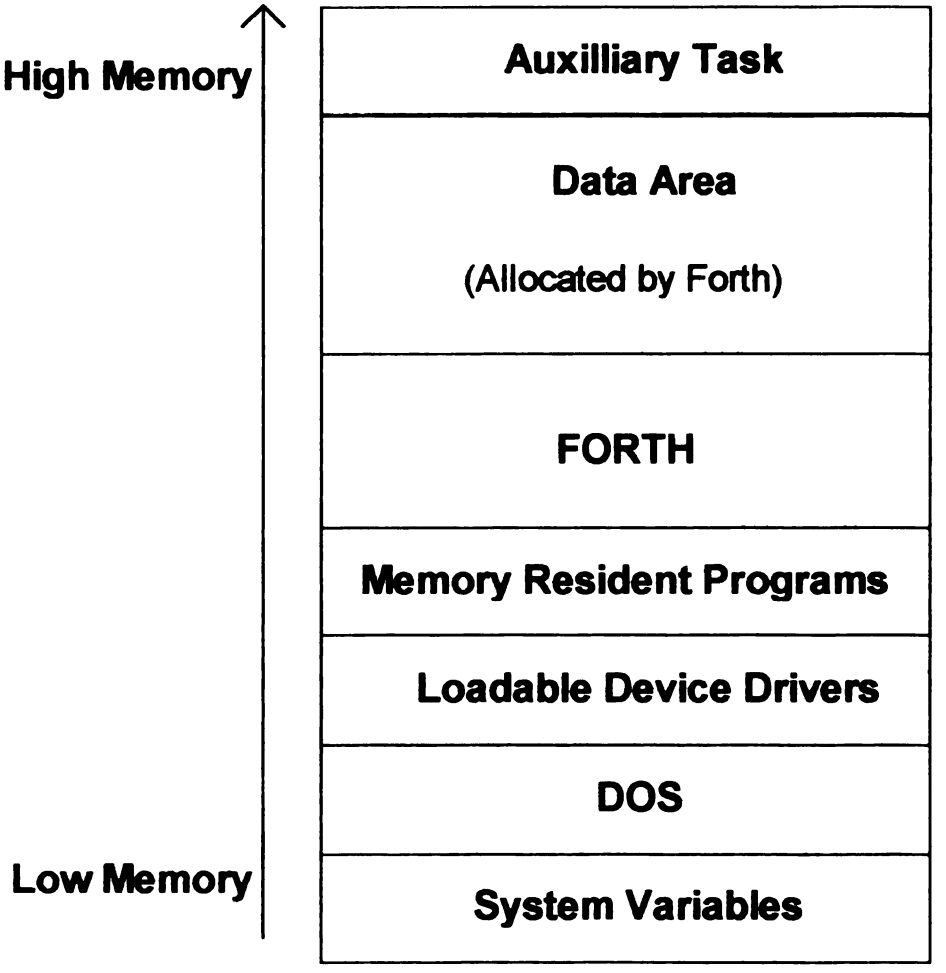

Figure 4-1

System Memory Map

located at power up time by the BIOS. These include the number of serial and parallel ports along with their addressed, types and capacities of disk and diskette drive(s), total system memory, type ahead keyboard buffer, and various flags indicating the presence of math co-processors, as well as the instantaneous state of the operating system.

Immediately above these vectors, DOS loads itself and allocates whatever memory it needs for disk buffers, file handle's, and user installable device drivers. DOS itself consists of user callable routines for handling everything from screen I/O, keyboard handlers, serial and parallel ports, file creation, file reads, file write, file and disk status, and memory allocations. Also included as a part of DOS is a program called the command processor, known as COMMAND.COM. When running, this program produces the familiar prompt C:> which is displayed on the screen.

Installable device drivers are loaded above DOS. These files are listed in the "CONFIG.SYS" file which DOS reads to load the appropriate files. DOS also creates any additional file buffers requested in this memory space. Loaded next are those memory resident programs usually placed in a batch file. This software is usually activated by an unusual keystroke sequence, whereby it intercepts the sequence, becomes active, performs its task, and terminates but stays memory resident. These can include everything and anything from phone dialers, pop-up calculators, spelling checkers, keyboard enhancers, alarm clocks, appointment scheduling, and the like.

Above the memory resident software lives FORTH. FORTH is actually a program that runs continually and could be thought of as being permanently memory resident. The difference is that after FORTH is invoked, all future communication with the system goes through FORTH. The normal DOS prompt is replaced by the FORTH prompt, which is usually an "ok". Keyboard and disk I/O pass through FORTH and are subject to interpretation by FORTH. Normal DOS operations still exist if FORTH is programmed to

interpret the instructions to their DOS equivalents. Thereby, DIRectories can still be displayed, files can be TYPEd, and subdirectories can be made, removed, or changed.

As mentioned earlier the diode array data acquisition is DMA driven. Properly initialized, the DMA controller transfers data at speeds adequate for the diode array time scale. If allowed to run amuck, the DMA controller will dump diode array data at random locations in the PC's memory space. Aside from making data retrieval difficult, software loaded previously in memory will not run properly if random sections of its code are replaced by raw spectral data. Although is would appear that the space above the FORTH partition is "free", this is not the case. DOS keeps tabs on unused memory blocks, such that when a properly behaved program requires more memory, DOS can find, allocate, and deallocate memory dynamically as needed. When FORTH is loaded by DOS, FORTH informs DOS of its disk size as well as its minimum and maximum memory requirements. Should FORTH or any other program running require additional memory, DOS uses memory control blocks (MCB) to chain through free memory to find a block large enough to meet the request. Simply using what is perceived to be "unused" memory will cause DOS to halt the system with a "memory allocation error" message. Most DOS functions are called by loading the AH register of the 80x8x processor with the DOS function call and invoking software interrupt 21 hex (Figure 4-2).

Functions 48H Allocated Memory

On Entry	Register Contents
AH	48H
BX	The number of paragraphs of memory requested

On Return	Register Contents
AH:0	Points to the allocate memory block
AX	Error codes; If carry flag is set
BX	size of the largest block of memory available (in para); if the allocation fails

Function 49H Free Allocated Memory

On Entry	Register Contents
AH	49H
ES	the segment of the block to be returned

On Return	Register Contents
AX	Error codes; if carry flag set

Function 4AH Modify Allocated Memory Blocks

On Entry	Register Contents
AH	4AH
ES	The segment of the returned memory block
BX	Contains the new requested block size in paragraphs

On Return	Register Contents
AX	Error codes; if carry set None; if carry not set
BX	Maximum poolsize possible if the call fails on a grow memory block request, if carry flag is set
BX	Size of the largest block of memory available (in para); if the allocation fails

Figure 4-2

DOS Memory Management Services

During initialization, high level FORTH uses the interrupts shown in Figure 4-2 to locate the top of its (FORTH's) memory space, and allocate sufficient free memory. The amount of memory FORTH requires is specified by the variable MAX#-SCANS. This is usually made large enough to accommodate 100 scans (≅ 200 Kbytes). The DOS routines that are called to allocate memory expect paragraphs as variables. Paragraphs are 16 bit pointers to 16 byte blocks of memory. The entire 1024 Kbyte PC address space consist of 65,536 paragraphs and can be addressed by a single 16 bit register. The FORTH variable FIRST-DATA contains the starting paragraph number of the data area allocated by DOS at FORTH'S request.

The "meat" of the software control is in the interrupt routine. As explained earlier, this routine is called at the completion of each scan which is initiated by the START pulse. The Interrupt Service Routine (ISR), can modify subsequent scans based on a pre-determined set of operator selected parameters contained in a parameter table. Prior to the start of a scan the operator builds this table with menu driven software. A typical set of parameters

Diode Array Scan Parameters

Entry Number	Number of Iterations	Integration Time (ms)	Take Data ? (Y or N)	Last Scan ? (Y or N)
1	1	3.5	n	n
2	1	10.5	n	n
3	50	10.5	Y	n
4				Y

Figure 4-3

Diode Array System Parameters Setup Menu

as entered into the menu would appear as shown in Figure 4-3.

In the sample menu depicted, entry 1 causes the array to perform a scan in 3.5 ms without collecting data. This is routinely done to replenish the charge on the individual diodes. By not taking data, this assures that valuable RAM is not occupied by invalid data. The next entry informs the system to acquire 50 scans of 10.5 ms duration and to store the data in memory. The last entry informs the software that the last scan has been performed and the system should become "idle".

Each entry in the menu corresponds to eight consecutive bytes in a binary parameter table. This table is examined by the ISR at the end of each scan to determine how to prepare the system for the next scan. The FORTH variable TBL_START points to the beginning of the binary parameter table, while the variable TBL_OFFSET points to the offset in the binary parameter table of the currently executing parameters. A list of the eight bytes that comprises each table entry and their contents is shown in Table 4-1.

The table entry at byte 1 is expected to contain either a 1, or 2. If the first byte entry contains a 1 then this entry is not the entry for the last scan and the routine should get the next eight bytes for processing. If the entry contains a 2 then this is the last scan and the routine should shut down the array and send it into idle mode.

Table 4-1

Eight Byte Binary Parameter Table Contents	
byte 0 Collect Data? 1=True, 0=False	byte 1 Last Scan? 0, 1, 2 or 3
byte 2 Integration Time MSB	byte 3 Integration Time LSB
byte 4 Iteration Count MSB	byte 5 Iteration Count LSB

Interrupt Service Routine

What follows is the complete commented code of the ISR. The code is broken into small sections of functional modules. These sections will be discussed individually along with any special caveats or precautions. The code is written in FORTH's native assembly language. The syntax is similar to INTEL standard syntax with the exception being the "verb" follows the operands and the verb is punctuated by a period. The FORTH assembly language statement:

```
TBL_OFFSET +[ ]          AX                MOV.
```

has the effect of moving the contents of the FORTH variable TBL_OFFSET into the AX register. A complete list of 8088 mnemonics can be found in the iAPX 88 book [1].

```
CODE INT_2
                         CLI.              \
AX                       PUSH.             \Save everything we think we need
BX                       PUSH.             \
DX                       PUSH.             \
DS                       PUSH.             \
AX  CS: DATA_SEG +[ ]    MOV.              \ Start of data segment
DS  AX                   MOV.              \
AL  MODE-FLAG +[ ]       MOV.              \ Get the mode flag
AL                       DEC.              \ Is mode flag = 1 ? ( menu mode)
JZ                       MENU-MODE.        \ Run array in mode 1
JMP                      START-PULSE.      \ Any other value causes a dummy fire
```

The preceding code saves the contents of those registers it will use. Because the ISR can be called from anywhere in memory it must be called by a far call. A far call consist of a 16 bit pointer to a 64 kilobyte memory block (paragraph) and a 16 bit offset into the 64 kilobyte block. Segmented addressing limits the 8088 to only addressing 64 kbytes of code and 64 kbytes of data at a time. In order for the ISR to access high level FORTH's

variables, both the ISR and FORTH must have the same value in the Data Segment (DS) register. After assuring that DS is properly initialized, the ISR has access to FORTH's variables. It then checks the FORTH variable MODE_FLAG for a 1. If it finds a 1, the ISR will retrieve further instructions from the binary parameter table built by the menu software, otherwise it will just issue a START pulse without having initialized the DMA controller. This will initiate a dummy scan without collecting any data. The MODE_FLAG is used to keep the system from accessing the binary parameter table when the menu software is being used to modify the table.

```
>>>>>>MENU-MODE.                              \
CNTR +[ ] WORD-PTR      DEC.                  \ Has counter reached 0 ?if so must
                                              \ get another set of parameters
JS                      MORE-PARAM.           \ Go get some more parameters
AX  1D IW               MOV.                  \ Delay for timing loop
CALL                    DELAY1.               \ Kill time so both paths are same
JMP                     DO-DMA?.              \ Present set of parameters good, test
                                              \ flag and dec memory if necessary
                                              \ then go start the array
                                              \
```

Each eight byte entry in the binary parameter table referring to a scan has an associated iteration count (Table 4-1). This is done so that when 50 identical scans are required they can be accomplished with only one table entry. The ISR keeps track of what iteration it is presently performing in the FORTH variable CNTR. As seen in the following code fragment, each pass through the routine will DECrement the iteration counter CNTR. The routine will then JS (Jump on Sign bit being set), if and when the CNTR drops below zero, thereby forcing the code to fetch the next set of parameters on the next iteration.

```
>>>>>> MORE-PARAM.                           \ Need another set of parameters
BX TBL_OFFSET +[ ]      MOV.                  \ Get pointer to current table offset
                                              \ Must init
                                              \ TBL_OFFSET = TBL_START
```

```
DX CS: [BX]          MOV.          \ If high byte is = 1 then last scan
                                   \ If low byte is = 1 then enable dma
DH                   DEC.          \ Is this the last scan, dh <<>>1 ?
JZ                   CONT.         \ DH = 1 not last scan, process it
DH                   DEC.          \ Is DH = 2, last scan ?
JMP                  CLEANUP.      \ Last scan go to dummy scan mode
```

Having ascertained the need for fresh parameters, the routine loads BX with the current offset into the binary parameter table. Using BX in indirect addressing mode ([BX]), the ISR starts to process the eight byte group of parameters from the table. High level FORTH primes the routine at initialization to start at the beginning of the table at by setting the TBL_OFFSET = TBL_START, and setting the CNTR = 0. This forces the routine to start reading the table at the beginning on the first pass through the ISR. The ISR also determines at this stage if the last entry in the table is being processed and if the array should be shut down at this point.

```
>>>>>> CONT.                       \ Not last scan, get parameters
DMA-FLAG +[ ] DL     MOV.          \ Set dma flag
BX 02 IW             ADD.          \ Point to next word in data set
DX 31D IW            MOV.          \ Point to counter 1 " STB "
AX CS: [BX]          MOV.          \ This word contains the time in ms
AL                   OUT-DX.       \ Send lsb first
AL AH                MOV.          \ Get second byte
AL                   OUT-DX.       \ Send it along also
```

The first word (2 bytes), of the parameter table were read into the DX register. The high byte (DH) contains the "last scan" flag, while the low byte (DL) contains the DMA_FLAG. This flag is examined later to determine if the DMA controller is to be enabled or not. The pointer to TBL_OFFSET is incremented by two. This points it to bytes 2 and 3, which contains the integration time of this scan. These values are used to update the appropriate 8254 counter.

```
BX 02 IW                ADD.        \ Point to next word in data set
AX CS: [BX]             MOV.        \ Get iteration count
BX 04 IW                ADD.        \ Point to next word in data set
TBL_OFFSET +[ ] BX      MOV.        \ Save the pointer into param table
AX                      DEC.        \ Decrement counter because we will
                                    \ execute on iteration
CNTR +[ ] AX            MOV.        \ Put count in variable
JMP                     DO-DMA?.    \ Must inform system of memory use
                                    \ then fire the array, reset 8259 and
                                    \ return
```

Using the same method of advancing the pointer used earlier, we point to and retrieve the next word of the eight byte set that contains the iteration count. This is saved in the variable CNTR. We then add 4 more to the TBL_OFFSET pointer. This is necessary because the table contains 2 entries that are not currently used and they must be jumped over so that TBL_OFFSET points to the start of the next group of eight bytes. The code then jumps unconditionally to determine if the 8237 DMA controller is to be enabled.

```
>>>>>> CLEANUP.                    \ Set the system to dummy scan mode
MODE-FLAG +[ ] 04 IB    MOV.        \ Set mode to dummy scan
\AL 05IB                MOV.        \ Mask off 8237 channel 3
\AL 0A                  OUT.        \ Send it and return
AX DUMMY-SPEED +[ ]     MOV.        \ This word contains the time in ms
AL                      OUT-DX.     \ Send lsb first
AL AH                   MOV.        \ Get second byte
AL                      OUT-DX.     \ Send it along also
```

This code shuts down the array by setting the variable MODE_FLAG to a value other than 1. This will cause the ISR to just issue a START pulse without initializing the 8237-5 DMA controller. The counter is slowed down so that the array idles by scanning itself at a speed kept in variable DUMMY_SPEED. This is done so that the "idling" array doesn't bog down the PC's performance with frequent interrupts. The DMA controller is disabled by masking off the DMA channel servicing the diode array.

```
\ enabled. This will leave the array in a ready to be fired state when
\ the parameter table is finished. The array is left dummy scanning by
\ virtue of the mode flag.  To re-execute the parameter table just set
\ MODE-FLAG = 1 to re-execute a virgin table
\
CYCLE# +[ ] FFFF IW          MOV.              \ " Zero " cycle counter
                                               \ Reset FSET
AX FSET-ORIG +[ ]            MOV.              \ Original value
FSET +[ ] AX                 MOV.              \ Restored
AX SCANS-TILL-EMPTY-ORIG +[ ]    MOV.          \ Reset SCANS-TILL-EMPTY
SCANS-TILL-EMPTY +[ ] AX         MOV.          \
AX DMA-PAGE-ORIG +[ ]            MOV.          \ Reset DMA-PAGE
DMA-PAGE +[ ] AX             MOV.              \
DMA-FLAG+[ ] 01 IB           MOV.              \ Set the data request flag
CNTR +[ ] 00 IW              MOV.              \ Zero counter
DMA-FLAG +[ ] 00 IW          MOV.              \ Zero this flag for the fun of it
AX TBL_START +[ ]            MOV.              \ Beginning of parameter table
TBL_OFFSET +[ ]AX            MOV.              \ point to start of parameter table
                                               \ Fire the array and exit
```

The remainder of this routine initializes some variables to the values they had before the first iteration of the ISR. This will prepare the array for retriggering from the start of the binary parameter table. Because the variable MODE_FLAG $\neq$ 1, the array will be in the scanning idle mode.

The variables that are reinitialized and their meanings are:

CYCLE#

This contains the number of scans actually acquired in memory by DMA intervention. It is used by the ISR to keep dynamic track of available memory consumption as well as a count of the number of scans saved.

FSET_ORIG

The DMA controller can only access 64 Kbytes (16 bits), and uses a page register to generate the high 4 bits to produce a 20 bit address (Figure 4-4). These 64 Kbyte DMA boundaries occur regularly. However the memory allocation services will find and allocate memory based on paragraph units. When the memory allocation services return the starting paragraph of the requested memory block, the chances are more than likely the returned paragraph will not start at the beginning of DMA page boundary. In the example shown in Figure 4-4, the high hex digit is the current page. This is loaded into the variable DMA_PAGE_ORIG. The offset into the page is formed by the low 3 hex digits with a zero follower. To initialize the DMA controller to point to the starting paragraph 73A4H, the DMA page register is loaded with a 7, while the DMA address register is loaded with 3A40H. In practical operation of the array, the variable FSET_ORIG is rounded up to the nearest even multiple of 400H (1024). This is because a 512 element diode array requires 1 Kbyte to hold one scan from a 12 bit A/D. The rounding assures the next time the DMA page register is adjusted the base address will start at zero. The current software pre-computes the value of FSET_ORIG. This is done because FSET_ORIG is a constant until the PC is rebooted and it's computation within the ISR routine would add unnecessary overhead.

FSET

As the variable FSET_ORIG is the original offset into the first DMA page. The variable FSET is the dynamic version of the offset the ISR uses to keep track of where to program the DMA controller to store the next scan. After the ISR services a scan that acquires data, the variable FSET is incremented by a precalculated value equal to the number of BYTES_PER_SCAN.

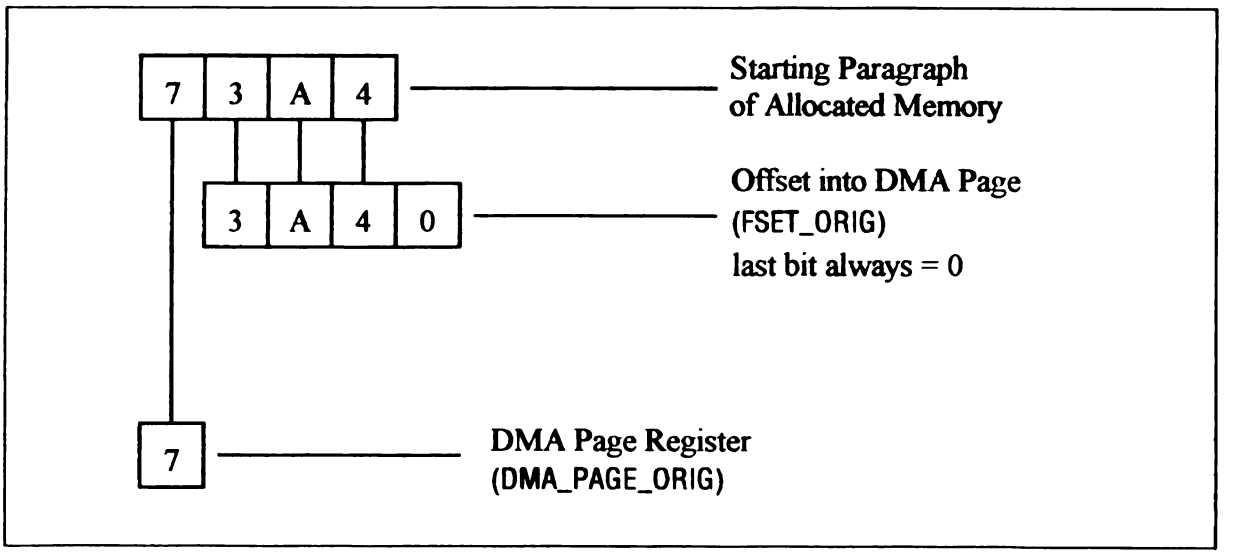

Figure 4-4

DMA Page and Offset Addressing from Paragraphs

SCANS_TILL_EMPTY_ORIG

This is the precomputed value of the number of scans the first short DMA page will hold. It is a constant until the PC is rebooted and the configuration changes such that the location of the top of free memory is different.

SCANS_TILL_EMPTY

This is the count of the number of scans that will fit in the current DMA page. The ISR decrements this value whenever a scan is stored. It uses this value to determine when to adjust the DMA page register. Prior to the start of any scans FORTH sets SCANS_TILL_EMPTY = SCANS_TILL_EMPTY_ORIG. Whenever data are acquired in memory, this value is decremented. When the DMA page register is adjusted, the ISR sets SCANS_TILL_EMPTY = 64, which is the number of scans a whole page can store.

DMA_PAGE_ORIG

This precomputed value is likewise constant until the PC's memory configuration is changed after rebooting. It is the value of the original DMA page, computed as shown in Figure 4-4.

DMA_PAGE

This is the dynamic counterpart to the variable DMA_PAGE_ORIG. The ISR dynamically alters this variable as the array is running to keep track of the present location of the current DMA page. This variable is a convenience and is not really necessary as the actual hardware DMA page registers can be read as well as written.

DMA_FLAG

This variable is used by the ISR to determine if the 8237-5 DMA controller should be programmed and unmasked to allow data acquisition.

CNTR

The ISR uses this variable to keep track of how many iterations it has executed of a menu entry. All menu entry's are executed at least once, but when multiple passes through the same entry are required this variable is decremented dynamically by the ISR through each pass.

```
>>>>>> START-PULSE.                    \
DX 307 IW              MOV.            \ Point to 8255 control port
AL AL                  SUB.            \ Set bit c0 low
AL                     OUT-DX.         \ Send it
AL                     INC.            \ Set 8255 port C bit 6 hi
```

```
AL                      OUT-DX.         \ Send this also
AL 20 IB                MOV.            \ Non specific eoi
AL 20                   OUT.            \ Send it to the 8259 command reg
DS                      POP.            \ Restore everything we used
DX                      POP.
BX                      POP.
AX                      POP.
                        IRET.           \ Return from interrupt
```

The preceding section of code starts the hardware necessary for a scan by issuing a "request to start" pulse through the 8255 Peripheral Input Output (PIO) chip (11). An End Of Interrupt (EOI) is issued to the 8259 programmable interrupt controller and all altered registers are restored. The routine returns control to whatever it interrupted by executing an Interrupt RETurn (IRET) instruction.

```
\ We have to indicate we are using memory, must program 8237, decrement
\ memory allocation table, check to see if we cross a page boundary
\
>> DO-DMA?.
DMA-FLAG +[ ] 01 IB     CMP.            \ Are dma request being serviced ?
JNE                     FIRE-ARRAY.     \ No, just fire array and exit
```

The preceding code segment determines if data are to be acquired or not. On the basis of the status of the DMA_FLAG the routine will either program the 8237-5 DMA controller or just send a start pulse.

```
\ Otherwise we must indicate memory is being used and program the 8237,
\ page registers and update FSET, SCANS-TILL-EMPTY, CYCLE#
\
AX CYCLE# +[ ]          MOV.            \ Get count of cycle executed
AX                      INC.            \ Bump value by one
AX MAX#-SCANS +[ ]      CMP.            \ Have we hit top of memory yet ?
JL                      MEMORY-GOOD.    \ Memory is still good, continue
JMP                     CLEANUP.        \ Ran out of memory, shut down array
```

To reach this point the system wants to store data into memory. For safety the ISR compares the dynamic variable CYCLE#, which contains a count of the number of scans already stored in memory, with MAX#_SCANS, a precomputed constant containing the maximum number of scans we have asked to be allocated.

```
>>>>>> MEMORY-GOOD.
CYCLE# +[ ] AX              MOV.          \ Restore updated cycle count
SCANS-TILL-EMPTY +[ ]       BYTE-PTR DEC. \ Decrement counter,
                                          \ we're using memory
JNS PAGE-OK.                              \ Still have room, memory is ok
AX MAX-SCANS-PAGE +[ ]      MOV.          \ Reload the memory counter with
SCANS-TILL-EMPTY +[ ] AX    MOV.          \ the max number of scans per page
AL DMA-PAGE +[ ]            MOV.          \ Get the current dma page value
AL                          INC.          \ Increment the value
AL 082                      OUT.          \ Output 8237 channel 3 page register
DMA-PAGE +[ ] AL            MOV.          \ Update page counter variable
FSET +[ ] 00 IW             MOV.          \ Zero the offset, starting new page
```

Dynamic variables are informed of our intention to use memory. The variable CYCLE# is incremented to indicate another "live" scan, and SCANS_TILL_EMPTY is decremented to indicate a loss from the available size of the current DMA page. A check is made to see if the current DMA page has been depleted. If it has been depleted the variable DMA_PAGE is incremented, the DMA page hardware register is updated and the offset (FSET), into the new page is zeroed. The variable SCANS_TILL_EMPTY is updated with the precomputed constant MAX_SCANS_PAGE.

```
\ We now have to set up the 8237 address and count register and unmask
\ the 8237 to allow dma request to occur.
\
>>>>>> PAGE-OK.                          \
AX FSET +[ ]                MOV.          \ Get the current offset
AL 0C                       OUT.          \ Dummy write, set 8237 flip bit
DX 06 IW                    MOV.          \ Point to 8237 address register
```

```
AL                      OUT-DX.         \ Output lsb first
AL AH                   XCHG.           \ Swap bytes
AL                      OUT-DX.         \ Send msb to address register
AL AH                   XCHG.           \ Restore original count word order
BX BYTES/SCAN +[ ]      MOV.            \ Get number of bytes per scan
AX BX                   ADD.            \ Add number of bytes per scan
FSET +[ ] AX            MOV.            \ Save value in offset variable
AX BX                   MOV.            \ Get byte count to AX again from BX
AX                      DEC.            \ Decrement because 8237
                                        \ adds one to count
DX                      INC.            \ Point to 8237 count register
AL                      OUT-DX.         \ Send lsb of count
AL AH                   XCHG.           \ Swap lsb and msb
AL                      OUT-DX.         \ Send msb of count
AL 03IB                 MOV.            \ Setup to unmask 8237 channel 3
AL 0A                   OUT.            \ Unmask it
>>>>>> FIRE-ARRAY.                      \ Start the array
DX 307 IW               MOV.            \ Point to 8255 control port
AL AL                   SUB.            \ Set bit c0 low
AL                      OUT-DX.         \ Send it
AL                      INC.            \ Set 8255 port C bit 6 hi
AL                      OUT-DX.         \ Send this also
\
>>>>>> GO-HOME.                         \ Reset interrupt controller
AL 20 IB                MOV.            \ Non specific eoi
AL 20                   OUT.            \ Send it to the 8259 command reg
DS                      POP.            \ Restore everything we used
DX                      POP.            \
BX                      POP.            \
AX                      POP.            \
                        IRET.           \ Return from interrupt
END-CODE
```

The rather large segment of code above is entered when the ISR determines the current DMA page has enough room to contain another scan. This code segment performs the

mundane task of using the current offset into the current valid DMA page (FSET), to point the 8237-5 DMA controllers address registers to the next valid free memory address. The DMA controller is programmed to transfer the value contained in the variable BYTES/SCAN, which is usually 1024 bytes. The 8237-5 DMA controller is unmasked, and the array fired by issuing a request to generate the START signal. This precipitates the hardware events that actually initiate the true hardware START signal (Figure 3-5). The routine exits from where it came as described earlier.

The diode array source code in its entirety would occupy 100+ printed pages and thus is not presented. The bulk of the code is contained in 7 files with the code grouped logically. A master file called **LOADEM**. contains these files by name. They are listed in the order they should be loaded. FORTH builds the diode array system when the command Memory File LOAD "MFLOAD **LOADEM**", is issued to FORTH. FORTH loads the files into memory, and interprets/compiles them in less than a minute. The particular implementation of FORTH uses a turbo type interpreter and has a throughput of roughly 6,000 lines per minute on the current 5 MHz PC.

FORTH as an Operating System/Language

The system software was written in FORTH. This aided in making the instrument user friendly due to its English-like syntax. FORTH is hierarchical. Its structure is composed of "words". A word is the smallest unit of written code useful in the FORTH programming environment. Words are composed of other words and so on. Written correctly FORTH is readable and intuitive to a human operator. FORTH presents itself to an uninitiated observer as an english sentence with atypical punctuation. A small example of code is shown below.

```
: Take_Data    Get_User_Parameters    Initialize_Array    Wait_For_Go_Signal
  Plot_Data    Reset_Array ;
```

FORTH requires a leading semi-colon to signal the start of a new "word". In this case the word's name is "Take_Data". The succeeding words are all words that FORTH would know for one of several reasons. The first reason is that they are core words required as part of the language. The second being that they are user-defined words, that are words comprised of earlier definitions. Typing the word "Take_Data" at the terminal followed by a carriage return would cause all of its defining words to execute. This allows incremental program development and debugging because each word can written, tested, and optimized before including it in the vocabulary of the FORTH language. Words pass numbers, pointers to arrays and strings, and pointers to other words via a common stack. A requisite component of a standard FORTH implementation is the inclusion of an in-line assembler for the host CPU. The use of an in line assembler makes the interface between FORTH and assembly language painless. FORTH is relatively quick in its performance, with speeds between that of compiled BASIC and C. FORTH tends to produce the smallest code of any language (even assembly language). This made it ideal in the days of 64 Kb microcomputers when memory resources were scarce.

The FORTH language is rich in its basic compliment of conditional tests, loops, complicated data structures, and core words. However to maximize the utility of an extensible language the operator must be able to extend the vocabulary in a useful way. This means that there will be as many different extensions of FORTH as there are FORTH programmers. A word with high mnemonic content for one programmer would probably be implemented differently by another programmer. Perhaps even differently by the same programmer on a different day. In the FORTH example "Take_Data" shown earlier, the definition might be remembered more readily as "Get_Data", or "Fetch_Data". FORTH's parser is very unforgiving of "accents" or synonyms when being addressed. In some

respects FORTH is quite primitive. It has a limited capacity for the features that are taken for granted in other programming languages.

FORTH doesn't deal well with floating point numbers and has a non standard file structure. FORTH is not very portable across different systems because of its extendibility and its lack of a standard file structure. However, in spite of these shortcomings, FORTH is unequaled for programming control micros. There is no need for compilation and linking as with other languages. Code development time is reduced due to the interactive nature of debugging and the readability of the language. A programmer need only know that the word "Initialize_Array" will do just that when executed, no knowledge of the words inner mechanism is necessary.

FORTH Program Files

RASTER

The first file to be loaded is called RASTER., the contents of which are mostly in assembly language. At the time of the instrument's inception the only affordable graphics board with acceptable resolution was manufactured by Hercules. This board is not supported in our implementation of FORTH, and drivers were needed to draw points, lines, and text while in graphics mode. Provisions also had to be made for resetting the board in and out of graphics mode. The assembly language code contained in RASTER performed these tasks. Some important words and their expected parameters are:

HPOINT (x y color -)

HPOINT expects three items on the top of stack (tos), the lowest (first) item on the stack is the x coordinate, next is the y coordinate, finally is the color. A zero for color will cause erasure of the current x,y coordinates. Any other value for color will plot the point. The coordinate 0,0 is at the lower left hand corner. This routine is written in assembly language for speed.

LINE. (x1, y1, x2, y2, color -)

LINE expects the FORTH stack to contain the five parameters X1, Y1, X2, Y2, and COLOR to be passed with the coordinates of the endpoints of the line. LINE uses the same coordinate system and interpretation of the color variable as hpoint-stack. It is coded in assembly language for speed.

H-LINER. (-)

H-LINER expects the user defined FORTH variables to contain X1, Y1, X2, Y2, and COLOR to be initialized with the coordinates of the endpoints of the line. H-LINER uses the same coordinate system and interpretation of the color variable as hpoint-stack. It is coded in assembly language for speed.

HIRES (-)

HIRES sends the Hercules board into high resolution (720 x 348) graphics mode and clears the graphics screen. This word also revectors the word FORTH uses to print to the screen to another routine contained in raster. This routine called "HERC-EMIT" prints characters by printing them dot by dot.

ALPHA (-)

This word returns the Hercules card into text only mode. The FORTH print routine is re-vectored to its point of origin.

INTX

The file INTX. contains the body of the interrupt service routine (ISR) discussed earlier. The majority of the FORTH variables are declared in this routine, as well as the remainder of the code written in assembly language. The space for the binary parameter table is allotted as well.

WITHIN (n1 n2 n3 - f)

WITHIN returns a true flag (flag $\neq$ 0) if n2 << n1 << n3. This is coded in assembly language for speed.

ON-DEMAND-BUILD (-)

This word loads the binary parameter table with a special set of constant values to operate in a mode called "SCAN-ON-DEMAND-MODE".

ON-DEMAND-TIME! (time -)

This sets the data collection time (in ms) when the array is operated in the "SCAN-ON-DEMAND-MODE".

ON-DEMAND-TIME@ (- time)

This word returns the current integration time when the array is operating in "SCAN-ON-DEMAND-MODE".

BYTES-PER-SCAN (-)

BYTES-PER-SCAN calculates the number of bytes a single scan will occupy and saves the answer in the FORTH variable BYTES/SCAN. Also the number of paragraphs per scan is calculated and stored in the variable PARA/SCAN.

SCANS-TO-EMPTY (-)

SCANS-TO-EMPTY calculates the number of scans the first short DMA page will hold and stores it in the FORTH variables SCANS-TILL-EMPTY and SCANS-TILL-EMPTY-ORIG.

SCANS-PER-PAGE (-)

This word calculates the number of scans a full DMA page will contain. The value is stored in the FORTH variable MAX-SCANS-PAGE.

DMA-PAGE-SET (-)

This word uses the value of the FORTH variable BLOCK-START, which contains the segment of the start of the allotted data area, to calculate the initial value of the DMA page register. This values is stored in the FORTH variables DMA-PAGE-ORIG and DMA-PAGE.

INT-7-OFF (-), INT-7-ON (-)

These words are complimentary and as can be implied by their names will either mask or unmask interrupt 7 on the 8259-A programmable interrupt controller.

DMA-3-OFF (-), DMA-3-ON (-)

These words will toggle the mask bit on the 8237-5 DMA controller, thus enabling or disabling the interface board from collecting data.

In addition the file INTX. contains words for setting the mode of operation for the 8255 PIO chip, the 8259 interrupt controller, the 8237 DMA controller, and programming the modes and speeds of the 6 counters contained on the 8254-2 counter-timer chips.

MN

The next file loaded is called MN. This file contains words for manipulating the cursor through a text based menu. The contents of this user created menu are used to build the binary parameter table. The ISR uses this table to dynamically alter the operating parameters during the course of a sequence of scans. The only FORTH definition of any consequence is "MENU". This word clears the screen and presents a reverse video cursor that points to various cells of a menu (Figure 4-5). The cursors' movements are controlled by the arrow keys on the numeric keypad. When parameters are typed followed by a carriage return <<CR>>, they appear in the cell where the cursor presently resides. As parameters are entered into the menu, the binary parameter table is simultaneously updated with the user selected variables. The software will not permit a table entry that is out of range or in an invalid format. The number of iteration column entry must be at least 1 and the minimum integration time is 4.5 ms. The columns labeled "Take Data", and "Last Scan" will accept either a "Y" or "N" in their fields. The active function keys are their purpose is listed on the bottom of the screen. Key F1 will save the current parameter

Sample Menu Screen Output

Entry Number	Number of Iterations	Integration Time (ms)	Take Data? (Y or N)	Last Scan? (Y or N)
1	1	4.5	n	n
2	3	10.5	n	n
3	50	10.5	n	n
4			Y	Y

1:Save 2:Get 3:-F 4:+F 5:Regen ESC:Exit PgUp PgDn

Figure 4-5

Sample Menu Screen Output

set and prompt for a filename. Key F2 will retrieve a binary parameter set saved earlier. Key F3 will scroll the menu up one line with key F4 performing the opposite action. The keypad keys PgUp and PdDn scroll the menu 10 lines at a time. The binary parameter allots room for 50 entries, which in practice is 45 more entries than is really needed. The escape key exits the menu function while clearing the screen.

HLOAD

The next file is called HLOAD, its code supports the array when it is operated in the "SCAN-ON-DEMAND-MODE". This mode of operation is the most interactive and consistent with the behavior the majority of people expect from a diode array. In this mode the array executes a fixed binary parameter table that clears out the array and takes a single scan at a user selected integration time.

In "SCAN-ON-DEMAND-MODE", the ISR is designed to ignore execution of the bulk of its code. It does not execute the binary parameter table and wont collect data if the MODE-FLAG $\neq$ 1. The array executes the binary parameter table and performs a scan-on-demand by when the MODE-FLAG = 1. After the completion of the scan, the ISR shuts the array down by setting the MODE-FLAG = 4 just before it returns. The acquired scan can be displayed interactively on the screen and another scan acquired by resetting the MODE-FLAG = 1. The integration time can be altered between scans and the results viewed almost instantly. Operating the system interactively permits fine tuning of experimental parameters such as array gain, integration time, lamp intensity, monochromator settings, and array observation wavelength settings. A constant or slowly varying signal can be observed at the convenience of the operator.

HAXIS

The last major file loaded is called HAXIS. This file has the job of installing the code segment and offset of the ISR in the interrupt vector table in low memory. This file also defines five of the six major words required to operate the array.

MEM-TO-DISK (n1 n2 -)

Assuming the array has completed multiple scans this word will save them to disk after prompting the operator for a filename. Scans n2 through n1 inclusive will be saved to disk. Parameter n1 represents the last scan to save while n2 is the first scan. No check is made for sufficient disk space to hold the scans and no errors are returned if a write should fail for any reason.

DISK-TO-MEM (n1 n2 -)

This word is complimentary to MEM-TO-DISK, and as its name implies will take data from the disk and write it to memory. This is useful if it is desirable to use the data station's software in reviewing the results of a scan taken earlier. It expects two parameters on the stack and will write scans n2 through n1 inclusive into memory.

V-DIAGS (n1 -)

V-DIAGS expects a single number on the top of the stack. This number is the last scan number in memory the operator wishes to review. The screen goes into graphics mode as shown in (Figure 4-8).

V-RUN (-)

This word causes the array to run in "SCAN-ON-DEMAND" mode. No parameters are expected or values returned.

Array Operating Modes

V-DIAGS Scan Replay Mode

Operation in V-DIAGS mode will cause the PC to sequentially display scans from memory to the screen. The scans will be displayed starting with scan zero up to scan n1, where n1 is the number left on the stack when the FORTH word V-DIAGS is executed. Scans are redrawn as the previous scans are erased. This animates the output to reflect changes in experimental conditions in real time. Time compression is useful for post postmortem monitoring of extremely rapid or very slow events, redisplaying them on a time frame suitable for visual study. When the last scan in the sequence (n1) is displayed, the cycle restarts automatically with scan zero. Besides the spectral data the screen displays the current delay (Figure 4-6), which is an iteration counter in a dummy loop that is executed prior to the screen drawing a single pixel. The y-axis scale units are A/D counts, with a range from 0-4095. The limits of the y-axis can be repeatedly halved by multiple presses of function key F2, or doubled by pressing function key F1 (Attenuation control, Figure 4-6). The arbitrary delay between redraws can be incremented or decremented by the actions of function keys F3 and F4 respectively (Figure 4-6). The scan number currently being displayed on the screen is also shown and updated automatically. Function key F7 causes the PC to immediately add 10 to the scan being displayed and plot that scan, while key F8 will decrease the number of the next scan to be displayed. Function key F5 will cause the system to restart the display sequence at zero. Key F10 is a toggle and will make the system calculate and display the intensity either in counts, %T, or absorbance units. The legend and limits of the y-axis will change in accordance with the mode being displayed. Function key F9 changes the function key legend on the bottom of the screen and draws a vertical line on the output screen. As can be deduced from the legend on the bottom of the screen (Figure 4-7), the function keys will change the location

of the vertical line (locator) in increments of ± 100, 10, or 1 array element. The length of the x-axis is 510 screen pixels, one for each diode array element.

Repositioning the locator gives the operator a mean of dynamically querying the system for an individual element's intensity history during the course of a pre-recorded scan. Function key F9 toggles the screen to its previous mode. Pressing the escape key while in either mode returns control of the PC to the FORTH operating system.

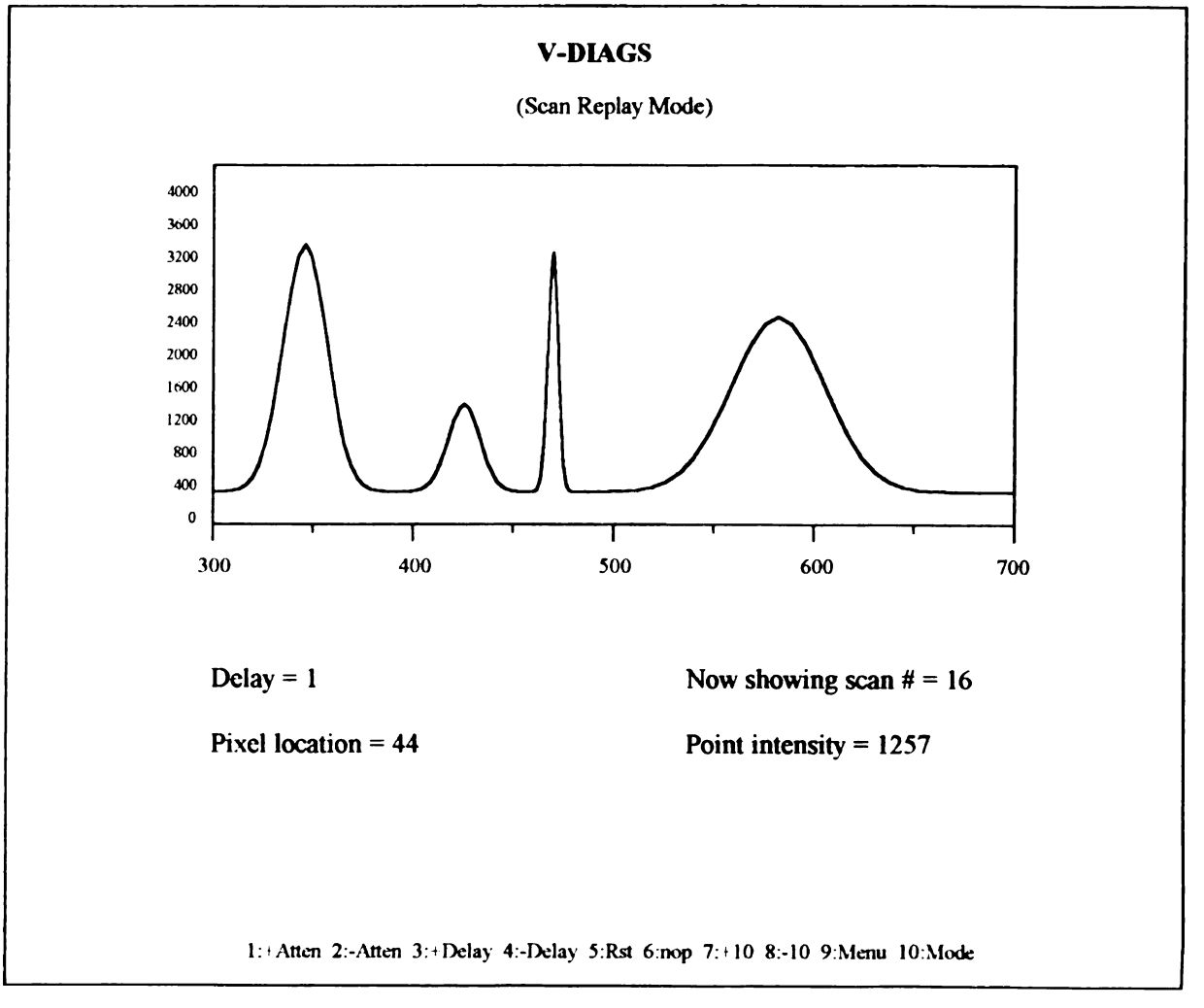

Figure 4-6

V-DIAGS

(Scan Replay Mode)

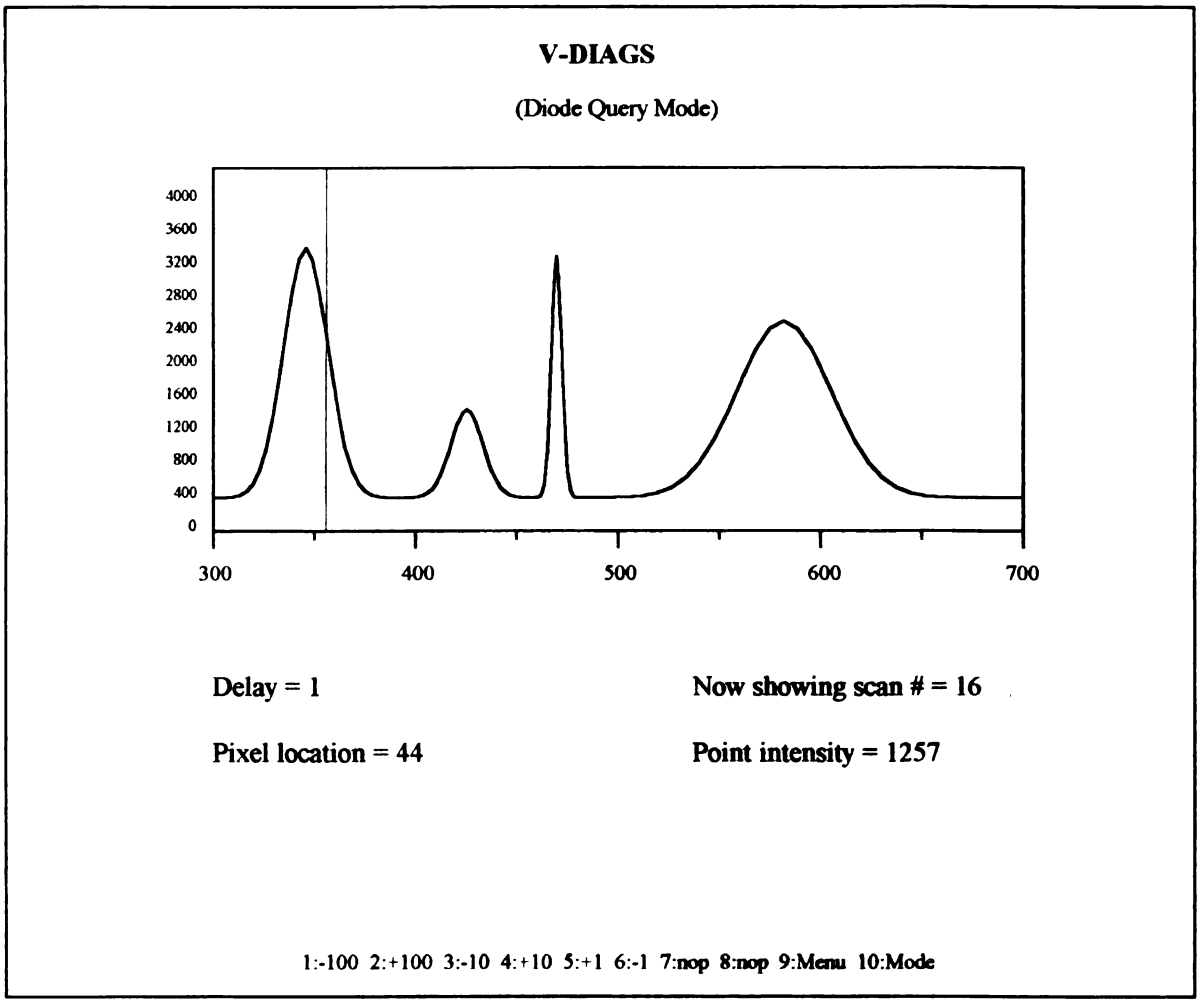

Figure 4-7

V-DIAGS

(Diode Query Selection Mode)

V-RUN Scan-on-Demand Mode

When operated in the Scan-On-Demand mode, the array repeatedly acquires a single scan and plots the results as illustrated in Figure 4-8. Because all scans occupy the same memory location the array can operate in this mode indefinitely without consuming memory resources. This mode is useful when adjusting experimental parameters to optimize the signal within the optimal operating parameters of the array. The consequences of adjustments to lamps, optical elements, and alignment can be observed

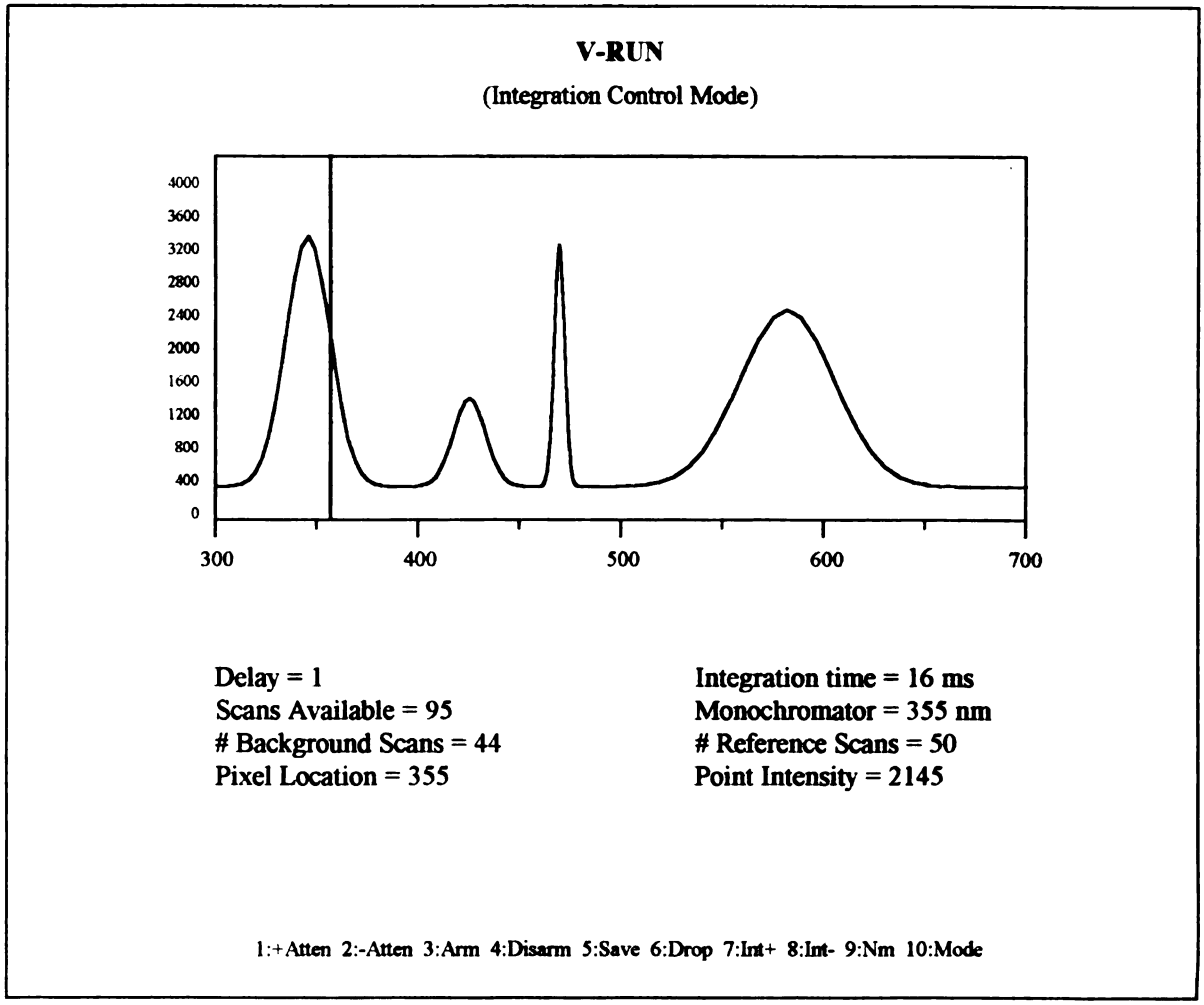

Figure 4-8

V-DIAGS

(Integration Control Mode)

immediately. Repeatedly pressing function key F9 will cause the mode of operation of the remaining function keys to be altered through four separate menus. These modes of operation described briefly are the integration setting mode, the pixel interrogation mode, the reference/background accumulation mode, and the monochromator control mode.

Integration Mode Screen

The integration control mode, shown in Figure 4-8, permits real time observation of the effect of changing the integration time on the output signal. Function keys F1 and F2 adjust the attenuation for the digital display and have no effect on the analog signal. Function key F5 will save a snapshot of the currently displayed scan in memory and decrement the "Scans Available" display on the screen to reflect the number of scans that system can accumulate. Function key F6 drops scans out of memory on a first-in-first-out (FIFO) basis. The "Scans Available" counter is similarly adjusted to reflect freeing memory resources. Function key F10 controls the display mode for the y-axis of the graph. It will toggle between counts, absorbance units, and percent transmittance, assuming reference and background scans have been accumulated. The label on the y-axis will change to indicate the current display mode.

Function keys F3 and F4 perform simple but useful tasks. Key F3 sets a software flag, while key F4 clears it. Although not immediately apparent, this task is quite useful. To understand why, a brief explanation of the code that comprises V-RUN is in order.

Figure 4-9 shows the actual code of V-RUN. The first lines of code initialize some variables, the graphics screens, and the hardware that controls the array and acquires data.

```
: V-RUN

SETIT       PREPARE-ON-DEMAND   ARM-ARRAY              SINGLE
00          DISPLAY-NOW    !    00    END-SCAN         !
WAIT-A-WEE-BIT
HIRES       PAGEH       LOGO        (Graphics mode, clear hercules page)
00    S->P  00    400   40    FILL  (Zero data buffers)
V-RUN-LEGENDS
[']   KEY-DO-A          KEY-DO                 !
[']   DISPLAYA          DISPLAY-IS             !
[']   DUMMY-MODE        PROCEED?               !
[']   0-PUT             OPERATOR-ROUTINE1      !
[']   NEXT              OPERATOR-ROUTINE2      !
[']   STATUS-A          STATUS?                !
      ARM-ARRAY         VIEW-ON-DEMAND         ;
```

Figure 4-9

Source code for FORTH Word V-RUN

The line of code:

```
['] KEY-DO-A KEY-DO!
```

takes the code field address (CFA) of the FORTH word KEY-DO-A and stores it in the FORTH variable KEY-DO. The remaining lines of code perform identical functions for the FORTH words and variables shown. The FORTH code sequence

```
KEY-DO @EXECUTE
```

will retrieve the address of the FORTH word stored at the FORTH variable KEY-DO and execute the FORTH word. When the function key F9, which changes the mode of operation of the function keys, is pressed, it simply cycles one of four values through the FORTH variable KEY-DO. This indirect execution changes the behavior of the function keys simply and with minimal code overhead. The last FORTH word in the definition of V-RUN is VIEW-ON-DEMAND. This FORTH word executes an endless loop that does nothing but indirectly execute the code contained in the FORTH variables KEY-DO. This code defines the behavior of the function keys, DISPLAY-IS, which defines the mode of display of the intensity along the y-axis. The variable PROCEED? contains the address of the word that defines how the display buffer is filled, either by retrieving one from memory or taking a new scan. The FORTH variable OPERATOR-ROUTINE1 contains code that is executed just prior to a scan being taken. In this case it just leaves the number on the top of the stack of the next scan to be displayed. The variable STATUS? contains the address of the code that defines how the array and function keys status are to be displayed. Finally the variable OPERATOR-ROUTINE2 contains the address of the FORTH word NEXT. This word just tells FORTH to proceed with the next word in the sequence. The FORTH compiler appends this code onto all defined words.

However in the case of the diode array acquiring synchronous fluorescence, the CFA of the word NEXT in the variable OPERATOR-ROUTINE2 is replaced by an operator defined word that waits for a flag to be set by an ARM command, initiated by function key F3, then performs the synchronous scan as it was programmed.

By allowing the user to specify code to be executed at the end of a single scan gives the array unlimited versatility to acquire, analyze, and make decisions and adjustment during the course of and experiment via user supplied logic.

Diode Query Mode

The pixel interrogation mode, shown in Figure 4-10, uses function keys F1, F3, and F5 to move a bar across the graph in either 100, 10, and 1 pixel increments. As the bar moves, the display is updated to reflect the present array location and the intensity at that location. Function keys F2, F4, and F6 decrement the locator position by 100, 10, and 1 pixel increments respectively. Function key F9 reprograms the function keys to operate in the reference/background mode.

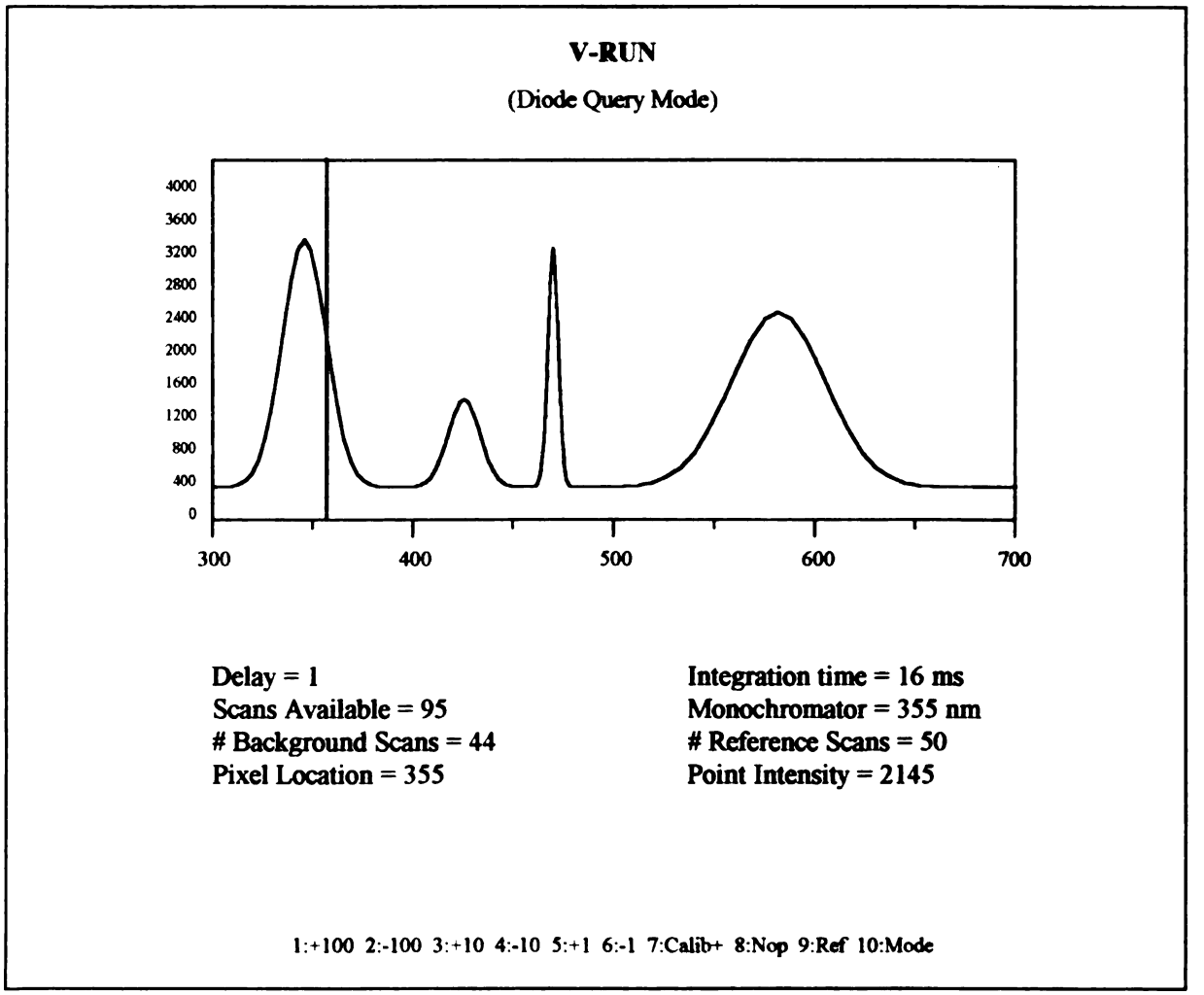

Figure 4-10

V-RUN

(Diode Query Mode)

Reference/Background Mode

In reference/background mode, shown in Figure 4-11, a running average is kept of accumulated reference and background scans which are required for ratio measurements. Function keys F1, F2, and F3 acquire and average 100, 10, and 1 reference scans, while F5, F6, and F7 perform the same functions for background scans. Function keys F4 and F8 will zero out the reference and background buffers respectively. Function key F9 reprograms the function keys to operate in the pixel interrogation mode.

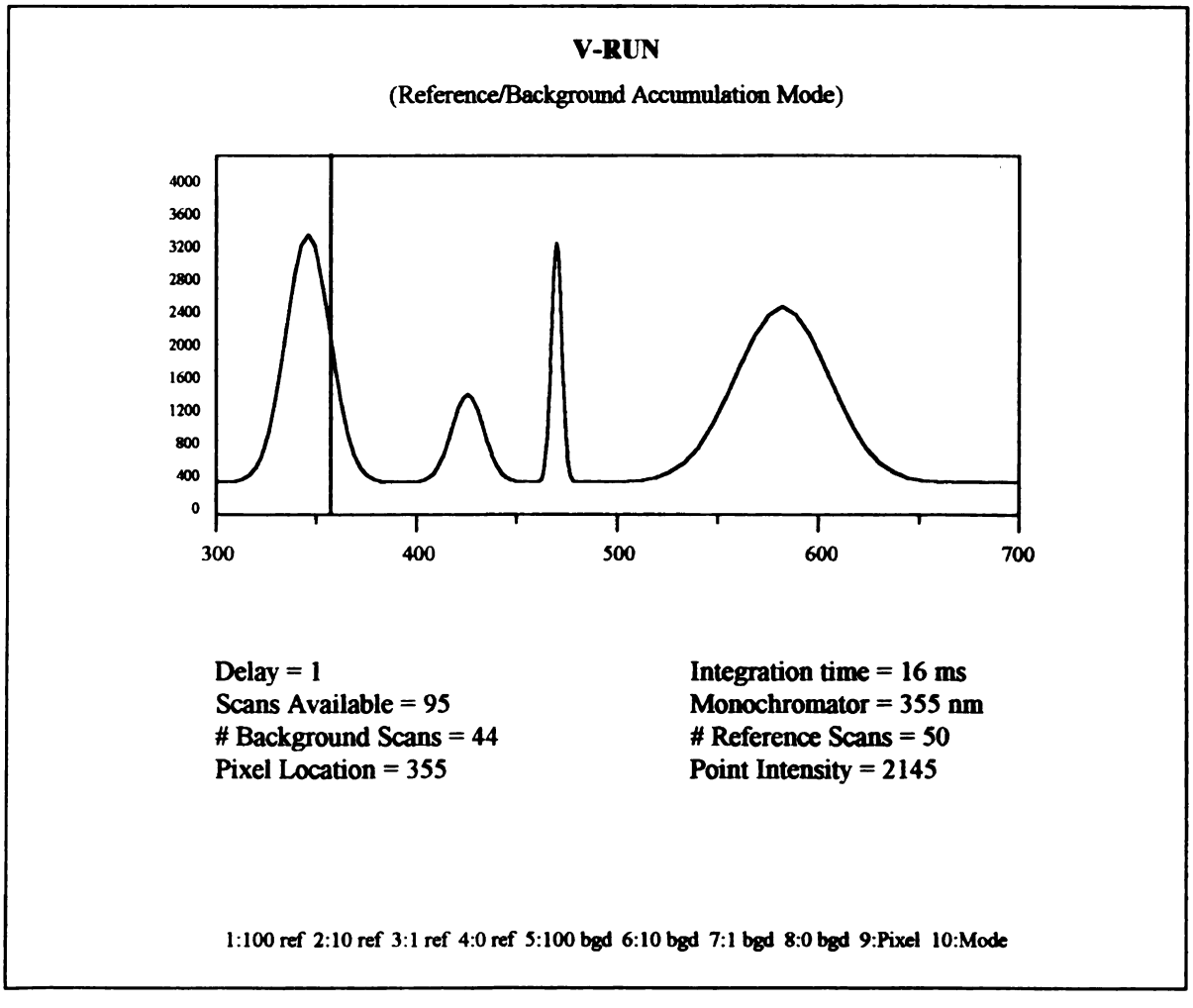

Figure 4-11

V-RUN

(Reference/Background Accumulation Mode)

Monochromator Control Mode

The monochromator control screen, shown in Figure 4-12, was specialized to support the control of the excitation monochromator when using the system to acquire synchronous fluorescence data. Function keys F1, F3, and F5 advance the monochromator setting by 100, 10, and 1 nm, while F2, F4, and F6 decrement the monochromator settings by like amounts. Function key F7 causes the stepper motor to recalibrate. Function key F8 causes the stepper motor to move the monochromator to the new setting. Key F9 reprograms the function keys to operate in the reference/background acquisition mode.

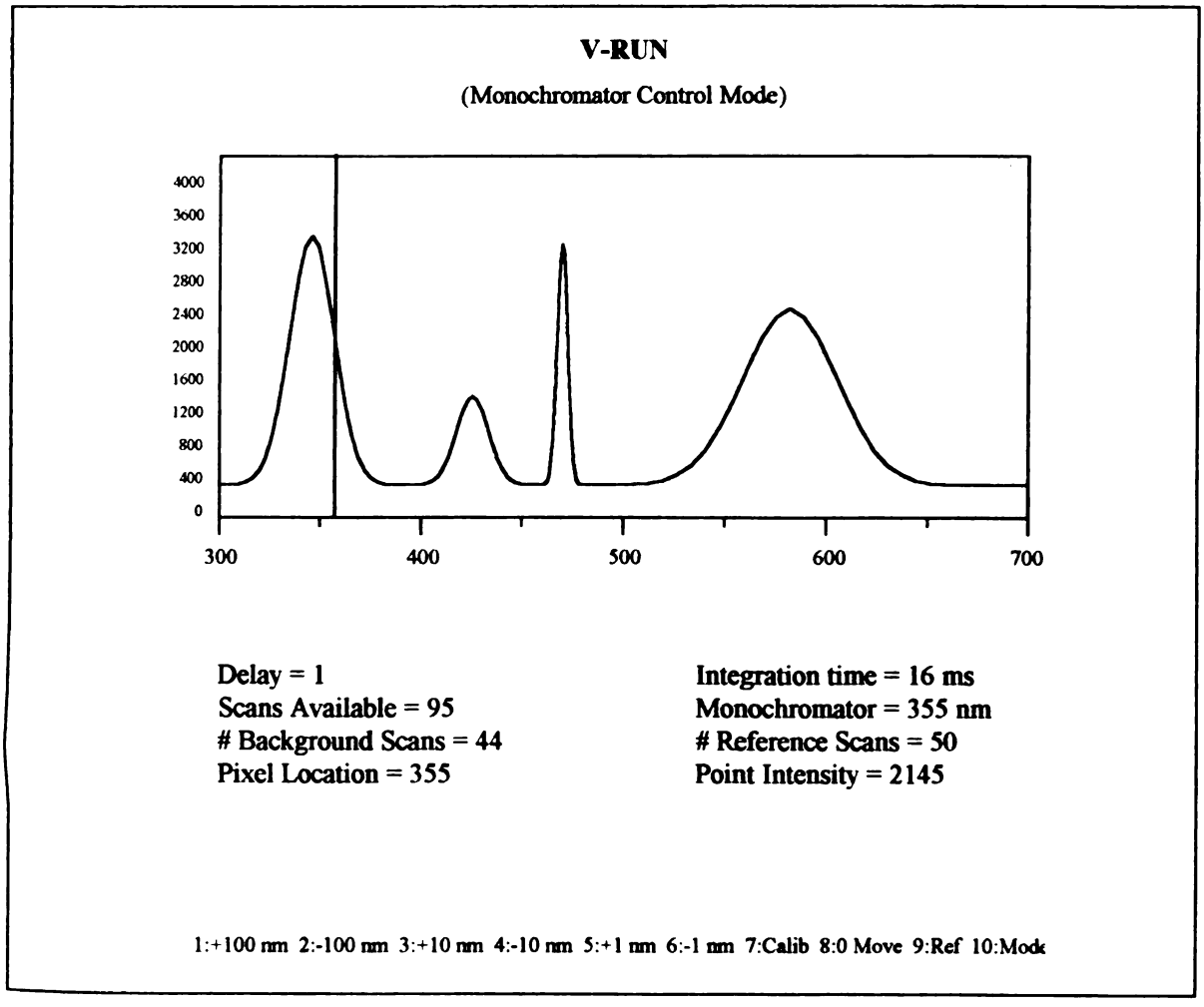

Figure 4-12

V-RUN

(Monochromator Control Mode)

REFERENCE:

1. Microprocessor and Peripheral Handbook, Intel Corporation, Santa Clara, CA. 95051 (1988).

CHAPTER 5

CHARACTERIZATION OF THE INTENSIFIED DIODE ARRAY SPECTROPHOTOMETER

Introduction

The previous chapters have described why the instrument was built, how it works, and its operation. This chapter deals with the instrument's performance, reproducibility, and S/N characteristics. The influence of various fixed and adjustable parameters on array performance are also discussed.

Signal-to-Noise Ratio

The photometric measurement precision of a UV-visible spectrophotometer is limited by several sources of uncertainty inherent in the instrument [1]. In an intensified PDA detector, noise originates from several sources. These noise sources manifest themselves as preamplifier noise, A/D converter noise, dark current shot noise, photon shot noise, and photon flicker noise. Other unrelated sources include variations in solution refractive indices due to thermal and concentration gradients, imperfections in sample cells, and aberrations due to system optics as well as long term drift in sources and electronics.

Assuming precautions have been taken to reduce contributions from the unrelated noise sources, the total noise (σ_T) for a PDA system comes from 3 sources. These noise sources are due to the readout process (σ_r), dark signal noise (σ_d), and photon shot noise (σ_λ). Quantization noise from the A/D converter is less than ±½ count. The total noise (σ_T) is given by the following expression $\left(\sigma_T = \sqrt{\sigma_\lambda^2 + \sigma_d^2 + \sigma_r^2}\right)$. Ideally, the performance of a PMT based spectrophotometer is photon shot noise limited. The

PDAspectrophotometer is preamplifier noise limited (σ_r) (Table 5-1). Therefore, the S/N increases almost linearly with the signal intensity. It is thus preferable to maintain the integrated signal intensity near the maximum A/D count level (4096 counts). The signal is maintained near the maximum A/D count not by increasing source intensity or slit width, as is done in PMT based systems, but rather by increasing the integration time. Adjustments in intensity levels often lead to undesirable shifts in the noise characteristics of the instrument, usually from photon shot noise limited to flicker noise limited. Similarly, drifts associated with a thermostated PDA have been observed to be rather low [2 , 3], and become significant only when a large number of readouts are averaged in memory instead of on the detector. This phenomenon is thought to be associated with the flicker noise in the MOS-FET multiplex switches of the PDA [4].

Table 5-1 [4]

Theoretical Noise Considerations for the Intensified Diode Array Detector

Signal (counts)	σ_r (counts rms)[a]	σ_λ (counts rms)[b]	σ_d (counts rms)[c]	σ_T (counts rms)[c]	$\frac{S}{N}$
10	3	0.09	1.6	1.0	4.3
100	3	0.29	1.6	1.9	50.6
1000	3	0.9	1.6	2.1	476
4000	3	1.8	1.6	2.6	1538
16000	3	3.7	1.6	4.2	3810

a. Readout noise is approximately ≈ 3 counts/millisecond, equivalent to approximately 1200 electrons rms.

b. $$\sigma_\lambda = \frac{\left[\text{signal (counts)} \times 1200\left(\frac{\text{electrons}}{\text{count}}\right)\right]^{1/2}}{1200\left(\frac{\text{electrons}}{\text{count}}\right)}$$

c. σ_d has been calculated based on the assumption that dark charge is 3000 counts/diode/16 sec integration

Dark Current

One operational characteristic of the PDA is the background noise associated with the dark current. This is the net signal in counts that is obtained when no light strikes the detector. As thermionic emission from the intensifier photocathode is a contributor to dark current, the net dark current signal per channel, in counts, is proportional to the integration time, the dark signal per channel per second, and the gain factor for the electronics. The dark signal per channel is temperature dependent, dropping by roughly 50% for every 7° C drop in temperature [5].

The dark current as a function of integration time is easily determined by blocking the entrance slit to the spectrograph and scanning the array at different integration times. As can be seen in Figure 5-1, the dark current is somewhat constant across the array. It was found not to vary linearly with the integration time (Figure 5-2). At roughly 1/4 of full scale, the dark current versus integration time relationship becomes non-linear. However, being reproducible from scan to scan, it can readily be subtracted out. At long integration times for low light levels, the dark current is usually what limits the dynamic range of the PDA.

At the lowest setting of the intensifier gain control (0.0), the dark current was the same as if the intensifier had been switched off. At the highest gain setting (10.0), the dark current increased by roughly 10% over the dark current measured with the intensifier switched off. The tendency for dark current to consume the dynamic range makes cooling the array a requirement for low light measurement at long integration times. As can be seen in Figure 5-2, cooling the array reduces the dark current sufficiently that it requires 10 seconds for the array to reach 25% saturation as opposed to 1 second at room temperature.

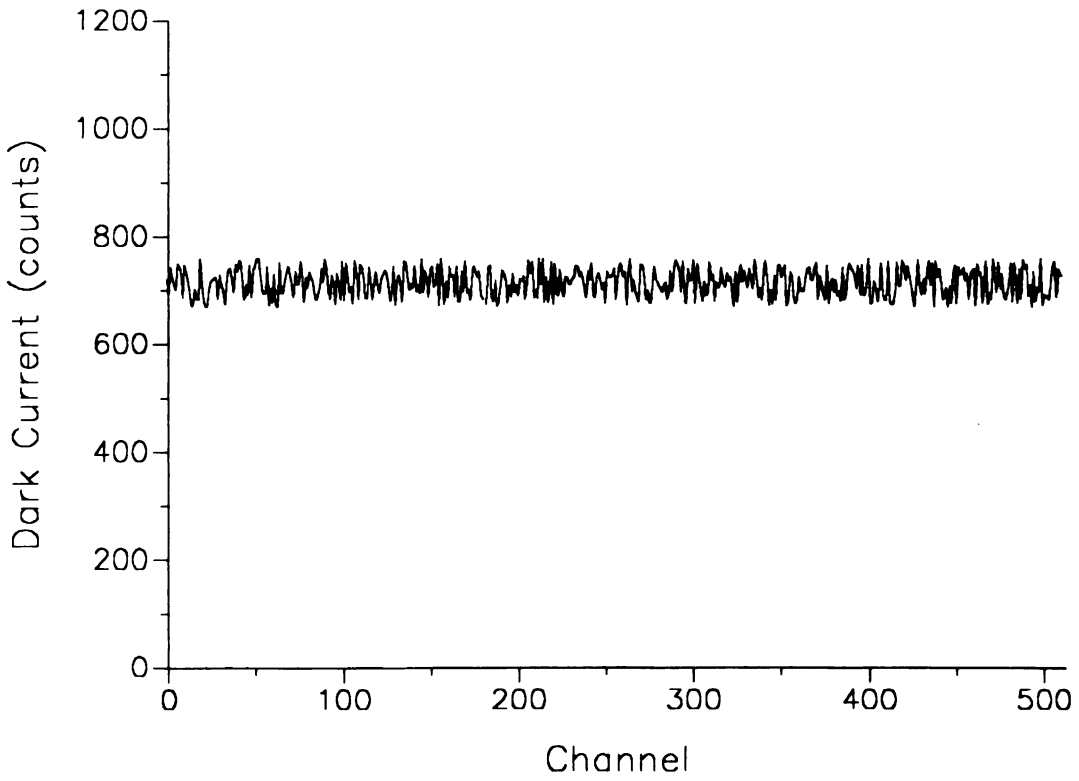

Figure 5-1

Intensified Diode Array Dark Noise

The dark noise is plotted against channel number in this figure. The gain setting was 2.5 with an integration time of 1 sec. The array was operated at room temperature. The noise is multiplied by 5 along the Y-axis.

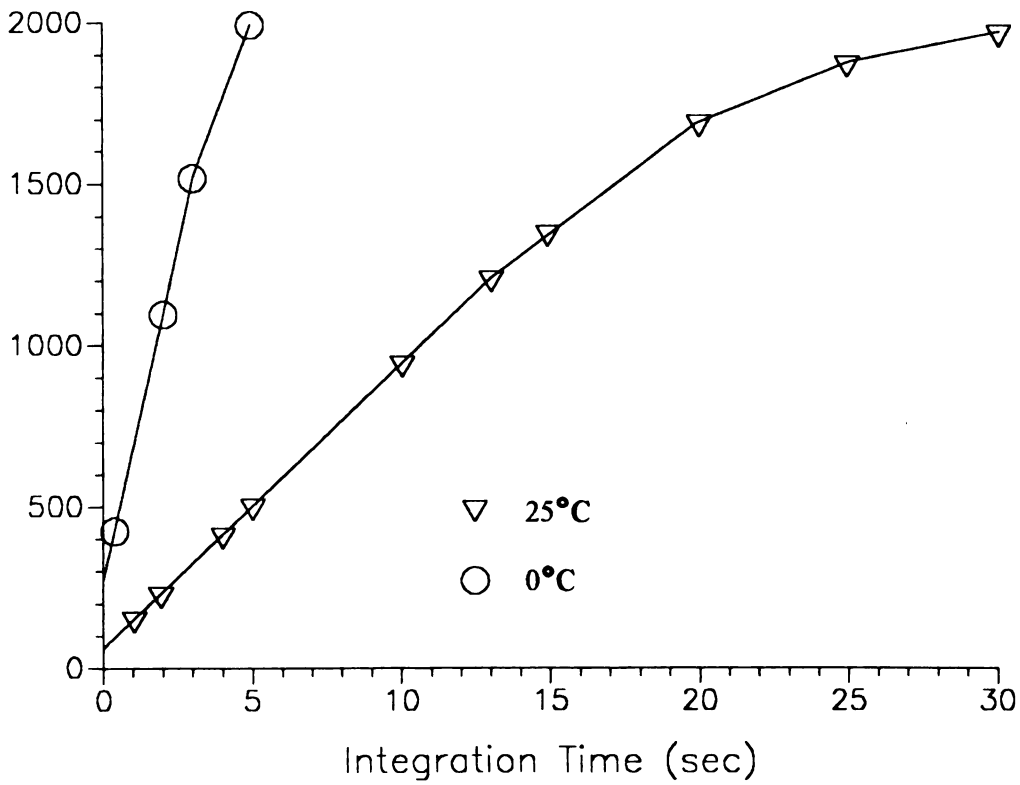

Figure 5-2

Dark Signal Dependence on Integration Time

Shown is the dark signal vs integration time. By using the Peltier cooler the dark current response is linear for integration times as long as 14 seconds. The readings were taken from a 10 diode bunch in the middle of the array. The gain setting was 2.5 for all measurements.

Integration Time Linearity

Integration is the technique where signal enhancement is achieved by taking advantage of the on-target, charge-integrating capabilities of the diode array. As the PDA is preamplifier noise limited, the S/N increases linearly with the integration time [4]. Therefore it is preferable to integrate on target for 1 second as opposed to digitally summing ten 100 ms scans in which 1/f readout noise is added. Photomultiplier-based spectrophotometers are often photon shot noise limited.

Figure 5-3 shows signal intensity plotted as a function of integration time. As is the case with dark current, the integration time-intensity response becomes decidedly non-linear at approximately 25% of full scale. However, the precision of 100 consecutive scans is >>1.8% (relative standard deviation) worst case among 300+ diodes. A General Electric #1974 quartz iodine lamp was used as the source. Only those diodes where the light level was at least 25% of full scale were used in the calculation. This lamp was chosen as a source over the xenon arc lamp because of its superior broadband stability.

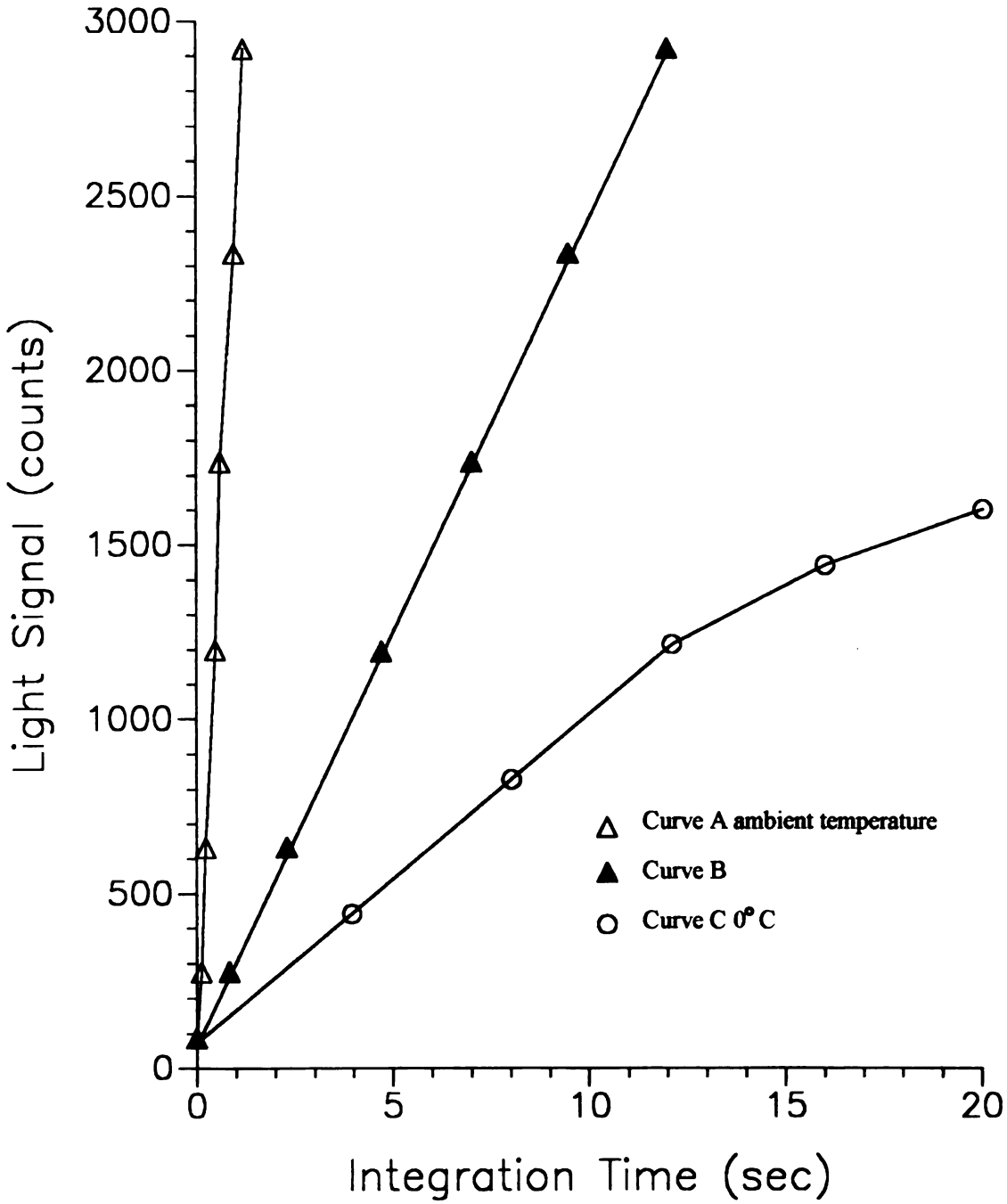

Figure 5-3

Signal vs Integration Time

Shown is the dependence of the net light signal vs the integration time. Curve A was obtained without cooling. Curve B is the same as curve A except the x-axis scale has been multiplied by 10. Curve C was obtained when the array was cooled to 0^{o} C. The light source was a 10 Watt quartz-iodine lamp. Calibrated neutral density filters were used to vary the light intensity. The intensifier setting was 2.0 for all measurements.

Varying the signal intensity with neutral density filters produced a linear response (<<1% RSD worst case), at constant integration time. The non-linear response observed earlier is due to the processes occurring in the PDA and is not dependent on the sampling method. Previously constructed instruments employed "auto-ranging" [6], a method whereby each diode was sampled at near saturation by repeatedly doubling the integration time and saving only those data points that did not overflow the A/D. By tracking the number of times a diode had been doubled, a high resolution (in intensity) scan could be reconstructed. When using such techniques, care must be taken to assure that intensity is linear with the integration time. As can be seen from Figure 5-3, the time range for which auto-ranging can be performed is greatly extended by cooling the array.

Stray Light

Stray light is often severe in the small spectrographs with fast gratings used with PDA's. Light scattering, fiber cross talk, and reflections of the excitation beam from the far end of our flow cell (typically 4% of the excitation beam), severely limit the instruments ability to record low light levels. The use of ultra flat black paint and internal baffling reduced the effect somewhat. However, stray light had a noticeable effect on the minimum detection limit. The effect can be seen empirically in the 3-dimensional plot of stilbene in Figure 5-4, where the small peak corresponds to the stray light due to scattering of the excitation beam and reflections in the sample cell.

Stray light was observed more quantitatively by observing the signal from the PDA with a He-Ne laser as the source (632.8 nm). The noticeable feature is the line at 452 nm is probably due to second order reflections within the spectrograph. The signal at 452 nm was determined to be 2.2% of the height of the signal at 632.8 nm (Figure 5-5). The measurements were made with the presence of two Kodak 2A cutoff filters. These filters transmit wavelengths from 400 to 800 nm. Two filters were used, one being placed inside

the spectrograph near the slits, while the second was placed outside, in the path of the He-Ne laser. The ratio of the peak at 632.8 nm to the peak at 452 nm remained constant, proving that the stray light originated entirely from within the spectrograph.

These experiments however do not characterize the stray light levels for the instrument. All we are measuring is the ability of the paint to absorb stray light from the 632.8 nm He-Ne laser line. There is also a possibility that the observed signal is due to atomic or ionic emission lines of the He-Ne laser. This seems unlikely, as the small peak does not remain at a fixed distance from the larger peak when the grating is rotated.

The fiber optic interface, although convenient for alignment purposes, plays havoc when trying to minimize stray light within the array. An iris was used in front of the lens while imaging the source on the slit. Usually this was just a piece of cardboard with a hole punched in the center. This limited the effective f/no of the lens to match that of the fiber. The *f*/no. of the fiber optic used in the interface is related to the numerical aperture by $f/\text{no.} = NA/(2 \times \tan \theta_0)$ [1]. Given that the effective numerical aperture of the fiber optics range from 0.25 - 0.35, depending on the wavelength and solvent refractive index, the f/no. of the fibers range from 2 - 3.5. A fiber optic limited interface tends to overfill the entrance slit and would be a cause of stray light

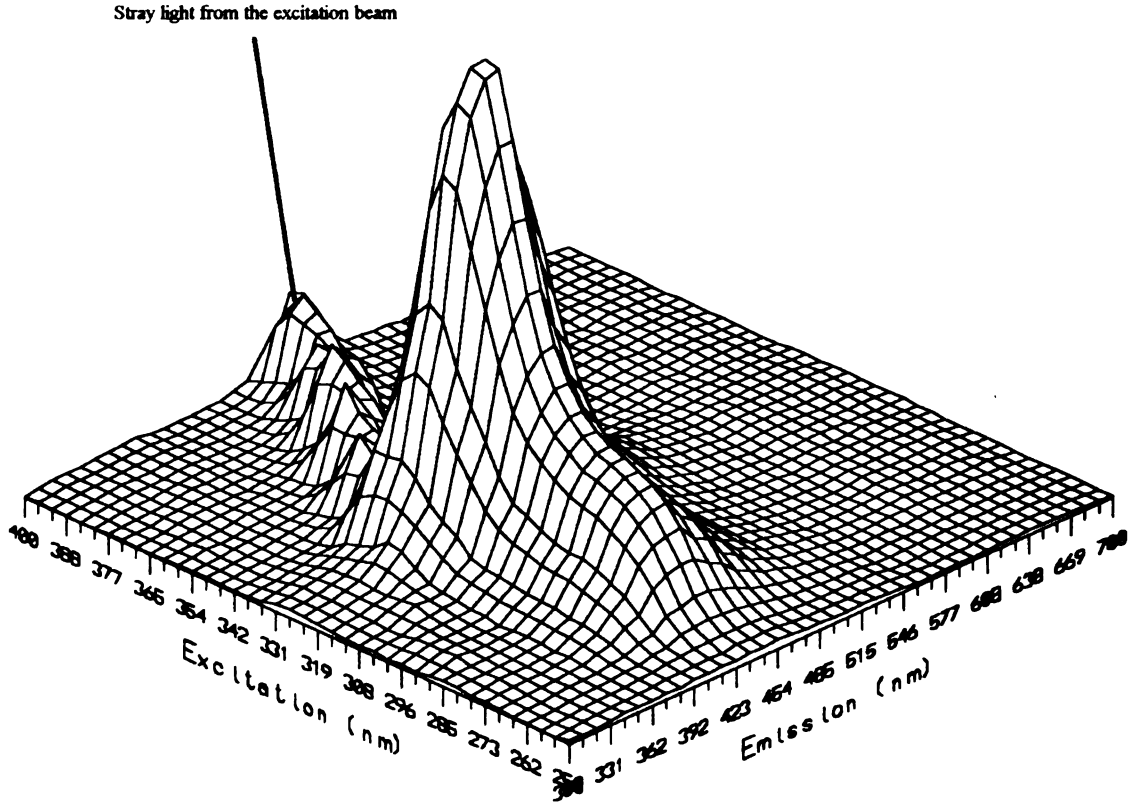

Figure 5-4

Stilbene

Excitation/Emission Spectra

The excitation/emission spectrum of stilbene shows a strong signal from the stray light inherent in the PDA spectrometer. The small fast monochromator and higher orders from the concave grating in the spectrometer give rise to a fairly large stray light signal.

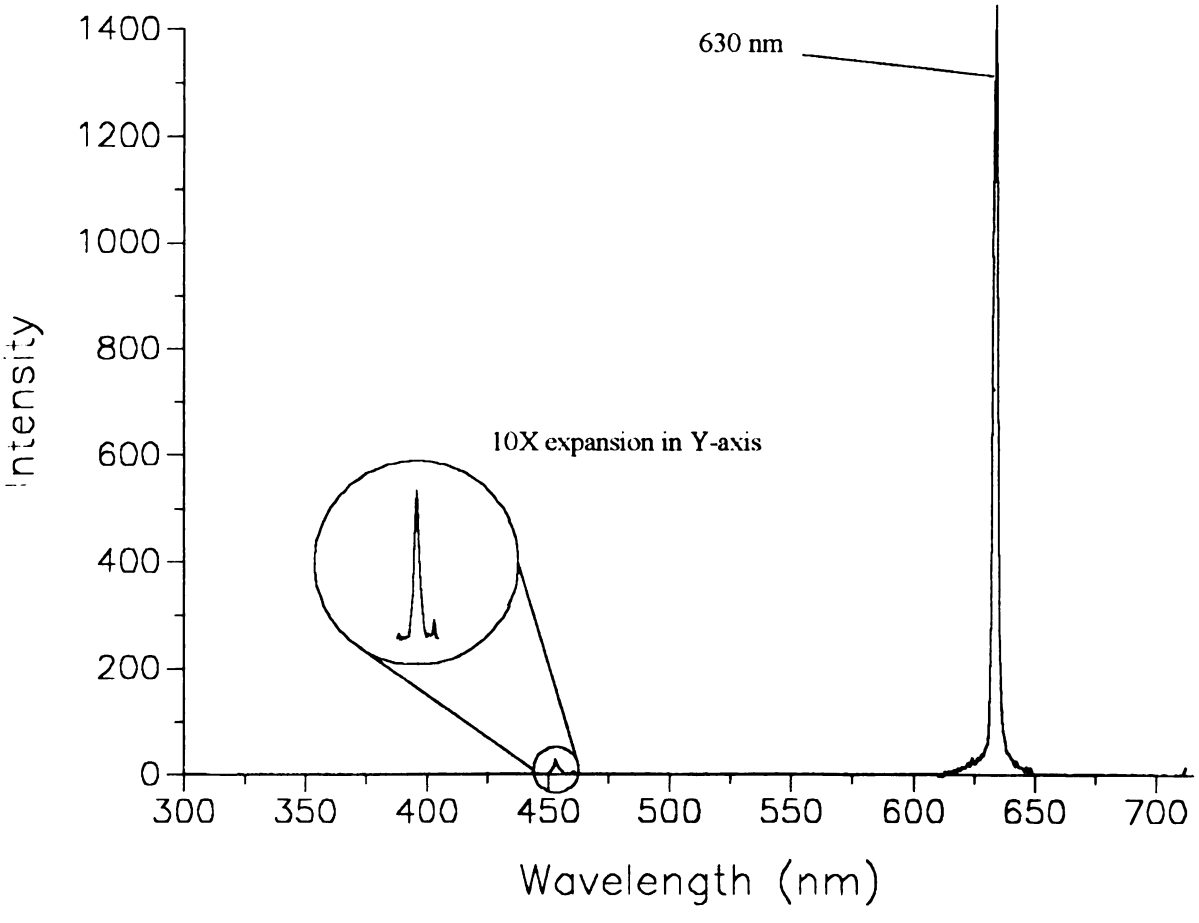

Figure 5-5

Plot Showing Stray Light Levels

The integration time was 10 ms, and the gain setting 0.3. The array was operated at room temperature. The pedestal rise in the middle of the array due to gain inhomogenaity has been subtracted out. The noticeable feature is the peak at 452 nm due to stray light reflections inside the array's spectrograph.

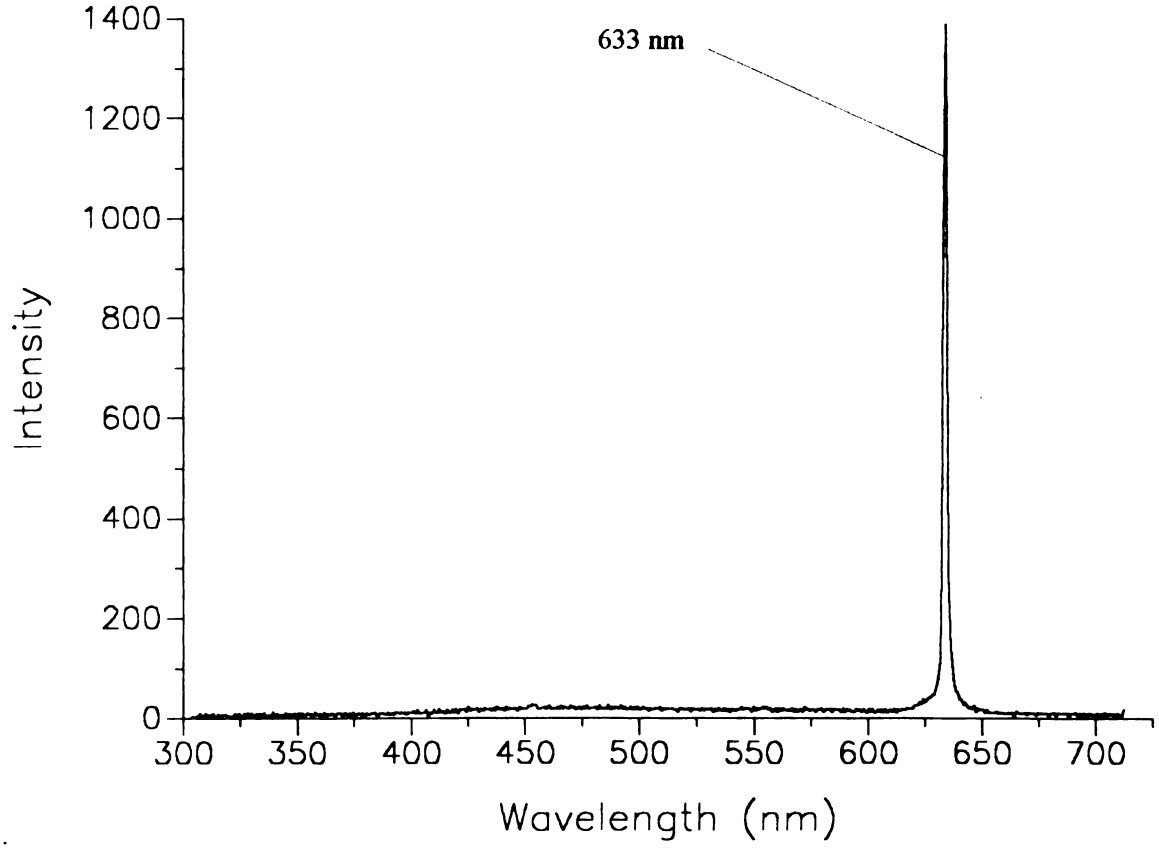

Figure 5-6

Instrument Resolution

The integration time was 10 ms, the intensifiers gain setting was 0.3. The array was operated at room temperature. The pedestal rise in the middle is due to gain inhomogenaity across the face of the array. The instrument also exhibits a 3 - 4 pixel peak width at FWHM for the He-Ne laser line.

Resolution

In the PDA, the resolution is dependent on the reciprocal linear dispersion of the grating (32 nm/mm) as well as the physical length of the array. The MCP intensifier further degrades the resolution by about a factor of 2 [5]. Because each photodiode in the array is covered by roughly 300 - 400 microtubules, bleed from the phosphor on the microchannel plate can degrade resolution. However, in the case of the present instrument, resolution degradation is most likely due to poor grating alignment. A difference of $1/20{,}000$ of an inch in the placement of the grating is the theoretical tolerance limit for focusing a line source on a single photodiode. This instrument sacrificed resolution for wavelength tuneability primarily because the instrument was built to study the wavelength regions from 190 - 700 nm. The intended use of the instrument was molecular fluorescence and absorption measurements in solutions where bandwidths are rarely narrower than 30 nm.

Slit width had no measurable effect on the instrument's resolution. The theoretical resolution is $12.8\,\text{mm}\ (\text{diode width}) \times 32\frac{\text{nm}}{\text{mm}} = 409\frac{\text{nm}}{512\ \text{diodes}} = 0.8\frac{\text{nm}}{\text{diode}}$. The bandpass of the narrowest slit is $25\ \mu\text{m}\ 32\frac{\text{nm}}{\text{mm}} = 0.8\,\text{nm}$, which corresponds to the theoretical minimal line width.

With tuning, the instrument was able to achieve the resolution of 2-3 diodes FWHM as specified by the manufacture's literature [5] (Figure 5-6)).

Dynamic Range

The dynamic range of the array was measured using a quartz halogen lamp source, a 10 ms integration time, a 50 μm slit width, and an intensifier setting of 1.55. The %T axis was fixed by using a series of neutral density filters of transmittance values 1.02, 2.95, 10.0, 19.5, 29.5, 41.7, 66.1, and 81.3 percent. The peak amplitude was measured as the average of 100 scans with each of the filters in place. A dynamic range of roughly 3 orders of magnitude was observed (Figure 5-7). To gauge the effect that the intensifier would have on the dynamic range, the previous filter experiment was repeated. The slit was narrowed to 25 μm and the gain increased to bring the number of counts to equal the count level of the first experiment. As can be seen in Figure 5-7, the gain does not affect the dynamic range. Both curves exhibited linearity to 3 orders of magnitude. The short integration time prevented the dark current pedestal from limiting the instruments dynamic range. By rotating the grating to move the peak of the lamp across the face of the array, the dynamic range was not found to change measurably.

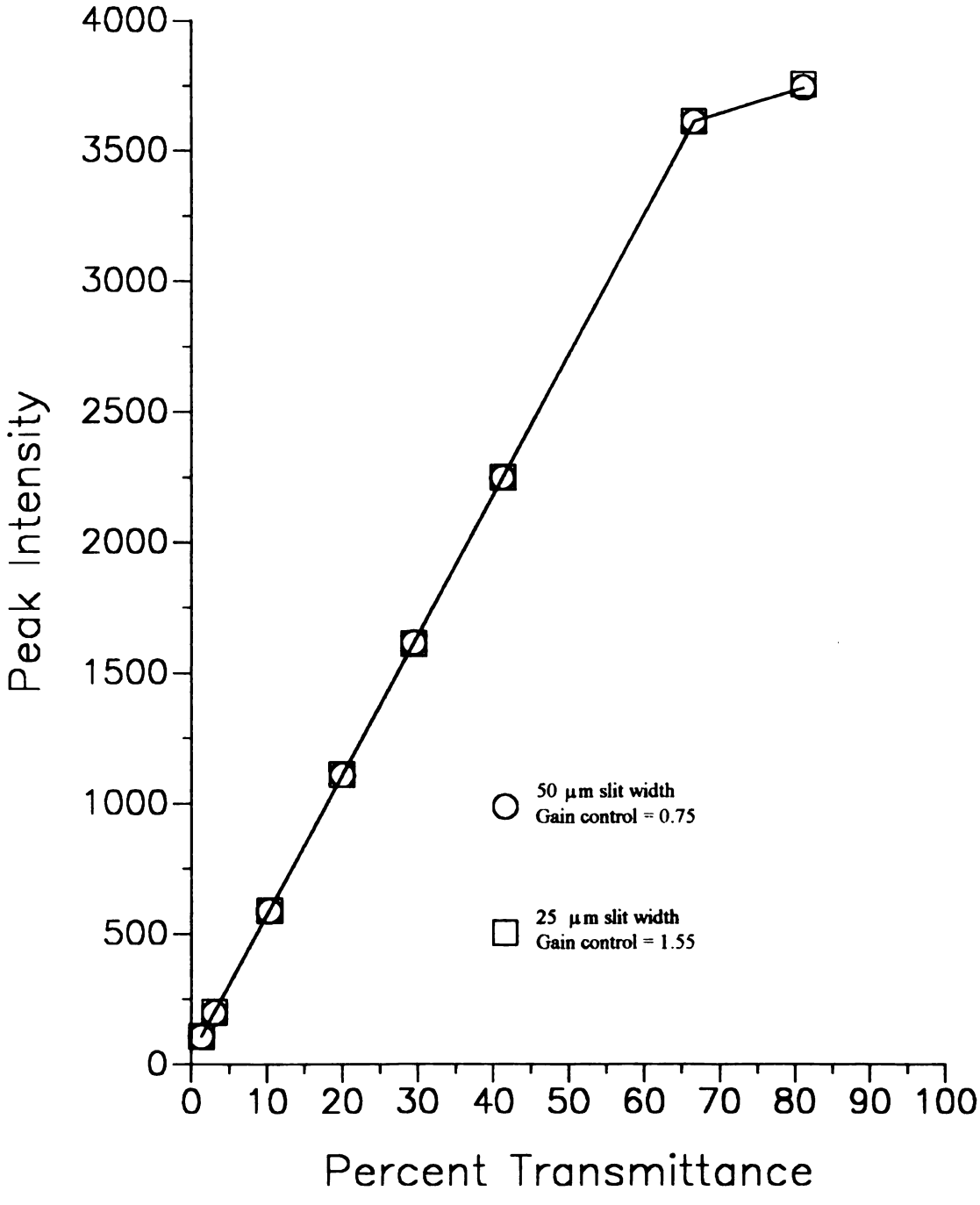

Figure 5-7

Peak Intensity vs Transmittance

Plot showing linear dynamic range of PDA. Notice how the gain control does not have any effect on the linear range of the system. Linearity was observed across 3 orders of magnitude.

Diode-to-Diode Sensitivity Variations

The diode array is read out by a 4-phase clock system. The signal from the odd and even diodes are amplified by matched circuitry and amplifiers. If the bias of the amplifiers is out of tune, a pseudo "noise" can be seen. This is due to gain variations when the odd and even diode signals are amplified. The operator's manual describes the procedure for matching the gain of the odd/even readout circuitry when the adjustment becomes necessary [5]. Diode to diode variations caused by unbalanced amplifiers can become a concern when averaging the signal from multiple diodes in memory. If the bunching is small, say 3 diodes, then the first group will consist of even-odd-even, while the next bunch will be odd-even-odd. Clearly, unbalanced amplifiers could have a detrimental effect on the S/N ratio. For a ratio type measurement (absorbance or transmittance), the effect is nulled out. The manufacture's literature specifies a spatial gain inhomogenaity of less than 62%. This means the minimum amplitude will not be less than 37.5% of the maximum amplitude over the active elements [5].

To measure the natural variations encountered in a multi-element diode array, a gray light source was used to uniformly illuminate the surface of the array. The concave grating was replaced by a Kodak neutral gray card. The card was dimly illuminated by exposing it to a dim diffuse light source while the cover was removed from the spectrograph. Figure 5-8 shows the natural variations in diode sensitivity due to the manufacturing processes. Fortunately, being rather reproducible, this natural variation should not reduce the instrument's photometric precision. This is best illustrated by comparing the plot of the 632 nm He-Ne line in Figures 5-5 and 5-6. Figure 5-5 is Figure 5-6 with the background subtracted.

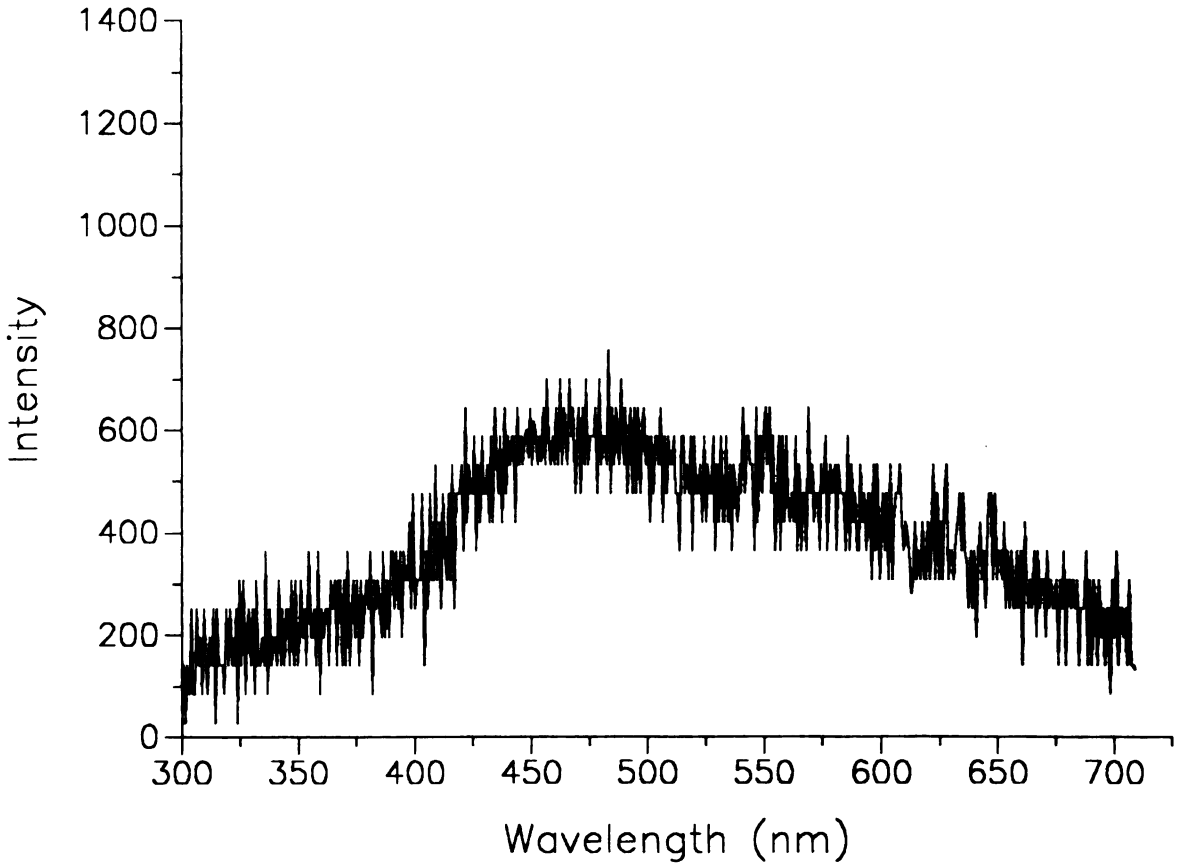

Figure 5-8

Gain Inhomogenaity Across the PDA

The array was illuminated with gray light to measure gain inhomogenaity across its length. The integration time was 300 ms with an intensifier setting of 0.75. The Y-scale is magnified by 20. The rise in sensitivity towards the middle of the array is due to gain inhomogenaity in the microchannel plate.

INTENSIFIER CHARACTERISTICS

A microchannel plate has a finite power on lifetime of roughly 1000 hours, after which the maximum gain will degrade to 50% of its initial value [5]. To conserve the intensifier's lifetime, a separate power supply and switch were built into the control panel to switch off the microchannel plate when the array was on but not in use. Additionally, the cost of an intensified array is triple that of an unintensified array. This is probably the most pressing reason for conserving power on hours.

After turning on the intensifier, the gain would reach 90% of its maximum value after 1.25 seconds, and level off to full scale after 2 seconds. Because the stability did not vary measurably, a 2 second warm up time was sufficient. Any long term drift in gain was insignificant compared to the long term drift in source intensity.

Nonuniformity in gain across the face of the microchannel plate is attributed to variations in the diode-to-diode response. According to the manufacturer, when uniformly illuminated, the spatial gain of the detector will have a variation of less than 62% [5]. For high microchannel plate currents, it has been shown that the gain decreases towards the center of the microchannel plate [7]. This is due to the fact that the resistance to charge replenishment at the center of the plate is limited by the resistance of the microchannel plate substrate. This resistance prevents the accumulation of sufficient charge to keep the plate at equilibrium and charge is lost faster than it can be replaced.

Another Figure of merit of the intensifier is the photon gain. The manufacturer's literature claims a 6000 fold photon gain at peak wavelength response when compared to an equivalent non-intensified detector [5]. The photon gain of the intensifier varies by a factor of about 75 between settings of 1.0 and 10.0 on the control potentiometer.

Memory Effects

Memory effects, particularly lag, refer to the signal being carried over from one scan to the next. According to the literature [8], linear diode arrays should not exhibit noticeable lag effects. However, with an intensified diode array, memory effects can arise from several processes. To quantitate the memory effects from various sources, two separate experiments, were performed.

In the first experiment, the slits to the spectrograph were covered, the power to the intensifier was switched off, and the array was allowed to saturate in the dark. After 20 seconds, the array was read out rapidly 100 times at 10 ms intervals. The results of the experiment are shown in Table 5-2. After 2 readouts occur, there is no measurable residual charge and all the remaining scans intensities are constant.

Table 5-2

PDA Memory Effects

Scan Readout	Total Time (ms)	% of full scale (4096 counts) (average of 510 diodes)
0	-	3.7
1	10	2.1
2	20	0.7
3	30	-
4	40	-
5	50	-
10	100	-
20	200	-
50	500	-

The experiment was repeated, with a gray light source used to saturate the array. The cover was left on the spectrograph, the quartz iodine lamp was the source, and a gray card substituted for the concave grating. The intensifier was left on, and the gain was set to 1.5. After allowing 20 seconds for saturation, the lamp was switched off and the array was read out as before. The results were identical to the previous experiment. It would appear that all lag effects are due to processes in the diode array, with no measurable contribution from the microchannel plate image intensifier. Other researchers have required 5 or more consecutive scans to reach a stable baseline after the exposure was terminated [3]. We surmise the lack of any additional memory lag attributed to the microchannel plate is due to the custom nature of the phosphor that was incorporated into our PDA. The manufacturer's specification sheet for this unit gives a typical decay rate of 1 ms for the phosphor to decay to 10% of its full scale value. As our minimum integration time is 3.5 ms, the phosphor would go through at least 3.5 100-10% half-life decay periods. This would leave only $0.1 \times 0.1 \times 0.1 = 0.1\%$ of its original value. Cooling the array may prolong the phosphorescence of some of the longer lived components such that they could become noticeable. However the array is rarely cooled when scanning at such short integration periods.

To minimize the effects of memory lag, the control software continually scans the PDA at 25 ms intervals. This minimizes lag by assuring the array is not allowed to saturate with dark signal.

REFERENCES

1. J.D. Ingle, S.R. Crouch, Spectrochemical Analysis, Prentice Hall, Engelwood Cliffs, New Jersey, 1988.

2. Y. Talmi, *Appl. Spec.*, **36(1)**, 1 (1982).

3. M.R. Hotchkiss, J.D. Ingle Jr., *Talanta*, **34(7)**, 619 (1987).

4. Y. Talmi, R.W. Simpson, *Appl. Opt.*, **19**, 140 (1980).

5. TN-6100 Series DARSS Detector Head Manual, Technical Manual PCN-278, Tracor Northern Inc., Middleton, WI. 53362 (1983).

6. P.J. Aiello, Ph.D. Dissertation, Michigan State University, East Lansing, MI., (1982).

7. Characteristics and Applications of Microchannel Plates., Technical Manual RES-0795, Hamamatsu Corporation, Middlesex, N.J., 08846 (1984).

8. G. Horlick, *Appl. Spec.*, **30**, 113 (1976).